

Thermally Driven Visco-Elastic Measurement Technique via Spectral Variations in Scanning
Probe Microscopy Cantilevers

By

Ryan Edward Jones

M.S., Mechanical Engineering
Massachusetts Institute of Technology, 1999

B.S., Mechanical Engineering
University of South Carolina, 1997

Submitted to Department of Mechanical Engineering
In Partial Fulfillment of the Requirements for the Degree of

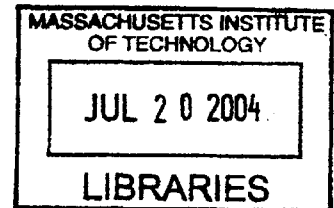
Doctorate of Philosophy in Mechanical Engineering

at the

Massachusetts Institute of Technology

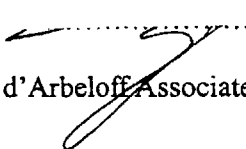
June 2004


© 2004 Massachusetts Institute of Technology
All right reserved



Signature of Author.....

Department of Mechanical Engineering
May 7th, 2004

Certified by.....

Douglas P. Hart
d'Arbeloff Associate Professor of Mechanical Engineering
Thesis Supervisor

Accepted by.....

Ain A. Sonin
Chairman, Department Committee on Graduate Students

Thermally Driven Visco-Elastic Measurement Technique via Spectral Variations in Scanning
Probe Microscopy Cantilevers

By

Ryan Edward Jones

Submitted to Department of Mechanical Engineering
on May 7th, 2004 in Partial Fulfillment of the Requirements for the
Degree of Doctorate of Philosophy in
Mechanical Engineering

ABSTRACT

Understanding how fluids respond to various deformations is of great importance to a spectrum of disciplines ranging from bio-medical research on joint replacements to sealing technology in industrial machinery. Specifically, this work addresses the need for probing interfacial rheology to understand how lubricants fail as system scales are reduced from bulk dimensions to molecular length scales. In the pursuit of interfacial rheology, one needs a platform capable of the temporal and spatial range and resolution required to quantify the visco-elastic fluid properties in the interfacial regime. With the availability and versatility of AFMs and the mounting models and data related to the performance of SPM probes in a fluid environment, the AFM is an attractive platform to exploit.

This thesis will discuss the use of thermal oscillations of an SPM probe to quantify the visco-elastic properties of fluids via spectral variations. There exist theoretical models for the Fluid-Structure Interactions (FSI) of vibrating bodies in incompressible viscous mediums that have been validated. This thesis will discuss how these models have been extended to develop a new visco-elastic FSI model. The analytical results of these models will be quantitatively compared to thermally driven SPM cantilevers to extract fluid properties. The new theory required for modeling the probe dynamics is outlined and the present limitations, for both the analytical and experimental techniques, are discussed.

Thesis Supervisor: Douglas P. Hart

Title: d'Arbeloff ~~Associate Professor of~~ Mechanical Engineering

Biographical Note and Acknowledgements

I was born and raised in a little town named Elgin, SC. I remember the town receiving its first stoplight, but small town did not equate to small dreams. After graduating from Lugoff-Elgin High School, I transitioned to the Mechanical Engineering program at the University of South Carolina (USC) in the Fall of 1993. The next four years served to wet my palette but did not satiate my hunger for learning. I then came to the Massachusetts Institute of Technology (MIT) for my M.S. in Mechanical Engineering in the Fall of 1997. After completing my masters degree in February of 1999, I thought my education was complete so I went to work for the Central Intelligence Agency (CIA) in Washington, DC. After about one year, my academic fever flared up once again, and I found myself MIT bound for the Ph.D. program in January 2000. Four and one half years later, I find myself standing on the edge of a new stage in my life.

While feeling such pride over my accomplishments, it is simultaneously extremely humbling. Accomplished people never stand alone as an island. As much work and sacrifice as I have made personally, I am ever cognizant of the fact that none of this would be possible without my amazing support structure of friends and family.

Regarding this latest stage of my life, spanning the last four years, I would like to thank all the present and past members of the fluids laboratory at MIT. You created a fun and intellectually stimulating environment in which to thrive. To the Hatsopoulos Microfluids Laboratory (HML) faculty and staff, thank you for fostering and supporting such a unique environment (BBQs, Christmas parties, etc.). I think the HML was the envy of the department! No other lab had the Lilie factor. To the department, a special thanks to Leslie and Joan for watching over all of us throughout our graduate work.

Finally, I would like to give a special thanks to my family. I am forever indebted to you for the innumerable amount of times that your love, support and encouragement gave me the strength to forge ahead. My parents infused me with a strong moral and ethical compass that I hope is continually reflected in both my personal and professional life.

One final thought...no matter where you go or what you do, never forget where you came from. It is the sum total of our lives that define who we are and we should cherish those experiences and never forget them.

Table of Contents

1	Introduction and Motivation	14
1.1	Hydrodynamic, Mixed and Boundary Lubrication	14
1.2	Current research in tribological systems	17
2	Background	21
2.1	Visco-elasticity	21
2.2	Rheological Measurements	22
2.2.1	Outline Newtonian fluid and motivate complex viscosity and shear modulus	22
2.2.2	Quantifying Complex Viscosity, η^* , with Small Amplitude Oscillatory Shear (SAOS)	28
2.2.3	Techniques for thin film rheology	30
2.3	SPM testing	36
2.3.1	Functional components of AFM	36
2.3.2	Other research using SPM technology for visco-elastic measurements	38
2.4	Research objective	40
3	Theory	43
3.1	Thermal excitation	43
3.1.1	Deterministic theory	43
3.1.2	Random signal theory: thermal energy	44
3.1.3	Thermal Power Spectral Density	45
3.2	Beam Dynamics	49
3.2.1	Derivation and Solution of Euler-Bernoulli beam equation	49
3.2.2	Effect of viscous/elastic fluid environment on spectral response	55
3.3	Fluid Structure Interaction (FSI)	56
3.3.1	Viscous FSI	57
3.3.2	Visco-Elastic FSI	63
3.3.3	Scaling effects	66
4	Experimental Setup and Testing Procedures	68
4.1	Experimental Testing Configuration	68
4.1.1	AFM and DAQ Integration	68
4.1.2	Cantilevers: triangular and rectangular w/ and w/o tips	69
4.2	Data Acquisition	71
4.2.1	Testing	71
4.2.2	Data Acquisition Hardware	72
4.3	Testing Procedure and Post-Processing	72
4.3.1	Experimental Testing Procedure	73
4.3.1.1	Typical Data Set	75
4.3.2	Post-processing	77
4.3.2.1	Processing of Experimental Data	78
4.3.2.1.1	Generate Force Curves	78
4.3.2.1.2	Generate Power Spectral Density	80
4.3.2.1.3	SHO fit to First Mode	81
4.3.2.1.4	Convert PSD to Magnitude of Transfer Function	83

4.3.2.2	Processing of Theory	84
4.3.2.2.1	Beam theory and visco-elastic FSI	84
4.3.2.2.2	Squeeze Film Analysis.....	85
4.3.2.2.2.1	Drag on a Cylinder.....	86
4.3.2.2.2.2	Squeeze-Film Theory.....	87
4.3.2.2.2.3	Micro-Viscometer	92
4.3.2.3	Fit visco-elastic FSI theory to experimentally measured data.....	94
5	Results and Discussion	96
5.1	Demonstrate thermal acquisition at known height with AFM platform.....	96
5.2	Baseline Techniques	97
5.2.1	Rheometer	97
5.2.2	Caber	100
5.3	Bulk Validation.....	104
5.3.1	Squeeze-film analysis to determine η_0	105
5.3.2	Fit new FSI theory to spectrum to determine λ	106
5.3.3	Visco-Elastic FSI Bulk Validation Data	108
5.4	Comparison and Discussion of Techniques.....	119
6	Limitations of the Technique.....	123
6.1	Experimental Limits.....	123
6.1.1	Low Frequency Viscous Limit of FSI Theory.....	129
6.2	Scaling limits	130
6.2.1	Polymer size and concentration effects.....	130
6.2.2	Effect of Viscous Boundary on Parameter Space	133
7	Conclusion	135
	Appendix A: Processing code used in IGOR with annotation for various macros and user-defined functions.....	137
	Works cited.....	166

List of Figures

Figure 1-1: Qualitative form of Stribeck curve which captures the three lubrication regimes: hydrodynamic, mixed and boundary lubrication ($h \equiv$ viscosity, $V \equiv$ velocity, $F \equiv$ force per unit length)	15
Figure 1-2: Hardy's model for boundary lubrication	17
Figure 1-3: Bowden and Tabor model for mixed and boundary lubrication	17
Figure 1-4: Micro textured surface example and quantitative Stribeck curves for various micro-textured surfaces. The plots illustrate the influence of size and coverage areas of 15 micron deep holes on the Stribeck curve. Data provided by Sara Hupp[11]	19
Figure 2-1: Silly Putty is a visco-elastic fluid, which exhibits very different behavior given a timescale of deformation and observation	21
Figure 2-2: Mechanical analogy of viscous and elastic components.....	24
Figure 2-3: Illustration of phase difference in elastic and viscous forces in response to oscillatory displacement. Plots are normalized with their maximum values.....	24
Figure 2-4: Visco-elastic mechanical element, which represents the mechanical analogy to the Maxwell constitutive fluid model	25
Figure 2-5: Mechanical analogy of Jeffreys constitutive relationship for a visco-elastic fluid[14]	26
Figure 2-6: Schematic of sheared visco-elastic fluid.....	27
Figure 2-7: Micro-Rheometer functional schematic[15, 16]	31
Figure 2-8: Schematic of micro-rheometer parallel alignment[16]	32
Figure 2-9: Schematic of compound linear leaf spring in micro-rheometer.....	33
Figure 2-10: Schematic of Surface Force Apparatus (SFA).....	34
Figure 2-11: Veeco Multi-Mode Atomic Force Microscope, which was used in conjunction with a NanoScope® IV controller	36
Figure 2-12: Schematic of AFM functional components (not to scale).....	36
Figure 2-13: AFM height and phase image of un-cleaved mica substrate, acquired in tapping mode: $A=25\mu\text{m}^2$	37
Figure 2-14: Typical cantilever dimensions and properties.....	38
Figure 2-15: Schematic for using dynamic response of SPM probes to quantify properties of a fluid environment.....	39
Figure 2-16: Spectral response of SPM cantilever in air, in a Newtonian fluid and in a visco-elastic fluid with similar viscosity. The qualitatively differences of the spectral response in the visco-elastic fluid will be quantified to yield rheological properties.....	41
Figure 3-1: Deterministic system response of a Simple Harmonic Oscillator. The input is convolved with the impulse response of the system to yield the time dependent output	43
Figure 3-2: System Dynamics with Random Inputs	44
Figure 3-3: Electrical analogy of thermal driving energy. The driving voltage, thermal power, is desired so that the response of the load resistor, SPM probe, can be modeled.	47
Figure 3-4: Schematic and dimensions used for solution to cantilever bending and dynamics ..	49
Figure 3-5: Differential beam element.....	50
Figure 3-6: Spatial mode solution to Euler-Bernoulli beam equation. The x and y axis of this plot have been normalized by the length of the beam and maximum tip deflection, respectively.	52
Figure 3-7: Typical normalized frequency response of cantilevered probe	55

Figure 3-8: Cylindrical Approximation for fluid structure interaction model. Model is an infinite cylinder translating normal to its z-axis with a given oscillating velocity.....	57
Figure 3-9: Relate the fluid structure interaction model to equivalent parameters in the SHO model for the probe.....	61
Figure 3-10: Added mass and dampening terms as a function of frequency. The normalized mass and dampening were defined as m_{add}/m_{disp} and $b_{add}/m_{disp}\omega^*$, respectively. The normalized frequency was defined as ω/ω^*	63
Figure 3-11: Normalized plots of η' and η'' for a Maxwell fluid.....	64
Figure 3-12: Added mass and dampening terms for a Maxwell fluid($\eta_0=0.008Pa\ s$ and $\lambda=0.8ms$) compared to that of a Newtonian fluid with the same viscosity.....	65
Figure 3-13: Infinite Boundary Condition for fluid structure interaction model.....	66
Figure 3-14: Planar viscous boundary condition for fluid structure interaction model.....	66
Figure 4-1: Integration of AFM and separate data acquisition system.....	69
Figure 4-2: Tipped cantilevers limit the minimum separation between a cantilevered beam and substrate.....	70
Figure 4-3: A conceptual experiment in which data would be acquired during the pause in the retracted position, and the approach curve would give the precise location at which the thermal was captured.....	71
Figure 4-4: Testing parameter input and post-processing flow chart to yield visco-elastic fluid properties: η_0 and λ , at a know height above the substrate, h	73
Figure 4-5: Portion of testing procedure checklist, which illustrates critical aspects of the experimental testing.....	74
Figure 4-6: Time response of probe in Squalane. The motion of the piezo clearly affects the deflection data and needed to be identified to avoid inclusion in the spectra.....	75
Figure 4-7: This is un-processed cantilever deflection corresponding to piezo motion illustrated in Figure 4-3. The relaxation of the cantilever at "A" and the linear deflection region at hard contact with the substrate is apparent.	76
Figure 4-8: Cantilever deflection, or force, verses substrate position as the piezo is extended and retracted.....	77
Figure 4-9: When defining thermal wave, one must omit portions where the cantilever is relaxing in order to minimize spectral errors.....	78
Figure 4-10: One must plot the cantilever deflection verses the piezo position such the optical lever sensitivity, [nm/V], can be recalculated to ensure correct conversion from photo-diode voltage signal to nm deflection.....	79
Figure 4-11: The cantilever deflection, y-axis, and separation, x-axis, need to be zeroed such that the height at which the thermal was obtained can be determined. This force curves was obtained in squalane Figure 4-7.....	80
Figure 4-12: A SHO model is fit to the first mode of the power spectral density to determine the m_C , b_C and k_C of the cantilever.....	81
Figure 4-13: The power spectral density can be converted to the effective magnitude of a SHO transfer function.....	83
Figure 4-14: Theoretical comparison of beam theory, Newtonian FSI theory and visco-elastic FSI theory.....	85
Figure 4-15: Schematic of cantilever and relevant system variables.....	85
Figure 4-16: Full range of theoretical deflection curves discussed in this paper. All curves have similar shape but are shifted according to fluid properties and testing dynamics.....	87

Figure 4-17: Theoretical dimensionless force curves. All force curves collapse in the squeeze-film regime, but are offset at larger distances from the substrate by drag effects	90
Figure 4-18: Cantilever response in water with approach velocity of 24.7 $\mu\text{m/s}$ to 107 $\mu\text{m/s}$	91
Figure 4-19: Effect of viscosity on force curves. All curves were measured at 80 $\mu\text{m/s}$	92
Figure 4-20: Cantilever relaxation from 80.2 $\mu\text{m/s}$ in dodecane, decalin, and squalane	93
Figure 4-21: Fit visco-elastic theoretical response of modes to measured modal response. The Newtonian response is shown for comparison of the old FSI theory with the new VE-FSI theory.	95
Figure 5-1: SHO fits to the first mode of cantilever response at varying heights in water, ranging from $>60\mu\text{m}$ to 11 nm	96
Figure 5-2: Schematic of cone and plate rheometer configuration	97
Figure 5-3: Viscosity versus steady-state shear rate data	98
Figure 5-4: Oscillatory rheometer data for polyethylene oxide 1.0%	99
Figure 5-5: Oscillatory rheometer data for polyethylene oxide 3.0%	99
Figure 5-6: Schematic of how CaBER™ was used to determine fluid relaxation time, λ	100
Figure 5-7: CaBER data and exponential fit for polyol ester	101
Figure 5-8: CaBER data and exponential fit for polyethylene oxide 0.3%	101
Figure 5-9: CaBER data and exponential fit for polyethylene oxide 0.1%	101
Figure 5-10: CaBER data and exponential fit for polyethylene oxide 1.0%	102
Figure 5-11: CaBER data and exponential fit for polyethylene oxide 3.0%	102
Figure 5-12: CaBER data and exponential fit for polyalpha olefin	102
Figure 5-13: CaBER data and exponential fit for polyalkylene Glycol	103
Figure 5-14: CaBER data and exponential fit for diester azelate	103
Figure 5-15: Cantilever relaxation in PEO 0.3%: $k_C=0.02\text{N/m}$, $\delta=8.9\text{nm}$, $V_{probe}=53.5\mu\text{m/s}$	105
Figure 5-16: The measured beam response in air, which resulted in m_C , b_C and k_C , was used to check the beam theory output.	107
Figure 5-17: Visco Elastic FSI theory was fit to the measured response of the beam in PEO 0.3%.	108
Figure 5-18: Cantilever relaxation in PEO 0.1%: $k_C=0.02\text{N/m}$, $\delta=3.8\text{nm}$, $V_{probe}=53.5\mu\text{m/s}$	109
Figure 5-19: Visco Elastic FSI theory fit to the measured response of the beam in PEO 0.1%.	109
Figure 5-20: Cantilever relaxation in PEO 0.03%: $k_C=0.017\text{N/m}$, $\delta=1.9\text{nm}$, $V_{probe}=53.5\mu\text{m/s}$..	110
Figure 5-21: Visco Elastic FSI theory fit to the measured response of the beam in PEO 0.03%.	110
Figure 5-22: Cantilever relaxation in PEO 0.01%: $k_C=0.02\text{N/m}$, $\delta=2.0\text{nm}$, $V_{probe}=53.5\mu\text{m/s}$	110
Figure 5-23: Visco Elastic FSI theory fit to the measured response of the beam in PEO 0.01%.	111
Figure 5-24: Cantilever relaxation in PAO: $k_C=0.02\text{N/m}$, $\delta=11.7\text{nm}$, $V_{probe}=53.5\mu\text{m/s}$	111
Figure 5-25: Visco Elastic FSI theory fit to the measured response of the beam in polyalpha olefin.	112
Figure 5-26: Cantilever relaxation in POE: $k_C=0.02\text{N/m}$, $\delta=61\text{nm}$, $V_{probe}=37.2\mu\text{m/s}$	112
Figure 5-27: Visco Elastic FSI theory fit to the measured response of the beam in polyol ester.	113
Figure 5-28: Cantilever relaxation in DEA: $k_C=0.02\text{N/m}$, $\delta=39\text{nm}$, $V_{probe}=53.5\mu\text{m/s}$	113
Figure 5-29: Visco Elastic FSI theory fit to the measured response of the beam in diester azelate.	114
Figure 5-30: Cantilever relaxation in PAG: $k_C=0.017\text{N/m}$, $\delta=64\text{nm}$, $V_{probe}=9.3\text{nm/s}$	114

Figure 5-31: Visco Elastic FSI theory fit to the measured response of the beam in polyalkylene glycol.....	115
Figure 5-32: Cantilever relaxation in PEO 1.0%: $k_C=0.02N/m$, $\delta=45nm$, $V_{probe}=18.6\mu m/s$	115
Figure 5-33: Visco Elastic FSI theory fit to the measured response of the beam in PEO 1.0%.....	116
Figure 5-34: Cantilever relaxation in PEO 3.0%: $k_C=0.02N/m$, $\delta=1.011\mu m$, $V_{probe}=9.3nm/s$...	116
Figure 5-35: Visco Elastic FSI theory fit to the measured response of the beam in PEO 3.0%.....	117
Figure 5-36: Visco Elastic FSI theory fit to the measured response of the beam in water.....	118
Figure 5-37: Visco Elastic FSI theory fit to the measured response of the beam in calibration fluid.	118
Figure 5-38: Micro viscometer viscosity verses rheometric viscosity. The dark line, with slope=1, represents a perfect correlation between the two techniques for determining viscosity.	120
Figure 5-39: VE-FSI relaxation time verses CaBER relaxation time. The dark line, with slope=1, represents a perfect correlation between the two techniques for determining relaxation time.	120
Figure 5-40: Relaxation time of PEO ($M_w=2e6$) was independent of concentration in the dilute regime, and had a power law slope of 2.5 at higher concentrations.	121
Figure 6-1: Noise in data limits the ability to fit the theoretical visco-elastic FSI at higher frequencies	123
Figure 6-2: Comparison of noise level for identical setup: One spectral response is measure in air and the other response in 0.30% PEO.	124
Figure 6-3: Comparison of voltage PSD data for different dissipative environments with noise contributions from the DAQ system and photo-diode dark current	125
Figure 6-4: FSI theory + photodiode noise fit to measure response of cantilever in 0.30% PEO	126
Figure 6-5: Noise floor limits the resolution of λ , such that only $\lambda > 50\mu s$ was resolvable for $\eta_0=8e-3Pa s$ with a $PSD_{noise}=10^{-10}V^2/Hz$	126
Figure 6-6: Noise floor limits on λ : $\lambda > 20\mu s$ for $\eta_0=8e-3Pa s$ with a $PSD_{noise}=10^{-11}V^2/Hz$	127
Figure 6-7: Accessible parameter space (combination of η_0 and λ) that the thermally oscillating VE-FSI method can probe. The solid and dashed boundary was determined by consideration of the theoretical changes observed by systematically varying both η_0 and λ	128
Figure 6-8: Expansion of accessible parameter space by reduction of photodiode noise floor. Each successive dashed line represents 1 order reduction in the noise floor.....	129
Figure 6-9: Area between lines represents the area swept by the thermally oscillating cantilever for the fundamental mode. The higher modes swept larger volumes so only the fundamental mode is considered since it represents the minimum volume.....	132
Figure 6-10: As the viscous boundary is approached, the dissipation of the cantilever oscillations reduce the accessible parameter space for this technique.....	133

List of Tables

Table 3-1: Ratio of effective modal mass to the mass of the static cantilever.....	54
Table 4-1: Typical cantilever parameters	70
Table 4-2: Results from micro-viscometer testing.....	94
Table 5-1: Summary of η_0 and λ from baseline techniques used for comparison of the new thermally oscillating technique	104
Table 5-2: Comparison of beam theory and experimental data	107
Table 5-3: Comparison of rheometer(η_0) and CaBER(λ) data to η_0 and λ obtained from fitting the new VE-FSI theory to measured responses of the SPM probes.	119

List of Symbols

Symbol	Description/Formula	Units
\bar{E}	Energy	J
μ	Friction coefficient	--
λ	Relaxation time	s
π	Pi	--
ω	Angular frequency	rad/s
τ	Tangential stress	Pa
η	Viscosity	Pa s
ν	Angular frequency	rad/s
δ	Deflection	m
η'	Real part of complex viscosity	Pa s
η''	Imaginary part of complex viscosity	Pa s
$\rho(\tau)$	Auto-correlation function	
η^*	Complex viscosity	Pa s
η_0	Zero-shear rate viscosity	Pa s
b	Dissipation	N/(m/s)
b_{add}	Added dissipation (fluid)	N/(m/s)
De	Deborah number	--
E	Young's Modulus	Pa
F	Force	N
F'	Force per unit Length	N/m

G	Relaxation Modulus	Pa
G^*	Complex Modulus	Pa
h	Planck constant	J s
I	Area moment of Inertia	m^4
j	$\sqrt{-1}$	--
k	Spring Constant	N/m
k_B	Boltzmann constant	J/K
Kn	Knudsen number	
L	Length variable	m
m	Mass	kg
M	Moment	N m
m_{add}	Added mass (fluid)	kg
n	Counter or index	--
P_L, P_{th}	Electrical Power	W
R, R_s, R_L	Electrical Resistance	Ω
Re	Reynolds number	--
Re_ω	Kinematic Reynolds number	--
$S, S_L, S_{th_v}, S_{th}, S_F$	Power Spectral Density	V^2/Hz
So	Sommerfeld number	--
T	Temperature	K
U, V	Velocity	m/s
V, V_s, V_L	Voltage	V
w	z-axis beam deflection	m

X	Coordinates	--
X, x	Spatial variable	m
Y	Coordinates	--
Z	Coordinates	--
C, C*	Weight % concentration	kg _{solute} /kg _{solvent}

1 Introduction and Motivation

The importance of lubrication and wear is evident in many disciplines and sciences. Whether one is designing large scale machinery for moving tons of earth, high speed turbo-machinery or concerned with the longevity of surgically replaced knee joints, understanding the interplay of lubrication, substrates and wear mechanisms are essential to a successful design. When functioning properly, lubrication components are often overlooked with respect to the complications of the system in which they are incorporated. However, when these lubricated subsystems fail, they often bring everything to a literal grinding halt, which is often associated with substantial time and financial consequences.

Given the extreme range of applications where lubrication is required, it is no surprise that there are an equally broad range of lubricating regimes in which the lubricating mechanisms vary as well. The following sections will introduce the historical context of lubrication research and highlight the characteristic differences that distinguish various operating regimes. This will serve to set the stage and context of the current research of the thesis, which addresses interfacial rheology in these systems.

1.1 Hydrodynamic, Mixed and Boundary Lubrication

Lubricated systems are generally divided into three regimes: Hydrodynamic Lubrication, Mixed Lubrication and Boundary Lubrication. As shown in Figure 1-1, the Stribeck curve[1] is often used to capture the frictional behavior of lubricated contacts as a system passes from one regime to the other.

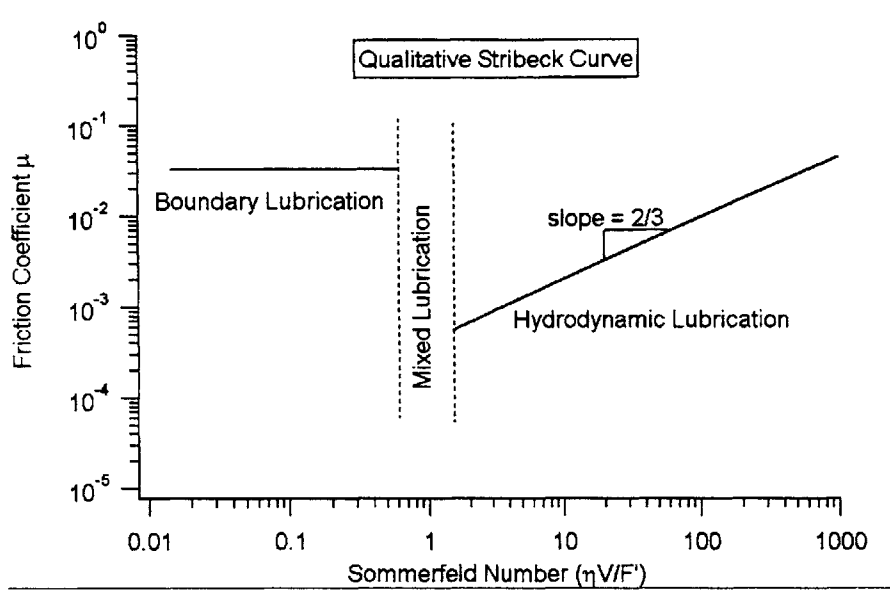


Figure 1-1: Qualitative form of Stribeck curve which captures the three lubrication regimes: hydrodynamic, mixed and boundary lubrication (η ≡viscosity, V ≡velocity, F' ≡force per unit length)

Of these three lubrication regimes, the most clearly understood is hydrodynamic, which has a power law slope of 2/3 on the Stribeck curve for a Newtonian fluid. The clarity of hydrodynamic lubrication has been derived from the uncoupled behavior of the lubricant and substrates. Unfortunately, it is not hydrodynamic lubrication that is often responsible for the severe and costly degradation of lubricated systems. Mixed and boundary lubricated regimes bear the responsibility for these adverse affects. This is a consequence of the load bearing capacity of the lubricated contact shifting from the internal lubricant pressure to surface asperity contacts, which results in wear. This transition is captured in the Stribeck curve via a sharp transition region, where the coefficient of friction becomes independent of the Sommerfeld number and approaches the sliding friction coefficient, $\mu = F_r / F_N$.

Despite very different operating regimes of lubricated contacts, it is impossible to design a contact that operates solely in one regime or the other. This results from the interdependence of

lubricant properties, contact geometry, contact loading and relative surface speeds on determining the dominant lubricating mechanisms. As a result, even lightly loaded systems will pass through a mixed regime during a transient start up process. As a result of this transition process, systems, which are hydrodynamic in steady state operation, will endure the wear of mixed and boundary lubrication.

The presence of the mixed and boundary lubricated regimes in systems is well known and has been experimentally confirmed, but not equally understood. There has been ample research into these areas, but a conclusive understanding of the physics has eluded researchers due to the scale of the phenomenon and the coupled behavior of the lubricating mechanisms.

The transition from hydrodynamic lubrication to boundary lubrication was studied as far back as the 1920's by W.B. Hardy. In fact, Hardy's initial theory, which dealt with adsorbed monolayers of molecules, is still the basis of our current models for boundary lubrication[2], see Figure 1-2. However, the currently accepted view of mixed and boundary lubrication is better illustrated by Figure 1-3. It was not until the 1940's that Bowden and Tabor developed this present view of mixed and boundary lubrication. The prevailing difference between the two theories was that Bowden and Tabor recognized the importance of surface asperity interactions and their effect on the system's behavior. With surface-to-surface interactions, models for friction began to include properties of lubricants, substrates and chemical and mechanical interactions between the two.

Despite being the accepted theory, most of the research over the last 50 years has focused on correlations between average film thickness and factors such as friction, wear and chemistry of the interface. One reason for this largely empirical approach to the research has been the

difficulty in observing and quantifying the lubricating phenomenon on the small and dynamic scale, which aggregately dictates the macroscopically observed response of the system.

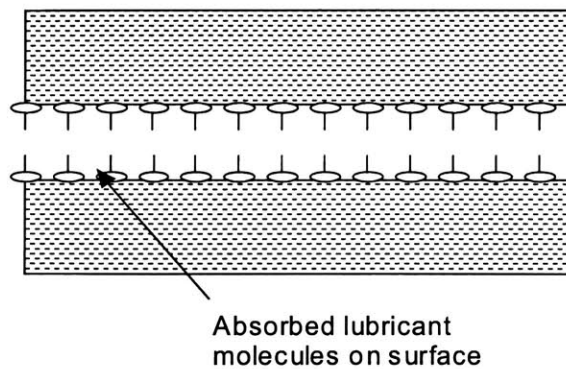


Figure 1-2: Hardy's model for boundary lubrication

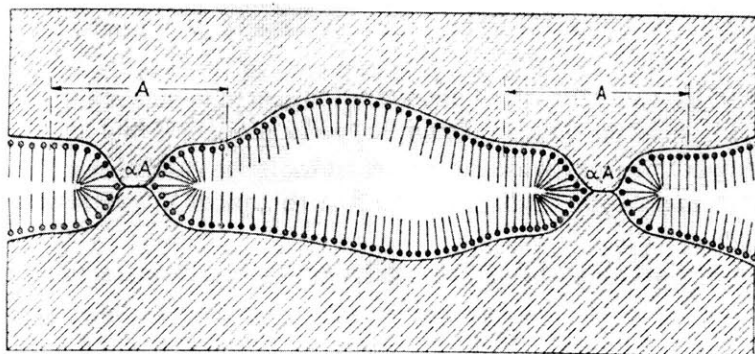


Figure 1-3: Bowden and Tabor model for mixed and boundary lubrication

1.2 Current research in tribological systems

Since directly observing and quantifying the lubricating parameters proved so difficult, researchers focused their efforts in areas where they could make strides. With the recent explosion in computational capabilities, complex models involving fluid structure interactions, actual surface roughness data and temperature and pressure dependence of viscosity have been developed[3, 4]. In contrast to this system level approach of looking at these contacts, Landman

and others[5, 6] have tackled the problem from a molecular perspective. Tracking every atom's position and velocity through time according to Newton's laws of motion, they have shown local elastic and plastic deformation of idealized asperities, and lubricant layering effects in highly confined geometries. Despite the apparent success of these models, experimental confirmation has not kept the same pace.

Unlike capacitive or resistive measurement schemes, which have been used extensively over the last 50 years and only provided spatially averaged quantities for lubricating films, new optical techniques are providing real time 3-D images of lubricating films. Techniques such as Dual Emission Laser Induced Fluorescence (DELIF), developed by Hart and Hidrovo[7], show capabilities for providing time dependent temperature and film thickness measurements over the lubricated region. Laser interferometric techniques have provided researchers with nanometer resolution for *in situ* measurements of hydrodynamic and boundary lubricated contacts[8-10]. Most importantly, these types of measurements provide experimental tools for validation of previously developed analytical models.

In addition to quantifying the performance of mixed and boundary lubricated contacts in practical configurations, there has been an equal push to replicate the operating conditions in an idealized configuration, and understand the physics on the micro-scale which control the macroscopic response. One such effort, shown in Figure 1-4, has been to fabricate micro-textured surfaces, and measure their frictional response to various lubrication conditions on a Stribeck curve[11].

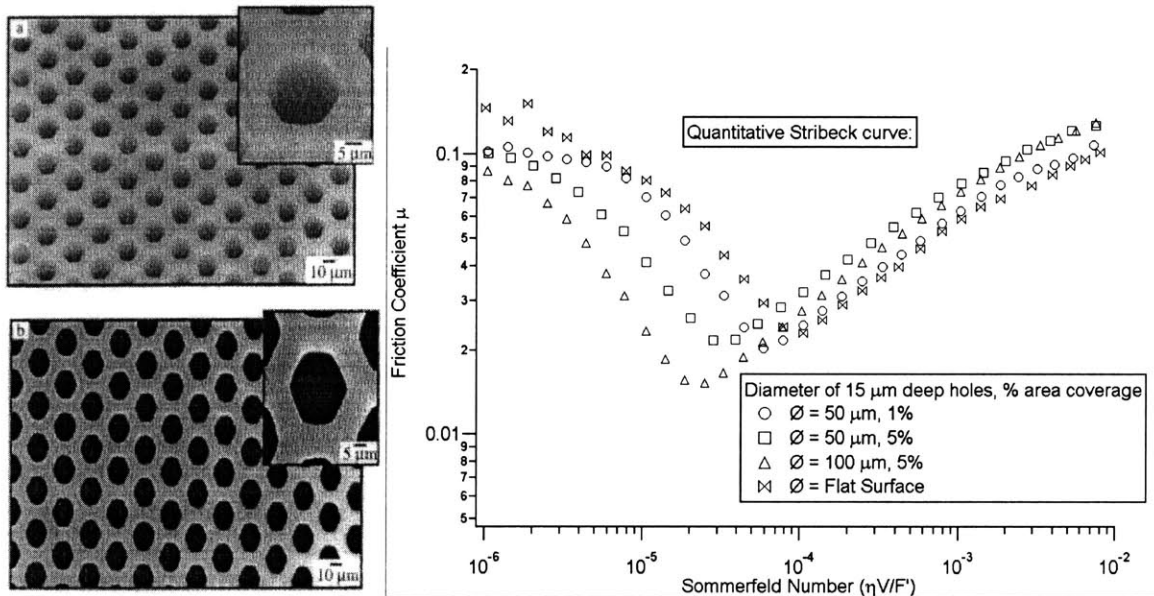


Figure 1-4: Micro textured surface example and quantitative Stribeck curves for various micro-textured surfaces. The plots illustrate the influence of size and coverage areas of 15 micron deep holes on the Stribeck curve. Data provided by Sara Hupp[11]

In addition to the effect of micro-textured surfaces, the lubricant properties, relevant to these scales, is an equally rich area of study. From a numerical perspective, researchers have been required to apply lumped correction factors to bulk properties for fluid properties as the film thickness becomes increasingly small. Similarly, Jacobson[12] modeled the lubricant, in contact regions of sufficiently high pressure, as a non-Newtonian material with solid type behavior. Although researchers were aware of apparent changes in lubricant properties on the temporal and spatial length scales in mixed and boundary lubrication, they were hand-cuffed without any quantitative method for determining the relevant properties.

It became clear that there was a significant piece of the puzzle missing if researchers hoped to understand micro-scaled mechanisms of these contacts. Although not the only piece, this understanding of how a lubricant's properties vary under these conditions had been relegated to the inclusion of empirical correction factors that provided agreeable results. Central to this

understanding is the response of the lubricant to the contact dynamics. Large variations in pressure, temperature, and strain rates, yield an equally wide range of lubricant properties from shear thinning of the dynamic viscosity to solid-like behavior and shear banding. One major question pertains to the lubricant rheology as the confines of the system approach time and length scales that modify the commonly used bulk properties of the lubricant. Understanding how the visco-elastic lubricant properties affect local lubricant-substrate force interactions is essential to understanding macroscopic contacts.

Despite the lack of experimental data on interfacial rheology and, more importantly, an acceptable method to acquire the data, it was clear that the physics on the micron and sub-micron scale dominated the systems macroscopic performance. This work focused on developing both the analytical models and experimental platform to provide researchers with a versatile tool capable of probing fluid properties from the bulk regime to the interfacial regime, in which fluids are confined to within nanometers of a substrate.

2 Background

2.1 Visco-elasticity

This chapter will give the necessary rheological background to understand the modeling methods chosen in subsequent chapters. In addition, this chapter will outline other techniques related to interfacial rheology and set the context for the work discussed in this thesis. With the repeated mention of lubricants exhibiting viscous and elastic behavior, it is first necessary to define what is meant by a visco-elastic fluid.

Consider the schematic shown in Figure 2-1. This is a sketch of the famous childhood toy, Silly Putty. Let's consider two different thought experiments and the response of the Silly Putty. In the first experiment on the left, a ball was formed and left to rest on a tabletop. Some time later it is observed that the ball has deformed into more of a pancake shape. Now in the second experiment on the right, the Silly Putty is again formed into a ball, but this

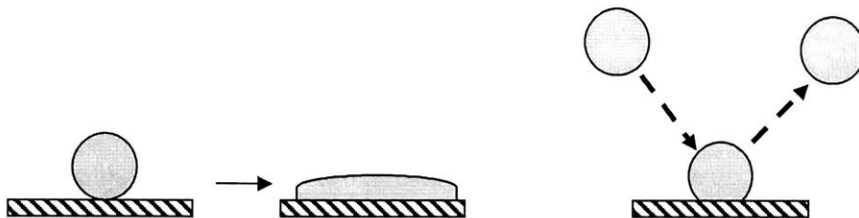


Figure 2-1: Silly Putty is a visco-elastic fluid, which exhibits very different behavior given a timescale of deformation and observation

time it is thrown against the floor, and bounces back like an elastic solid. In case one, the Silly Putty behaved as a viscous liquid, while in case two, it behaved as an elastic solid. The difference between the two experiments was simply the time scale of deformation compared with the relaxation time scale of the Silly Putty. In the first case, the observation time was several

minutes to hours, while in the second case, the time scale was a fraction of a second. This is the nature of visco-elastic fluids.

In the context of lubricated systems, as the confinement of a sheared visco-elastic fluid is increased, for a given relative speed between two shearing planes, the shear rate is increased. In addition to situations where the time scale becomes very short, there is a length scale at which the lubricant properties vary as a result of molecular influence from long chain polymers, which typically make up lubricants. The relevant dimensionless numbers associated with the spatial and temporal scales in confined fluid systems are the Knudsen number, $Kn = L_{fluid} / L_{system}$, and the Deborah number, $De = t_{fluid} / t_{system}$, respectively. With an intuitive understanding of visco-elasticity, the tools and methods used to quantify these properties will be discussed.

2.2 Rheological Measurements

This section will motivate and outline some analytics related to modeling visco-elastic fluids. Constitutive relations for Newtonian and non-Newtonian fluids will be discussed, which will establish the analytical framework required in the later discussions regarding the Fluid Structure Interaction modeling (FSI).

2.2.1 Outline Newtonian fluid and motivate complex viscosity and shear modulus

Most intuition and tools acquired from classic lubrication theory, usually deal with Newtonian fluids, in which the constitutive relation between stress and strain rate is given by equation (2.1).

$$\tau(t) = \eta \dot{\gamma}(t) \tag{2.1}$$

For a Newtonian fluid, the dynamic viscosity, η , is assumed to be constant. By incorporating this constitutive relation in the Navier-Stokes equations, scientist and engineers have been equipped to design and predict a host of practical problems. The next level of difficulty comes with the use of the General Newtonian Fluid (GNF)

$$\tau(t) = \eta(\dot{\gamma})\dot{\gamma}(t) \quad (2.2)$$

where $\eta(\dot{\gamma})$ is a material function, which relates dynamic viscosity to shear rate. Some of the more commonly used material functions are the power law

$$\eta = m\dot{\gamma}^{n-1} \quad (2.3)$$

and the Carreau model

$$\frac{\eta - \eta_{\infty}}{\eta_0 - \eta_{\infty}} = \left[1 + (\lambda\dot{\gamma})^a \right]^{\frac{n-1}{a}} \quad (2.4)$$

which captures shear-thinning behavior often observed at higher shear rates in polymeric fluids. Some additional material functions are the Ellis model, Truncated power law and Powell-Eyring model[13, 14].

The focus of this thesis is both the viscous and elastic properties of the lubricant. Newtonian and general Newtonian constitutive relations do not characterize any elastic components of the fluid. The following section will motivate and discuss the inclusion of elastic effects into constitutive models which capture the response of a visco-elastic lubricant.

In order to characterize a lubricant's visco-elastic properties, it is first necessary to understand how the viscous and elastic components are observed experimentally. A qualitative analogy can be made with some more intuitive mechanical elements, a spring and dashpot, as illustrated in Figure 2-2. The elastic spring exerts a force proportional to the displacement while the dashpot exerts a force proportional to velocity.

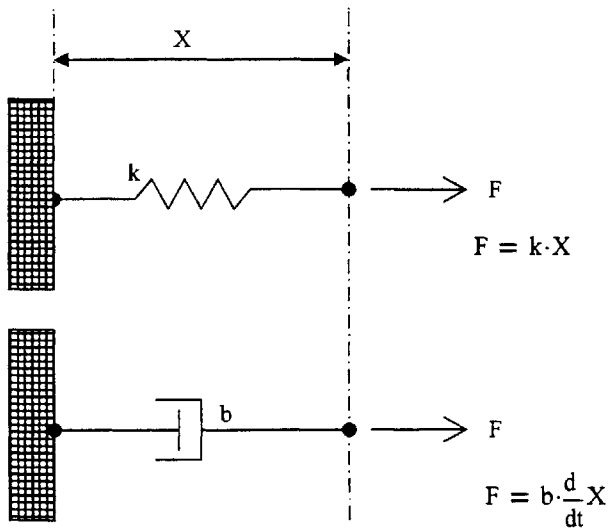


Figure 2-2: Mechanical analogy of viscous and elastic components

Now consider the situation where an oscillatory displacement is imposed on each of the mechanical elements, separately. If the forces required to maintain the oscillations are plotted together, Figure 2-3, it can be seen that there is a 90° phase between the elastic spring force and viscous dashpot force. The circles and triangle symbols represent the dashpot and spring reaction forces as a function of time in response to the unit amplitude oscillatory displacement, shown as the solid line.

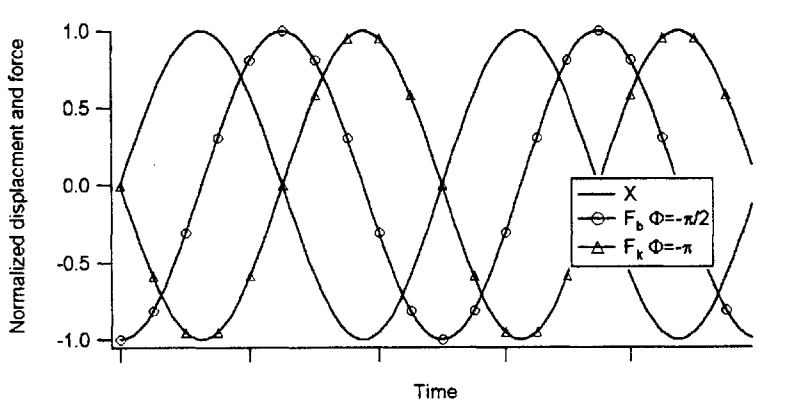


Figure 2-3: Illustration of phase difference in elastic and viscous forces in response to oscillatory displacement. Plots are normalized with their maximum values

Given the phase dependence of the force responses to an oscillatory displacement, one can understand how if the spring and dashpot were combined, Figure 2-4, the phase of the force response would be related to the relative magnitude of k and b .

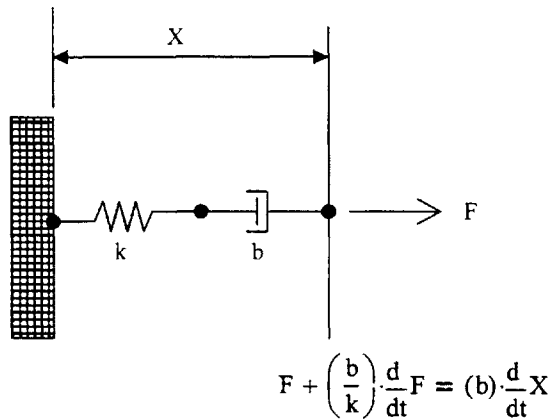


Figure 2-4: Visco-elastic mechanical element, which represents the mechanical analogy to the Maxwell constitutive fluid model

In addition to the phase of the response, the amplitude and frequency are equally important in determining the visco-elastic components. For example, if the frequency of oscillation was relatively small, $\omega \ll \frac{k}{b}$, the dashpot will result in a force response with an amplitude and phase equivalent to the dashpot. In contrast, if the oscillation frequency was relative large, $\omega \gg \frac{k}{b}$, the dashpot would behave as a rigid bar, simply compressing the spring with an amplitude and phase equivalent to a single spring. With the exception of the detailed equations, it can be seen that the values of both b and k can be obtained with information about the phase and amplitude of the force response at a given frequency.

The simplest analogous stress versus strain rate relation for a visco-elastic fluid is the Maxwell model, equation (2.5), where λ_1 and η_0 are the relaxation time and zero-shear rate viscosity, respectively.

$$\tau + (\lambda_1) \frac{d}{dt} \tau = \eta_0 \dot{\gamma} \quad (2.5)$$

Just as the Newtonian and GNF fluid, the Maxwell constitutive relation can be used in conjunction with the Navier-Stokes equations to model a lubricated contact.

As with the material functions discussed previously, increasingly complex analogies and constitutive relations are available, which more accurately characterize the stress-strain relationship of certain fluids, see Figure 2-5.

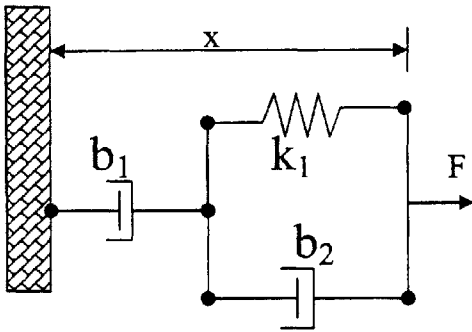


Figure 2-5: Mechanical analogy of Jeffreys constitutive relationship for a visco-elastic fluid[14]

$$F + \left(1 + \frac{b_2}{b_1}\right) \left(\frac{b_1}{k_1}\right) \frac{d}{dt} F = (b_1) \frac{d}{dt} X + \left(\frac{b_1}{k_1}\right) (b_2) \frac{d^2}{dt^2} X \quad (2.6)$$

$$\tau + \lambda_1 \frac{d}{dt} \tau = \eta_0 \left(\dot{\gamma} + \lambda_2 \frac{d}{dt} \dot{\gamma} \right) \quad (2.7)$$

Equation (2.6) and (2.7) are the associated equations for the Jeffreys model.

From an experimentalist's perspective, the in-phase and out-of-phase components of stress, $\tau(t)$, are often relatively easy to quantify, and it is instructive to solve for the stress response for a given constitutive model. The solution can be written in the following general form,

$$\tau(t) = - \int_{-\infty}^t G(t-t') \dot{\gamma}(t') dt' \quad (2.8)$$

where $G(t)$ is known as the relaxation modulus. For a Maxwell fluid, the stress function and relaxation modulus are given by equation (2.9) and (2.10).

$$\tau(t) = \int_{-\infty}^t \left\{ \frac{\eta_0}{\lambda_1} e^{-\frac{t-t'}{\lambda_1}} \right\} \dot{\gamma}(t') dt' \quad (2.9)$$

$$G(t) = \left\{ \frac{\eta_0}{\lambda_1} e^{-\frac{t-t'}{\lambda_1}} \right\} \quad (2.10)$$

The relaxation modulus and general stress solution will be used in the following section to develop expressions, which can be used to obtain parameters, such as η_0 and λ , of the constitutive relations.

In an equivalent manner to the deformation of the mechanical analogies, the visco-elastic properties of a fluid can be determined. Consider the schematic shown in Figure 2-6.

Small Amplitude Oscillatory Shear (SAOS)

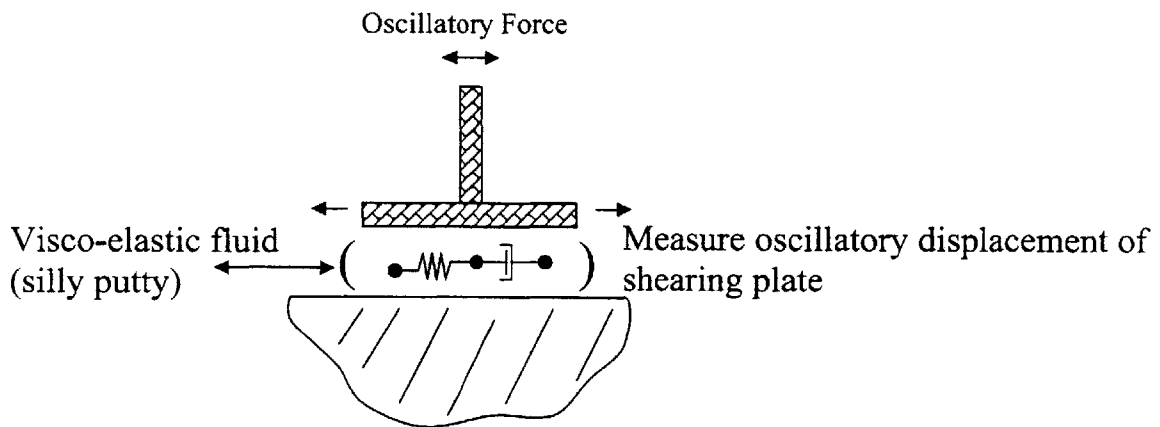


Figure 2-6: Schematic of sheared visco-elastic fluid

If a fluid, with both viscous and elastic components, is sheared in an oscillatory manner, the phase and amplitude of oscillation between the driving force and measured displacement is a consequence of the viscous and elastic components of the fluid. The following section will

outline the details to solve for the fluid's relaxation time and zero-shear rate viscosity for a Maxwell fluid, with the planar deformation of Figure 2-6. These methods may be extended for increasingly complicated constitutive relations, but the Maxwell model is used throughout this thesis, and therefore, the details are discussed below.

2.2.2 Quantifying Complex Viscosity, η^* , with Small Amplitude Oscillatory Shear (SAOS)

To model the response of a Newtonian fluid to deformation, a model was chosen for the material function, and in a similar manner, a visco-elastic model must be chosen, $\eta(\eta_0, \eta_\infty, \lambda_1, \lambda_2, \dots)$, for the visco-elastic fluid. For the visco-elastic material function, extending the idea of in-phase and out-of-phase components to adequately capture the material behavior, rheologists have adapted the use of a complex viscosity.

$$\eta^* = \eta' - j\eta'' \quad (2.11)$$

The complex nature of this definition readily lends itself to out of phase components where the complex relaxation modulus is defined by equation (2.12).

$$G^* = j\omega\eta^* \quad (2.12)$$

To obtain an expression for η' and η'' , consider a situation where a fluid is deformed in a Small Amplitude Oscillatory Shear configuration, recall Figure 2-6.

Let the shear-rate and stress be defined by equation (2.13).

$$\dot{\gamma} = \text{Re}\{\dot{\gamma}_0 e^{j\omega t}\}, \tau_{xy}^0 = -\eta^* \dot{\gamma}, \tau_{xy} = \text{Re}\{\tau_{xy}^0 e^{j\omega t}\} \quad (2.13)$$

Then by substitution of η^* , as defined previously, the stress becomes

$$\tau_{xy} = \text{Re}\{-\dot{\gamma}_0 (\eta' - j\eta'')(\cos(\omega t) + j \sin(\omega t))\} \quad (2.14)$$

which simplifies to

$$\tau_{xy} = -\dot{\gamma}_0 \{ \eta' \cos(\omega t) + \eta'' \sin(\omega t) \} \quad (2.15)$$

Experimentally, η' and η'' can now be determined by the relative amplitude and phase of the measured stress with respect to the imposed shear-rate. Finally, to connect this data to model parameters recall the following stress equation.

$$\tau(t) = - \int_{-\infty}^t G(t-t') \dot{\gamma}(t') dt' \quad (2.16)$$

Substituting for the imposed shear rate, $\dot{\gamma}(t)$, and making the following variable substitution.

$$s = t - t' \quad (2.17)$$

the stress function becomes equation (2.18).

$$-\tau_{xy} = \underbrace{\left[\int_0^{\infty} G(s) \cos(\omega s) ds \right]}_{\eta'} \dot{\gamma}_0 \cos(\omega t) + \underbrace{\left[\int_0^{\infty} G(s) \sin(\omega s) ds \right]}_{\eta''} \dot{\gamma}_0 \sin(\omega t) \quad (2.18)$$

Therefore, the following results for η' and η'' are obtained for a Maxwell fluid

$$\eta' = \int_0^{\infty} G(s) \cos(\omega s) ds = \int_0^{\infty} \left\{ \frac{\eta_0}{\lambda_1} e^{-\frac{s}{\lambda_1}} \right\} \cos(\omega s) ds \quad (2.19)$$

$$\eta'' = \int_0^{\infty} G(s) \sin(\omega s) ds = \int_0^{\infty} \left\{ \frac{\eta_0}{\lambda_1} e^{-\frac{s}{\lambda_1}} \right\} \sin(\omega s) ds \quad (2.20)$$

$$\eta' = \frac{\eta_0}{1 + (\lambda_1 \omega)^2} \quad (2.21)$$

$$\eta'' = \frac{\eta_0 (\lambda_1 \omega)}{1 + (\lambda_1 \omega)^2} \quad (2.22)$$

One can now fit these parametric expressions to the aforementioned measured data to obtain the parameters, η_0 and λ , in the constitutive relations. As a final reference, Small Amplitude

Oscillatory Extension (SAOE) is another method, although more difficult to achieve correct deformation of fluid, where the results are procedurally identical, with the result being larger by a factor of 3 due to the terms in the strain rate tensor.

$$\eta_e^* = 3\eta^* \quad (2.23)$$

2.2.3 Techniques for thin film rheology

There are numerous commercially available apparatuses for quantifying visco-elastic properties of lubricants and other materials by methods described in the previous section. However, these methods are generally limited in their spatial and temporal resolution due to inertial effects of components in the system. Consequently, these techniques are not well suited for thin film or interfacial rheology. This section will discuss techniques related to thin film rheology. Specifically, an overview of a collaborative effort aimed at building a micro-gapped planar rheometer, the Surface Force Apparatus (SFA) and other SPM techniques will be discussed.

It is always desired to relate lubricant behavior to parameters in rheological models. With models, one has predictive and design capabilities with which to predict a lubricant's behavior in specific applications. However, to compare models with experiment, one needs analytical solutions of the experimental setup with the desired model incorporated. The simplest setup, conceptually and analytically, is planar couette flow.

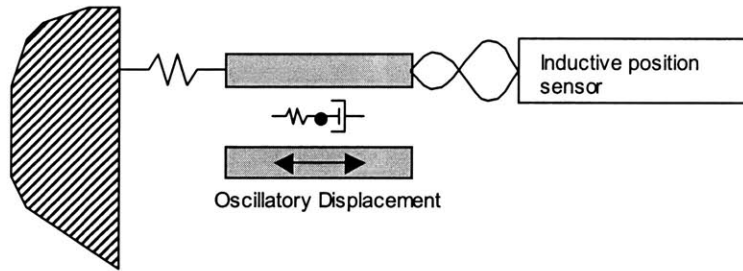


Figure 2-7: Micro-Rheometer functional schematic[15, 16]

Schematically shown in Figure 2-7 is a Micro-Rheometer[15, 16], which quantifies visco-elastic properties of lubricants in planar couette flow. This device operates on the same principles as discussed in the previous section. Although conceptually simple, achieving perfectly planar couette flow can be challenging if one considers shearing planes with areas on the order of cm^2 , while maintaining a spacing between the planes of order μm .

The first challenge was that of adjusting the shearing planes such that they were parallel. The second hurdle was to maintain these parallel planes while shearing. The effort of adjusting the planes, Figure 2-8, until they were parallel was accomplished by silvering optical flats and adjusting them like a Fabry-Perot Etalon until the spectrum passed into the spectrometer was spatially invariant[16].

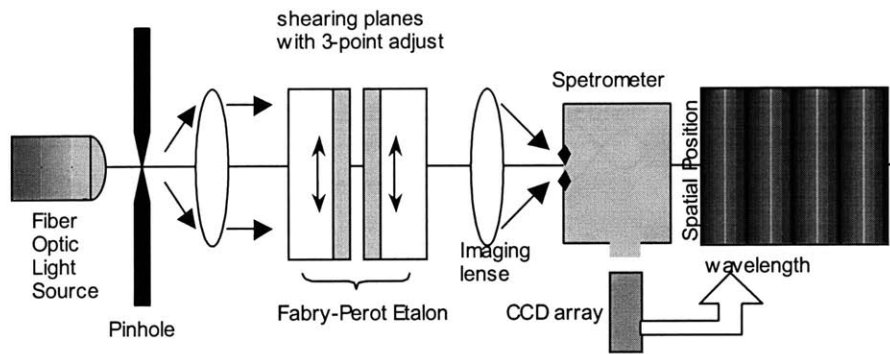


Figure 2-8: Schematic of micro-rheometer parallel alignment[16]

Had the optical flats, which served as shearing planes, not been parallel, the image on the CCD array would have appeared as slanted vertical lines, indicating a spatial variance.

With the plates parallel to within μrad , the remaining challenge was achieving rectilinear motion. Similar devices[15, 16] use small amplitude pendulum motion to approximate planar motion. This approximation limits the total strain that can be applied by the device without large out of plane motion, as well as limiting the range of steady-state shear experiments that can be performed. To eliminate these limitations, the micro-rheometer utilized a compound linear leaf spring, Figure 2-9. As illustrated, when the center plane is deflected to the left or right, the out of plane motion, expected from a typical leaf spring, is exactly matched by an equal and opposite out of plane motion. The net result of the deformation is rectilinear motion as apposed to pendulum motion.

Both the lower and upper planes are compound rectilinear springs to insure planar motion. As the fluid is sheared between the optical flats, the shear stress is transmitted, via the fluid, to the upper plane.

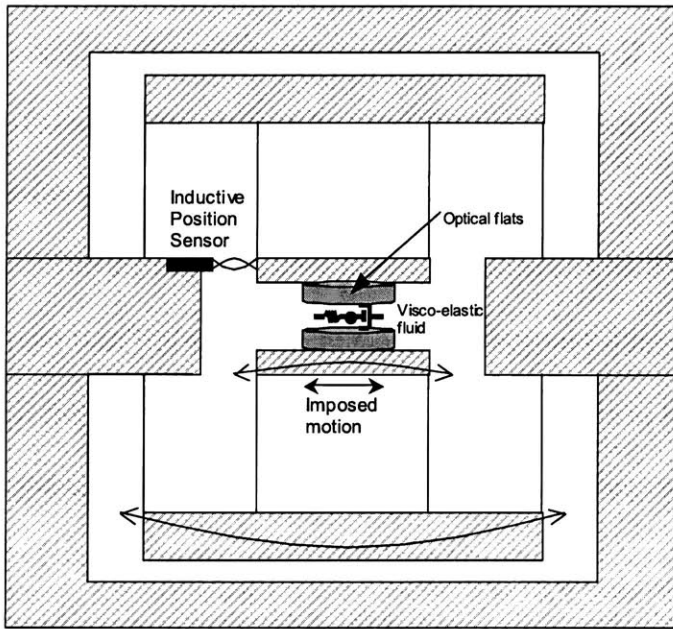


Figure 2-9: Schematic of compound linear leaf spring in micro-rheometer

The transmitted shear stress deflects the upper spring, with known k_{spring} , while an inductive position sensor detects the spring's displacement with a resolution of 20nm. This actuation and sensing scheme, adopted with permission, was a design used by L. Anand and B. Gearing at MIT for different applications, but was well suited for this system's requirements. Although successful for certain applications, this design lacked the force sensitivity for aqueous type viscosity fluids and spatial resolution below a couple μm .

In addition to the micro-rheometer, researchers such as Israelachvili and Granick developed a Surface Force Apparatus (SFA)[17-21].

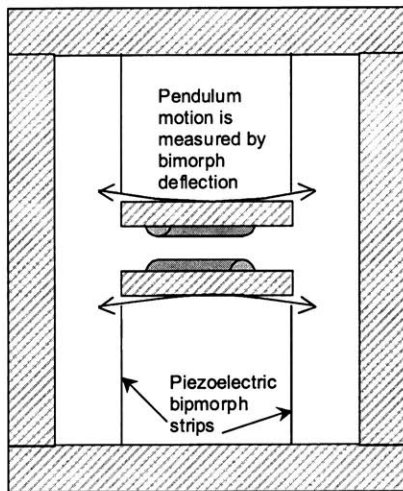


Figure 2-10: Schematic of Surface Force Apparatus (SFA)

Similar to the configuration of the micro-rheometer, the SFA utilizes leaf springs in a small amplitude pendulum motion. The leaf springs are piezoelectric bimorph strips, which deflect when a voltage is applied. Conversely, the force transmitted through the fluid is sensed by a resulting voltage due to the deflection of the opposing bimorph strips. This forcing and sensing scheme enables the force to be resolved to $\pm 10 \text{ nN}$. The SFA utilizes smooth mica covered cylinders to shear the fluid. The cylinders are positioned at right angles and the resulting contact geometry is equivalent to a sphere sliding over a flat plate. Unlike the planar configuration of the micro-rheometer, the cross cylinder setup does not require parallel alignment to ensure the resulting sphere on plane contact geometry. Piezoelectric tubes control the vertical surface separation, and the distance is determined with white light interferometry, which enables the separation to be determined to within 0.1 nm .

The piezo driven bimorph strips can be used to test both steady state shear and oscillatory responses of the fluid with the SFA. As illustrated in data presented by Israelachvili[19] the frequency response was restricted to values less than 0.1 kHz . This limitation is due to the inertia

of the fixtures and crossed cylinders at the end of the bimorph strips. This inertial limitation is systemic in all macroscopic devices. Although the SFA and micro-rheometer have solved the spatial resolution problem by providing nm precision positioning control and nN force sensitivities, they are both limited temporally.

The inertial limitations of these systems restrict their ability to measure relaxation times greater than $1/(2\pi f_{max})$, where f_{max} is the maximum attainable oscillation frequency. In molecularly confined films, where the relaxation times become larger than in the bulk, this limitation is less significant. However, the component inertia, of these macroscopic systems, is significant when one attempts to quantify smaller relaxation time constants, as seen in the bulk regime.

With the availability of equipment used in Scanning Probe Microscopy (SPM), researchers have begun to probe the local fluid-substrate force interactions with resolutions of pN using a variety of SPM techniques[22-24]. It is therefore naturally tempting to exploit the low inertial and high temporal and spatial resolution of SPM techniques to quantify the rheological response of fluids.

Before discussing the use of SPM techniques, an overview and discussion of the functional components of an AFM are required. The following section will discuss the operational capabilities of an AFM, with emphasis on its ability to achieve the spatial and temporal requirements for probing interfacial rheology.

2.3 SPM testing

2.3.1 Functional components of AFM

To understand the motivation for using an Atomic Force Microscope (AFM), it is first necessary to understand how the AFM generates images and how this relates to the functional needs of an interfacial rheology probe.



Figure 2-11: Veeco Multi-Mode Atomic Force Microscope, which was used in conjunction with a NanoScope® IV controller

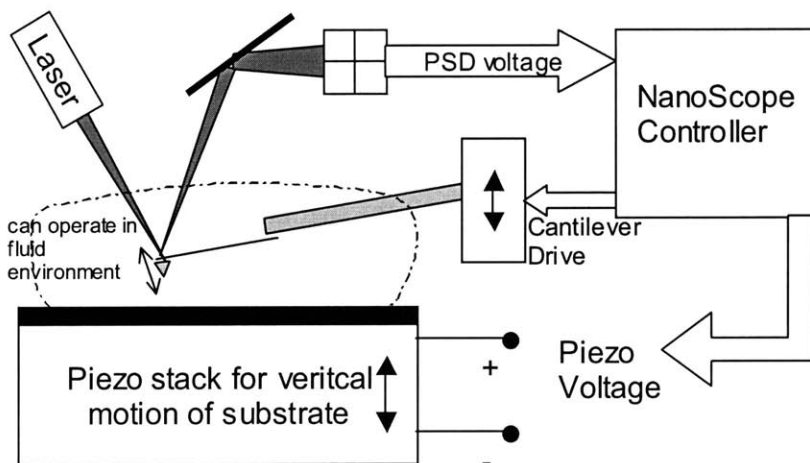
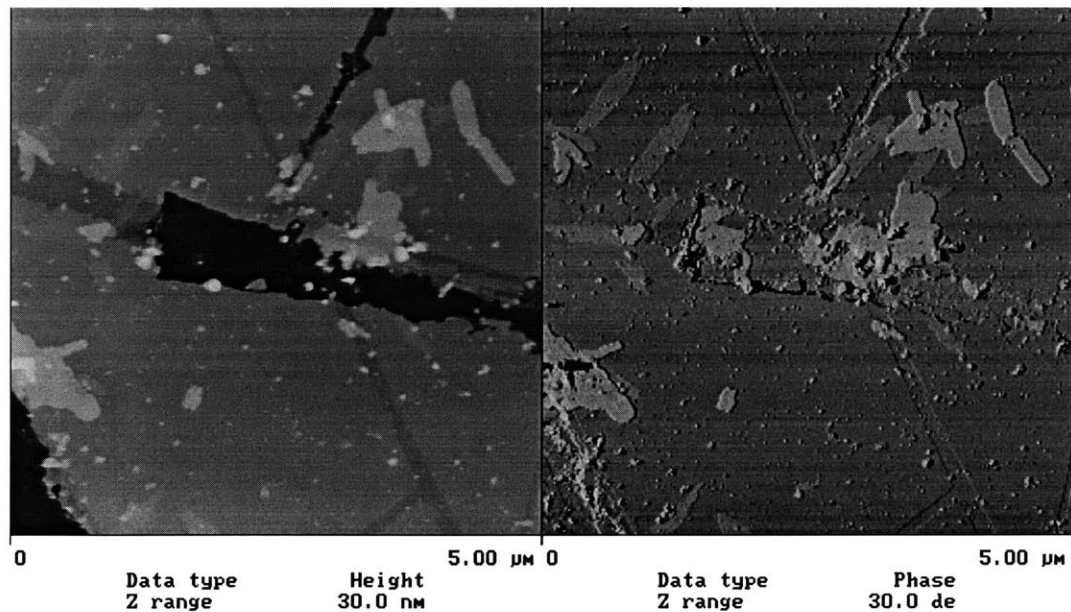


Figure 2-12: Schematic of AFM functional components (not to scale)

The concept behind an AFM is a sensitive force displacement spring system operated in feedback mode with a piezo positioned substrate. A laser beam is focused on the back of a micro cantilever, $L \sim 100 \mu m$, which is monitored by a photo-sensitive diode. The cantilever is engaged on a surface by adjusting the piezo stack until a user-defined static deflection or RMS amplitude of oscillation is achieved. The cantilever is then raster scanned over an area, $< (150 \mu m)^2$, while the controller adjust the piezo voltage to maintain the aforementioned user-defined value.

An example image of un-cleaved Mica is shown in Figure 2-13. This image was acquired in tapping mode, which used the cantilever drive and RMS amplitude as the feedback signal. The image on the left is a gray-scale height image with a full range of 30 nm and an area of $25 \mu m^2$. The image on the right is a gray-scale phase image with a full range of 30° for the same area.



mica.000

Figure 2-13: AFM height and phase image of un-cleaved mica substrate, acquired in tapping mode: $A=25\mu m^2$

This Mica was intentionally not cleaved in order to demonstrate AFM phase imaging. In these particular images, the height and phase look very similar. This is because many changes in

height on the left image are caused by debris, which accordingly has a different phase response. However, the dark lower height regions, in the height image are only outlined in the phase image. This is because the lower regions are scratches on the Mica surface, and should not exhibit a different phase or material property. However, these lower regions are outlined on the phase image because the sudden change in height, high frequency surface characteristics, are detected by the cantilever in phases imaging.

This example image is given to highlight the sensitivity and feedback control of the instrument. As with the SFA, the piezo stack provides *nm* control of the separation between the cantilever and substrate. The oscillating cantilever probe determines the temporal resolution. Given the typical dimensions of the cantilever, Figure 2-14, one can sense *pN* of force with these SPM probes.

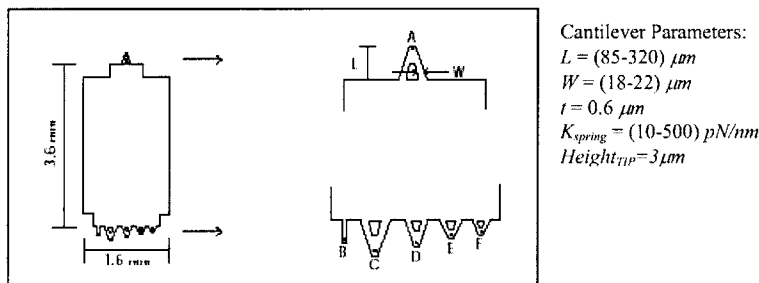


Figure 2-14: Typical cantilever dimensions and properties

The resonant frequencies of these probes can range from kHz to MHz, such that times scales on the order of μs can be probed with this system.

2.3.2 Other research using SPM technology for visco-elastic measurements

The versatility of atomic force microscopy has prompted researchers to employ its service for numerous micro-scaled phenomenon, not excluding visco-elastic effects. Lindsay and O'Shea[25-27] have used driven force modulation techniques to measure solvation forces near interfaces via changes in dissipative mechanisms. Burnham and Wahl[28-30] have used the

AFM to investigate the visco-elastic effects of coatings on substrates and the implications to tapping mode imagery and Friction Force Microscopy (FFM). Specifically related to the influence of a fluid environment on the response of SPM probes, Johannsmann[31] has measured the response of SPM probes near an interface to show the influence and collapse of polymer brushes.

For this thesis, a model relating the fluid's visco-elastic properties to the spectral response of the probe was required. SPM techniques have been demonstrated for quantifying bulk viscosity of fluids by Chen[32] and later by Kirstein[33] and Sader[34, 35]. Figure 2-15 illustrates the analogous concepts for rheological measurements as it relates to the SPM cantilever configuration. By modeling the SPM probe as a Simple Harmonic Oscillator (SHO) interacting with a specific model of a fluid environment, one can use the dynamic response of the SHO in concert with the fluid model to quantify the associated parameters of the fluid.

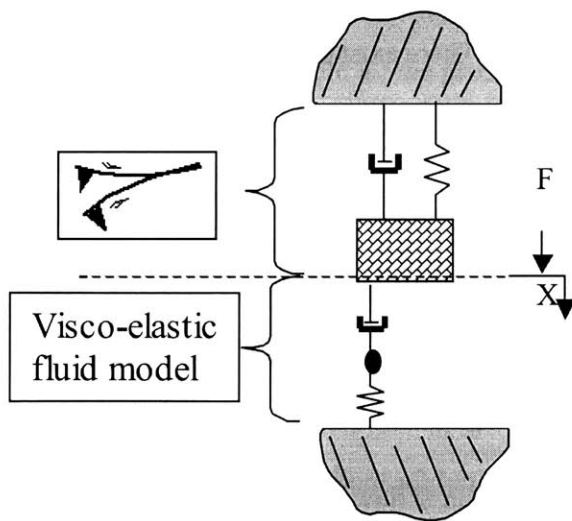


Figure 2-15: Schematic for using dynamic response of SPM probes to quantify properties of a fluid environment

The remaining point to be made is that if this technique is to be useful in the interfacial regime, then driving the cantilever through a range of frequencies would result in non-spectrally uniform amplitudes and large amplitude of oscillation relative to the dimension of interest in the interface, nm. Therefore, this work used thermally driven cantilevers, which will be discussed in detail later, to provide a small, less than 1nm, and uniform perturbation to the fluid environment.

2.4 Research objective

In the pursuit of interfacial rheology, one needs a platform capable of the required temporal and spatial range and resolution to quantify the visco-elastic fluid properties from a bulk regime to the interfacial regime. With the availability and versatility of AFMs and the mounting models and data related to the performance of SPM probes in a fluid environment, the AFM is an attractive platform to exploit.

This thesis discusses the use of thermal oscillations of an SPM probe to quantify the visco-elastic properties of fluids via spectral variations. There exist theoretical models for the Fluid-Structure Interactions (FSI) of vibrating bodies in incompressible viscous mediums[32, 33, 35], and these models serve as effective tools to quantify properties of the surrounding environment. This thesis will discuss how these models were extended to develop visco-elastic FSI models. These analytical models quantify the response of SPM probes in a visco-elastic incompressible medium and have been quantitatively compared with experimental data, obtained from thermally driven SPM cantilevers. The VE-FSI theory required for modeling the probe dynamics in a visco-elastic fluid is outlined and the present limitations, for both the analytical and experimental techniques, are discussed.

Figure 2-16, although premature without any theoretical foundation, illustrates our objective, and will be discussed in complete detail in the results section.

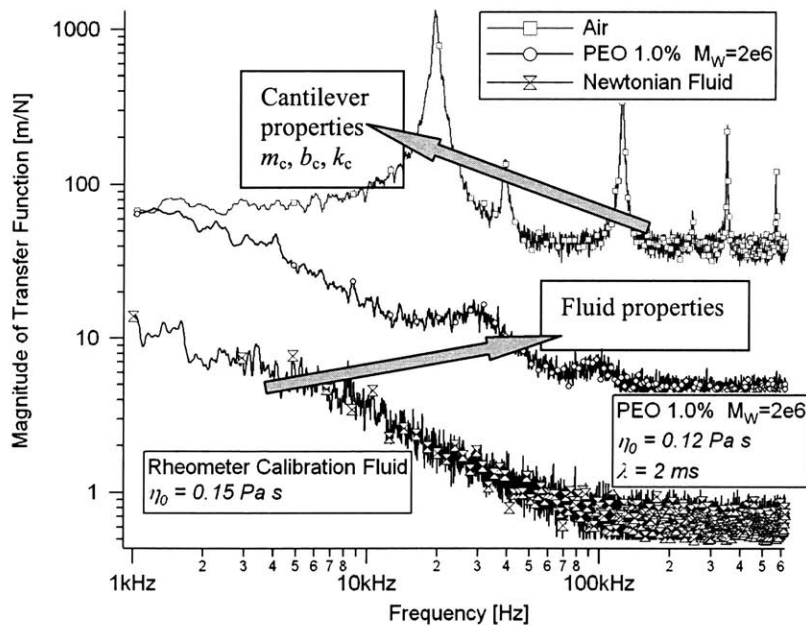


Figure 2-16: Spectral response of SPM cantilever in air, in a Newtonian fluid and in a visco-elastic fluid with similar viscosity. The qualitative differences of the spectral response in the visco-elastic fluid will be quantified to yield rheological properties.

In a typical test, one could first measure the response of the cantilever in air, which could be fit with an appropriate model to yield all the properties of the cantilever. With the cantilever being a known in the system, the spectral response of the probe can now be measured in various fluids and the added effect of the fluid environment quantified to yield the fluid's properties. More specifically, the modes of the cantilever simultaneously sample all the frequencies, including the short-time scale, high frequency, visco-elastic properties. As shown in Figure 2-16, the modal response of the probe is heavily damped in the Newtonian fluid, but the modes are dramatically enhanced in the visco-elastic fluid with similar viscosity.

With continued advances in these analytical theories and increased precision of experimental platforms and techniques, unmasking the physics, hidden in the scales of these complex systems, is only a matter of time. Parallel research efforts, in such areas as micro-

textured surfaces, will, in concert, shed light on the interplay of the confined rheology, micro-scaled surface properties and contact dynamics.

3 Theory

3.1 Thermal excitation

This section will discuss the theory related to the thermal excitation of the cantilevered probe. Deterministic theory, when system components have unique functional descriptions, will be discussed followed by the analogous scenario when system components are described by random processes.

3.1.1 Deterministic theory

Classic system dynamics usually deal with deterministic inputs to a given system, such as the SHO model that is proposed for the cantilevered probe, graphically represented in Figure 3-1.

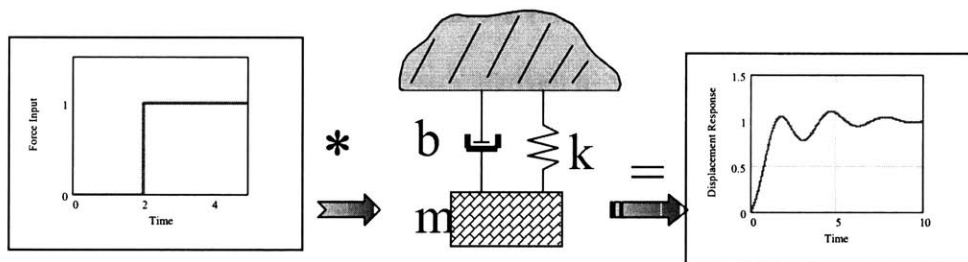


Figure 3-1: Deterministic system response of a Simple Harmonic Oscillator. The input is convolved with the impulse response of the system to yield the time dependent output

The mathematical relation to obtain the response of the system is to convolve the time domain input with the impulse response of the system, (3.1), where $h(t)$ is the response of the system to

and impulse, $\delta(t)$ where $1 = \int_{-\infty}^{\infty} \delta(t) e^{-j\omega t} dt$.

$$x_{in}(t) * h(t) = x_{out}(t) \quad (3.1)$$

It is often mathematically more desirable and practically more useful to think of these systems in the frequency domain, where the description of the system is algebraic, equation (3.2).

$$X_{in}(\omega)H(\omega) = X_{out}(\omega) \quad (3.2)$$

The functions $X(\omega)$ and $H(\omega)$ are the Fourier transforms of the time domain functions. With the simplicity of equation (3.2), if one knows any of the two terms, then the third is easily computed. For instance, if our system were a black box, then by driving the system with a known input and measuring the output, one could compute the transfer function of the black box. If a model existed for the proposed black box, then this model could be fit to the computed transfer function, and determine the model parameters.

3.1.2 Random signal theory: thermal energy

To capitalize on the scale of these probes, they are driven with their inherent thermal energy as defined by the ambient temperature in the experiments. Similar to systems with deterministic inputs, in which one can use Fourier transform methods in lieu of convolution techniques, Figure 3-2 illustrates the method used when systems are subjected to random inputs.

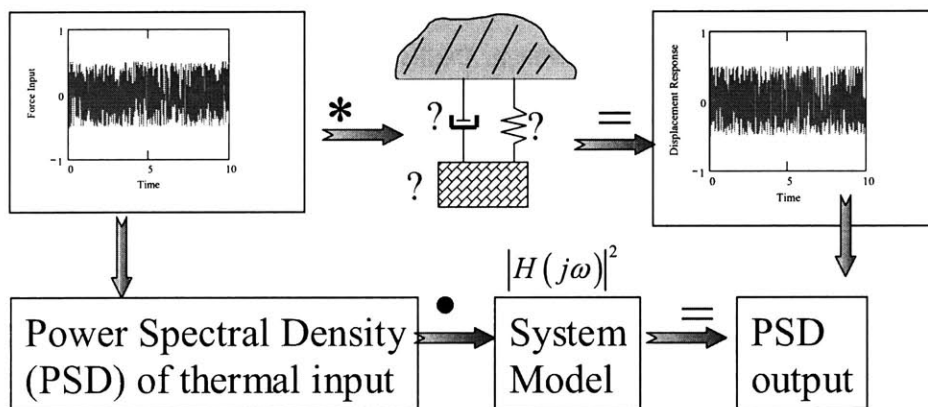


Figure 3-2: System Dynamics with Random Inputs

In the same spirit as with deterministic systems, when the models are viewed in terms of power spectral densities, the solution becomes an algebraic problem as compared to a convolution of random time functions, equation (3.3).

$$S_{in}(\omega) |H(\omega)|^2 = S_{out}(\omega) \quad (3.3)$$

S_{in} and S_{out} are Power Spectral Densities (PSD) with units of W/Hz . As with deterministic systems, with knowledge of any two components in the system equation, the third is readily computed. For the purpose of this work, the system model is illustrated in Figure 3-2, where a model for the input will be developed and by measurements of the output, a system model will be fit to the measured data to determine m_c , b_c , and k_c . The theoretical basis for the thermal input model will be discussed followed by an explanation and justification for how the actual measured response of the cantilever probe was converted to a displacement power spectrum.

3.1.3 Thermal Power Spectral Density

Planck's theory of blackbody radiation[36] states that the allowable energy state of a system is quantized by equation (3.4), where $h = 6.62 \cdot 10^{-34} J \cdot s$ is Planck's constant and ν is the frequency of oscillation.

$$E_n = nh\nu \quad (3.4)$$

Assuming the number of observed energy levels, corresponding to n , obey a Maxwell-Boltzmann distribution in equilibrium

$$N_n \sim e^{-\frac{E_n}{k_B T}} = e^{-\frac{nh\nu}{k_B T}} \quad (3.5)$$

where $k_B = 1.38 \cdot 10^{-23} \frac{J}{K}$ is Boltzmann's constant, and T is the temperature, then the probability of finding a given energy level is the number of levels, N_n , observed for that given energy level divided by the total number of possible energy levels.

$$p(E_n) = \frac{e^{-\frac{nh\nu}{k_B T}}}{\sum_{m=0}^{\infty} e^{-\frac{mh\nu}{k_B T}}} = \frac{y^n}{\sum_{m=0}^{\infty} y^m} = \frac{y^n}{(1-y)} = e^{-\frac{nh\nu}{k_B T}} \left(1 - e^{-\frac{h\nu}{k_B T}} \right) \quad (3.6)$$

$$\left| e^{-\frac{h\nu}{k_B T}} \right| < 1$$

This result is known as the Bose-Einstein probability. To find the statistical expectation, or average, value for the observed energy level, perform the following calculation.

$$\bar{E} = \sum_{n=0}^{\infty} E_n p(E_n) = \frac{h\nu}{e^{h\nu/k_B T} - 1} \quad (3.7)$$

Taking the power series expansion of the exponential in the denominator

$$e^{\frac{h\nu}{k_B T}} = \sum_{m=0}^{\infty} \left(\frac{h\nu}{k_B T} \right)^m \quad (3.8)$$

and assuming $h\nu/k_B T \ll 1$, which is known as the Rayleigh-Jeans limit, one can make a leading order approximation that the average energy is given by equation (3.9).

$$\bar{E} = k_B T \quad (3.9)$$

This assumption is valid at room temperature for frequencies less than 6 THz, which is well beyond the experimental ranges of the system discussed in this thesis. This frequency independent approximation to the thermal energy is the reason thermal energy is often referred to as “white” noise for many practical applications.

To understand the driving force, which results in this distribution of energy per mode, consider the analogous electrical circuit shown in Figure 3-3.

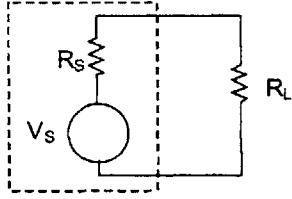


Figure 3-3: Electrical analogy of thermal driving energy. The driving voltage, thermal power, is desired so that the response of the load resistor, SPM probe, can be modeled.

Consider the power delivered to R_L in this circuit.

$$P_L = \frac{V_L^2}{R_L} = \frac{1}{R_L} \left(\frac{V_s \cdot R_L}{R_s + R_L} \right)^2 \quad (3.10)$$

The power delivered to the load resistor is maximized, $\partial P_L / \partial R_s = 0$, with respect to R_s when

$R_L = R_s = R$ such that

$$P_L = \frac{V_s^2}{4R} \quad (3.11)$$

Power spectral densities are defined as

$$S_L \equiv \frac{\partial P_L}{\partial \nu} \quad (3.12)$$

Using equation (3.9) for the energy of a system at a given temperature, the power in the load resistor is given by

$$P_L = k_B T (\Delta \nu) \quad (3.13)$$

or by substituting into equation (3.11)

$$P_s = 4k_B T (\Delta \nu) \Rightarrow (V_s)^2 = 4k_B T R (\Delta \nu) \quad (3.14)$$

Therefore, the source voltage power spectral density of the driving thermal energy is given by

$$S_{th_V} = \frac{\partial (V_s)^2}{\partial \nu} = 4k_B T R \text{ or } S_{th_P} = \frac{\partial P_{th}}{\partial \nu} = 4k_B T \quad (3.15)$$

or equivalently in force and velocity variables,

$$S_F = 4k_b T b \quad (3.16)$$

where b is the force-velocity dampening ratio, and S_F has units of N^2/Hz .

Equation (3.16) provides S_{in} for equation (3.3). Only the PSD of the output, which will be measured, is required to solve for the system response, $|H(\omega)|^2$. It will be shown, in the experimental section, that $x(t)$ will be measured for the cantilever deflection. To compute S_{out} from this time signal we use the Wiener-Khinchin theorem, which states that the PSD and auto-correlation function, $\rho(\tau)$, are a Fourier transform pair.

$$\begin{aligned} S_x(\omega) &= \mathfrak{F}[\rho_x(\tau)] = \int_{-\infty}^{\infty} \rho_x(\tau) e^{-j\omega\tau} d\tau \\ \rho_x(\tau) &= \mathfrak{F}^{-1}[S_x(\omega)] = \frac{1}{2\pi} \int_{-\infty}^{\infty} S_x(\omega) e^{j\omega\tau} d\omega \end{aligned} \quad (3.17)$$

Where the auto-correlation function is defined by equation (3.18)

$$\rho(\tau) = \lim_{T \rightarrow \infty} \frac{1}{T} \int_{-T/2}^{T/2} x(t)x(t+\tau) dt \quad (3.18)$$

Strictly speaking, equation (3.17) is only valid provided $x(t)$ is an ergodic random variable, which means that the time average value is equivalent to the ensemble average over different occurrences[36].

It is not computationally efficient to compute auto-correlations and then Fourier transform the results, but if we consider the following argument

$$\begin{aligned} S_x(\omega) &= \mathfrak{F}[x(t) * x^*(-t)] = (X)(X)^* = |X|^2 \\ \text{where } X(\omega) &= \mathfrak{F}[x(t)] \end{aligned} \quad (3.19)$$

then one sees that only the Fourier transform of the time signal is required, which is computationally efficient, comparatively. A useful consequence of (3.17), which will be used later, is that

$$\rho(0) \equiv x_{rms}^2 = \frac{1}{2\pi} \int_{-\infty}^{\infty} S_x(\omega) d\omega = 2 \int_0^{\infty} S_x(f) df \quad (3.20)$$

which states that the integral of S_x over all frequencies yields x_{rms}^2 .

3.2 Beam Dynamics

A model for S_{in} and a method for computing S_{out} has been presented. Therefore, $|H(\omega)|^2$ can now be computed, the details of which are discussed in chapter 4. The only remaining task is to develop a model for the beam dynamics and FSI such that analytical parametric models can be compared to the measured data.

3.2.1 Derivation and Solution of Euler-Bernoulli beam equation

Figure 3-4 shows the relevant parameters and coordinate system used for solving the beam dynamics.

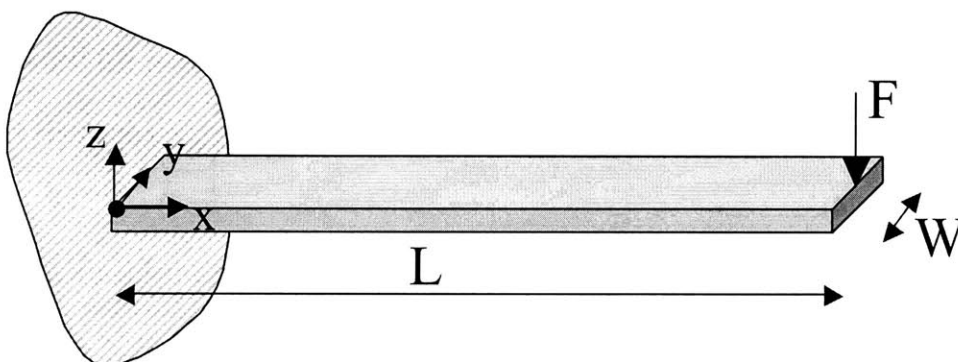


Figure 3-4: Schematic and dimensions used for solution to cantilever bending and dynamics

To develop a differential equation for the dynamics, consider the differential volume element depicted in Figure 3-5[37].

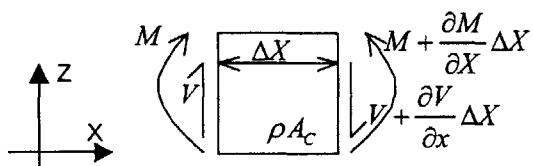


Figure 3-5: Differential beam element

If one sums the forces in the Z direction and sums the moments about the center of mass of the element, then by taking the limit as $\Delta X \rightarrow 0$, equation (3.21) and (3.22) result.

$$\sum F_y = ma \Rightarrow \rho A_c \frac{\partial^2 w}{\partial t^2} = -\frac{\partial V}{\partial X} \quad (3.21)$$

$$\sum M_{cm} = 0 \Rightarrow 0 = \frac{\partial M}{\partial X} - V - \frac{\partial V}{\partial X} \left(\frac{\Delta X}{2} \right) \quad (3.22)$$

$\left[\lim_{\Delta X \rightarrow 0} \right]$

Differentiating equation (3.22) and equating to equation (3.21) the Bernoulli-Euler beam equation is obtained.

$$-\rho A_c \frac{\partial^2 w}{\partial t^2} = \frac{\partial^2 M}{\partial X^2} = \frac{\partial^2}{\partial X^2} \left(\frac{EI}{R} \right) \approx \frac{\partial^2}{\partial X^2} \left(EI \frac{\partial^2 w}{\partial X^2} \right) \quad (3.23)$$

The approximate equal sign simply serves as a reminder that using $1/R = \partial^2 w / \partial x^2$ is valid only for small deflections, such that $\partial w / \partial x \ll 1$. The associated boundary conditions for equation (3.23) are given in equation (3.24).

$$\begin{aligned} w|_{x=0} = 0, \quad \frac{\partial w}{\partial x}|_{x=0} = 0 \\ \frac{\partial^2 w}{\partial x^2}|_{x=L} = 0, \quad \frac{\partial^3 w}{\partial x^3}|_{x=L} = 0 \end{aligned} \quad (3.24)$$

Solving equation (3.23) using separation of variables, $w(x,t) = \chi(x)T(t)$, results in the following two differential equations.

$$\begin{aligned} \frac{\partial^2 T}{\partial t^2} + \omega^2 T &= 0, \text{ where } \omega^2 = \text{constant} \\ \frac{\partial^4 X}{\partial X^4} - \gamma^4 X &= 0, \text{ where } \gamma^4 = \frac{\omega^2}{a^2} \text{ and } a = \sqrt{\frac{EI}{\rho A_c}} \end{aligned} \quad (3.25)$$

The associated solutions to these differential equations are given by equation (3.26).

$$\begin{aligned} T(t) &= A \cos(\omega t) + B \sin(\omega t), \text{ } A \text{ and } B \text{ are constants} \\ X(X) &= \frac{1}{2} \left[\left(\cos(kX) - \cosh(kX) \right) - \frac{(\cos(kL) + \cosh(kL))}{(\sin(kL) + \sinh(kL))} (\sin(kX) - \sinh(kX)) \right] \end{aligned} \quad (3.26)$$

where

$$\cos(k_j L) \cosh(k_j L) = (-1) \quad (3.27)$$

and

$$k_j = \sqrt{\frac{\omega_j}{a}} \quad (3.28)$$

Equation (3.27) results in an infinite set of solutions for $X_j(X)$, where the first four terms are

$$k_j L = \{1.875, 4.694, 7.855, 10.996, \dots\}$$

such that the corresponding angular frequencies are given by equation (3.29).

$$\omega_j = \sqrt{\frac{EI}{\rho A}} \left[\frac{(k_j L)}{L} \right]^2 \quad (3.29)$$

and the complete solution to the response of the beam is given by equation (3.30).

$$w(x,t) = \sum_j X_j(X) T_j(t) \quad (3.30)$$

Figure 3-6 shows the analytical results, equation (3.26), for the first four spatial modes allowed for the cantilevered beam.

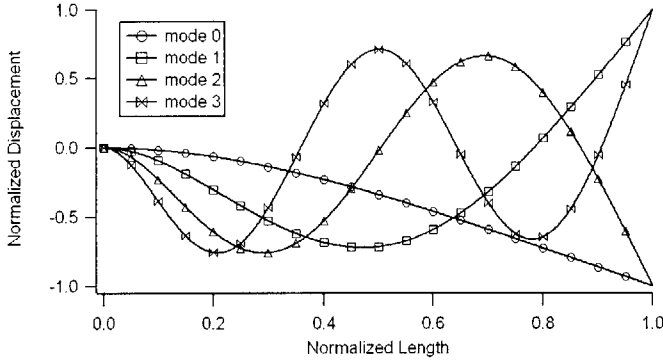


Figure 3-6: Spatial mode solution to Euler-Bernoulli beam equation. The x and y axis of this plot have been normalized by the length of the beam and maximum tip deflection, respectively.

As stated previously, a SHO model was used to capture the behavior of the cantilevered probe. To model as a SHO one needs to think about how the beam solutions translate to mass, spring and dampening terms. Since discussion, in the literature, regarding probe dynamics is almost always restricted to the fundamental frequency, consider the following discussion.

Similar to the dynamic case above, statically loaded solutions to equation (3.31), may be obtained and the resulting stiffness computed from equation (3.32).

$$\frac{-M}{EI} = \left(\frac{\partial^2 w}{\partial X^2} \right) = \frac{F(L-X)}{EI} \quad (3.31)$$

$$k_{eff} = \frac{F}{w(L)} = \frac{3EI}{L^3} \quad (3.32)$$

Noting that for a SHO one has the relation $\omega_0 = \sqrt{\frac{k_{eff}}{m_{eff}}}$, then by rearranging equation (3.29), the effective mass of the first mode may be computed by equation (3.33) and (3.34).

$$\omega_0 = \sqrt{\frac{EI}{\rho A} \left[\frac{(k_0 L)}{L} \right]^2} = \sqrt{\frac{k_{eff}}{3m_c}} (1.875)^2 = \sqrt{\frac{k_{eff}}{m_c (0.24)}} \quad (3.33)$$

$$m_{eff} = m_c (0.24) \quad (3.34)$$

More details will be discussed later, but to establish an order or magnitude, the typical values for the SHO parameters were: $k = 0.2 \text{ N/m}$, $m = 10^{-12} \text{ kg}$ and $b = 10^{-8} \frac{\text{Ns}}{\text{m}}$. The dampening value used for beam dampening was obtain from a paper by Hosaka[38], in which combined dissipative effects of internal friction and air drag was modeled.

For a more general result that includes higher modes, re-consider the discussion above from an energy perspective[37]. Compute the elastic strain energy in the beam, or the equivalent work required to deform the beam into the corresponding mode. Recall the first law of thermodynamics.

$$E = W_{in} = \int F dx \quad (3.35)$$

Considering the energy stored in an elastic solid

$$E = \int_0^{x^*} (\sigma_{xx} dy dz) (d\varepsilon_{xx} dx) \quad (3.36)$$

$$E = \int \underbrace{\int_0^{x^*} (\sigma_{xx} d\varepsilon_{xx})}_{\text{strain energy density}} (dV) \quad (3.37)$$

Therefore, for a hookean solid, the strain energy density, E_v , is given by equation (3.38).

$$E_v = E \frac{\varepsilon_{xx}^2}{2} = \frac{\sigma_{xx} \varepsilon_{xx}}{2} \quad (3.38)$$

For a Bernoulli-Euler beam, the strain energy density is given by equation (3.39).

$$E_v = \frac{1}{2} \left\{ Ez \frac{\partial^2 w}{\partial x^2} \right\} \left\{ z \frac{\partial^2 w}{\partial x^2} \right\} \quad (3.39)$$

$$E = \int_V \frac{E}{2} z^2 \left\{ \frac{\partial^2 w}{\partial x^2} \right\}^2 (dx dA) = \int_x \frac{E}{2} \underbrace{\left\{ \int z^2 dA \right\}}_{I_x} \left\{ \frac{\partial^2 w}{\partial x^2} \right\}^2 (dx) = \int_0^L \frac{EI}{2} \left\{ \frac{\partial^2 w}{\partial x^2} \right\}^2 dx \quad (3.40)$$

To compute the equivalent lumped parameter model, consider a force applied at the end of the beam such that

$$E_j = \int_0^L \frac{EI}{2} \left(\frac{\partial^2 w_j}{\partial x^2} \right)^2 dx = \frac{1}{2} k_{Cj} [w(L)]^2 \quad (3.41)$$

Noting that $w(L) = 1$, the beam's modal stiffness is defined by equation (3.42).

$$k_{Cj} = EI \int_0^L \left(\frac{\partial^2 w_j}{\partial x^2} \right)^2 dx \quad (3.42)$$

Using equation (3.42) in conjunction with (3.29), the modal masses can be computed.

$$m_j = \frac{k_{Cj}}{\omega_j^2} = \int_0^L \frac{\partial^2 w}{\partial x^2} dx (\rho A) \left(\frac{L}{k_j L} \right)^4 \quad (3.43)$$

The result of equation (3.43) is shown in Table 3-1.

Mode #	j=0	j=1	j=2	j=3
m_j/m_c	0.25001	0.25000	0.25006	0.24999

Table 3-1: Ratio of effective modal mass to the mass of the static cantilever

As noted previously, modal dampening was assumed to be $\sim 10^{-8}$ Ns/m for all modes, which was both a reference value in the literature and an experimentally observed value, as will be shown later when the results are discussed.

With values for m_j , b_j and k_j , one can think about the spectral response of the SPM probe to thermal energy. Since all properties are uniformly distributed along the beam as compared to localized property variation that would produce traveling waves, the response of the beam is captured by a superposition of the various modes, equation (3.44).

$$\left| \frac{x}{F} \right|^2 = \sum_j \frac{1}{(k_{c_j} - m_j \omega^2)^2 + (b_j \omega)^2} \quad (3.44)$$

Figure 3-7 shows a typical theoretical response for the SPM probes used in this research.

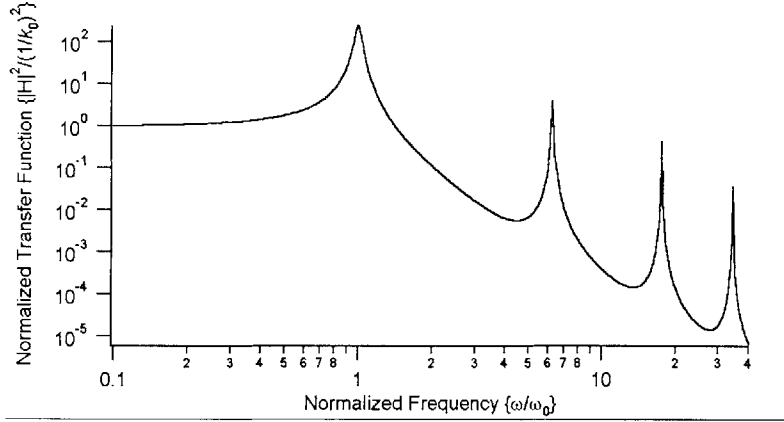


Figure 3-7: Typical normalized frequency response of cantilevered probe

Experimental comparison will be shown later, once there has been a discussion on the experimental procedure. In addition, recall that the measured S_{out} depends on $S_{in} = 4k_B T b$, where b will depend on the fluid environment. Therefore, the response of the probe in a fluid will also be postponed until the FSI models have been developed.

3.2.2 Effect of viscous/elastic fluid environment on spectral response

To understand the influence of a fluid environment, it is useful to think about the influence, per unit length, of a uniformly distributed fluid environment with a given m , b , and k effect.

Following the same procedure used to obtain equation (3.23) one will obtain the following result, where the prime denotes per unit length.

$$-\left((\rho_c A_c + m'_{fluid}) \frac{\partial^2 w}{\partial t^2} + b'_{fluid} \frac{\partial w}{\partial t} \right) = \frac{\partial^2}{\partial X^2} \left(EI \frac{\partial^2 w}{\partial X^2} \right) + k'_{fluid} w \quad (3.45)$$

Following the same solution procedure as before, the analogous result for equation (3.29) is found to be equation (3.46).

$$\Omega_j = \left\{ \left(\omega_j^2 + \frac{k'_{fluid}}{\rho_c A_c} \right) - \left(\frac{1}{4} \right) \left(\frac{b'_{fluid}}{\rho_c A_c + m'_{fluid}} \right) \right\}^{\frac{1}{2}} \quad (3.46)$$

Equation (3.46) illustrates how an increase in m'_{fluid} and b'_{fluid} tend to reduce resonant frequencies while k'_{fluid} tends to increase the frequencies. Similarly, k'_{fluid} and b'_{fluid} increase and decrease the modal quality, respectively. It is also important to note that equation (3.46) also has the correct asymptotic behavior in the absence of a fluid such that

$$\Omega_j = \omega_j \quad (3.47)$$

This argument serves to qualitatively predict the effect of a fluid environment on a SPM probe. The following section takes a rigorous approach to quantify the effects.

3.3 Fluid Structure Interaction (FSI)

For the purpose of our research, a model is required, which incorporates effects of measurable fluid properties (η, ρ, λ , etc.) on observed spectral shifts of SPM probes. This section outlines the analytics associated with quantifying the effects of FSI on the measurable dynamics of the probe. The first section considers the effect of a purely viscous fluid and relates this added fluid effect to equivalent lumped model parameters: m_{add} and b_{add} . The last portion shows how this research has extended this analytical approach to include the effect of viscoelasticity and relates this effect to equivalent lumped parameters.

3.3.1 Viscous FSI

For modeling reasons, one would like to eliminate sharp edges that exist in a rectangular beam. Consequently, many researchers model such geometries as cylindrical, where

$D_{cylinder} = W_{beam}$. This work adopted the same approximation, and will be justified by way of experimental validation

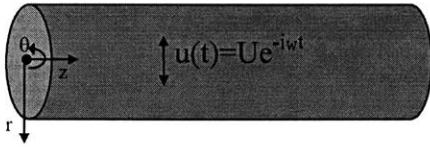


Figure 3-8: Cylindrical Approximation for fluid structure interaction model. Model is an infinite cylinder translating normal to its z-axis with a given oscillating velocity.

As shown in Figure 3-8, an infinitely long, $\frac{D}{L} \ll 1$, cylinder translates normal to its z-axis with a velocity given by equation (3.48).

$$\delta(t) = U \left(\frac{-j}{\omega} \right) e^{-j\omega t} \quad (3.48)$$

To capture the fluid dynamics we use the Navier-Stokes equation for an incompressible viscous fluid, equation (3.49).

$$\frac{\partial \vec{V}}{\partial t} + \vec{V} \cdot \nabla \vec{V} = -\frac{\nabla p}{\rho} + \nu \nabla^2 \vec{V} \quad ; \quad \nabla \cdot \vec{V} = 0 \quad (3.49)$$

If one takes the curl of equation (3.49) and makes use of some common vector identities and substitutes the continuity equation, equation (3.50) and (3.51) result.

$$\frac{\partial (\vec{\nabla} \times \vec{V})}{\partial t} + \underbrace{\vec{\nabla} \times \left\{ \frac{1}{2} \underbrace{\vec{\nabla} |\vec{V}|^2}_{\vec{\nabla} \times \vec{\nabla} \cdot \vec{V} = 0} - \vec{V} \times \vec{\nabla} \times \vec{V} \right\}}_{\vec{\nabla} \times \vec{\nabla} \cdot \vec{V} = 0} = - \underbrace{\vec{\nabla} \times \left(\frac{\vec{\nabla} p}{\rho} \right)}_{\vec{\nabla} \times \vec{\nabla} \cdot \vec{V} = 0} + \nu \nabla^2 (\vec{\nabla} \times \vec{V}) \quad (3.50)$$

$$\frac{\partial(\bar{\nabla} \times \bar{V})}{dt} + \left\{ \bar{\nabla} \times \bar{V} \cdot \bar{\nabla} \bar{V} - (\bar{V} \cdot \bar{\nabla})(\bar{\nabla} \times \bar{V}) + \underbrace{\bar{V} \cdot \bar{\nabla} \cdot (\bar{\nabla} \times \bar{V})}_{\bar{\nabla} \cdot (\bar{\nabla} \times \bar{V}) = 0} - (\bar{\nabla} \times \bar{V}) \cdot \underbrace{(\bar{\nabla} \times \bar{V})}_{\text{continuity}} \right\} = \nu \nabla^2 (\bar{\nabla} \times \bar{V}) \quad (3.51)$$

Recalling the definition for vorticity

$$\bar{\omega}_v = \bar{\nabla} \times \bar{V} \quad (3.52)$$

equation (3.51) becomes the Helmholtz vorticity equation, (3.53).

$$\frac{D(\bar{\omega}_v)}{Dt} = (\bar{\omega}_v \cdot \bar{\nabla}) \bar{V} + \nu \nabla^2 (\bar{\omega}_v) \quad (3.53)$$

One can then compare the orders of magnitude of the time derivative on the left side of the equation with the two convective terms on the left side.

$$\frac{V}{L\tau}, \frac{V^2}{L^2}, \frac{V^2}{L^2} \Rightarrow \frac{V^2}{L^2} \Big/ \frac{V}{L\tau} = \frac{V}{L\tau} \quad (3.54)$$

For oscillatory displacement of a cylinder, $V \rightarrow a\omega$ and $L \rightarrow R$, where a is the amplitude of displacement and R is the radius of the cylinder. Therefore, for small amplitude motion, which is appropriate for thermal oscillations, the governing fluid equation becomes

$$\frac{\partial}{\partial t}(\bar{\omega}_v) = \nu \nabla^2 (\bar{\omega}_v) \quad (3.55)$$

In general, the motion of a fluid can be described by

$$\bar{V} = \bar{\nabla}\Phi + \bar{\nabla} \times \bar{A}, \quad \Phi \equiv \text{scalar potential and } \bar{A} \equiv \text{vector potential} \quad (3.56)$$

in 2-D axis-symmetric case

$$\bar{A} = \Psi(r, \theta, t) \hat{k} \quad (3.57)$$

Therefore,

$$\bar{\omega}_v \rightarrow \omega_z = -\nabla^2 \Psi \quad (3.58)$$

or

$$\omega_z = -\nabla^2 \Psi = -\nabla^2 (\psi e^{j\omega t}) \quad (3.59)$$

where ψ is the commonly used stream function, such that the fluid velocities are given by equation (3.60).

$$V_r = \frac{1}{r} \frac{\partial \psi}{\partial \theta} \text{ and } V_\theta = -\frac{\partial \psi}{\partial r} \quad (3.60)$$

Finally, for 2-D, axis-symmetric, small amplitude oscillatory motion, equation (3.55) becomes equation (3.61).

$$\nabla^4 \psi - \frac{j\omega}{\nu} \nabla^2 \psi = 0 \quad (3.61)$$

Separation of variables, in cylindrical coordinates, results in the following general solution.

$$\psi(r, \theta) = \left[AH_\omega^{(1)}(kr) + \underbrace{BH_\omega^{(2)}(kr)}_{\substack{\text{radiation condition:} \\ \text{no incoming waves} \\ \text{at } r=\infty}} \right] [C \cos(\omega\theta) + D \sin(\omega\theta)] \quad (3.62)$$

$H_\omega^{(1)}(kr)$ is the Hankel function of order ω and $k = \sqrt{-j\omega/\nu}$.

Mathematical solutions, for well formulated cylindrical problems, have been worked out by Chen[32] and other subsequent researchers[33-35, 39]. In particular, if the following boundary conditions, equation (3.63), are applied to the general solution

$$\begin{aligned} \nabla \cdot \vec{V} &= 0 \\ \frac{U}{\omega} &\ll D \\ R_{\text{system boundary}} &= \infty \\ \vec{V}_{r=R} &= \vec{V}_{\text{cylinder}} \end{aligned} \quad (3.63)$$

then the solution becomes

$$\psi(r, \theta) = U(-RH(\alpha_r))\sin(\theta) \quad (3.64)$$

where

$$H(\alpha) = \left[1 + \frac{K_1(\alpha)}{\alpha K_0(\alpha)} \right] \quad (3.65)$$

and

$$\alpha = \sqrt{j(\text{Re}_\omega)} \quad (3.66)$$

$K_n(\alpha)$ is the modified Bessel function of the 2nd kind of order n and Re_ω is the kinematic Reynolds number, defined by equation (3.67).

$$\text{Re}_\omega = \frac{\rho\omega D^2}{4\eta} \quad (3.67)$$

With a solution for the velocity field, the forces opposing the motion of the cylinder need to be calculated. The pressure acting on the surface is approximately equal to the pressure acting on the surface if the fluid were inviscid. Since this is based on the argument that the viscous boundary layer is thin compared to the body dimensions, this approximation becomes increasingly more accurate as $\sqrt{\nu}/R \rightarrow 0$ or $\text{Re}_\omega \rightarrow \infty$. Euler's equation, neglecting gravity, then becomes

$$\frac{\partial}{\partial t}(\nabla\Psi) + \underbrace{\frac{1}{2}\nabla|V|^2}_{\substack{\text{neglect} \\ \left(\frac{(\omega R)^2}{a\omega^2} \right) \ll 1}} = \frac{-\nabla P}{\rho} \quad (3.68)$$

such that

$$P(r = R, \theta, t) = -\rho \frac{\partial\Psi}{\partial t} = \rho URH(\alpha)\sin(\theta)j\omega e^{j\omega t} \quad (3.69)$$

To compute the force, one needs to integrate the resulting pressure over the surface of the cylinder.

$$F_{\delta}(t) = \int_0^{2\pi} P(r = R, \theta, t) \sin(\theta) R d\theta L \quad (3.70)$$

The net force opposing the motion of the cylinder is then given by equation (3.71).

$$F_{\delta}(t) = U \rho \underbrace{\left[\int_0^{2\pi} \sin(\theta)^2 d\theta \right]}_{m_{displaced} = \pi} R^2 L H(\alpha) j\omega e^{j\omega t} \quad (3.71)$$

The in-phase and out-of-phase components are given by equation (3.72) and (3.73).

$$\text{Im}\{F_{\delta}(t)\} = U m_{disp} \omega e^{j\omega t} \text{Re}\{H(\alpha)\} \quad (3.72)$$

$$\text{Re}\{F_{\delta}(t)\} = -U m_{disp} \omega e^{j\omega t} \text{Im}\{H(\alpha)\} \quad (3.73)$$

Recall that the model for the SPM probe was a SHO model with given m , b , and k . It is desired to relate the effect of the fluid to equivalent lumped parametric terms, m_{add} and b_{add} in Figure 3-9, such that the response of the probe can be characterized by equation (3.74).

$$\left| \frac{X}{F} \right|^2 = \sum_j \frac{1}{(k_j - (m_j + m_{add})\omega^2)^2 + ((b_j + b_{add})\omega)^2} \quad (3.74)$$

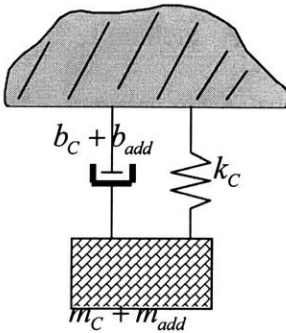


Figure 3-9: Relate the fluid structure interaction model to equivalent parameters in the SHO model for the probe

Consider the force response from a mass and damper, equation (3.75).

$$F(t) = j\omega U m_{add} e^{j\omega t} + U b_{add} e^{j\omega t} \quad (3.75)$$

To obtain an equivalent lumped parameter expression for the fluid effect, simply equate the real and imaginary parts of (3.75) and (3.71): $\text{Im}\{F_\delta\} = \text{Im}\{F\}$ and $\text{Re}\{F_\delta\} = \text{Re}\{F\}$.

$$m_{add} = \underbrace{\rho_{fluid}(\pi R^2 L)}_{m_{disp}} \text{Re}\{H(\alpha)\} \quad (3.76)$$

$$b_{add} = -\underbrace{\rho_{fluid}(\pi R^2 L)}_{m_{disp}} \omega \text{Im}\{H(\alpha)\} \quad (3.77)$$

To gain some insight into the forms of these relations, consider the large Re_ω approximation for $H(\alpha)$.

$$H(\alpha) = \left[1 + 4 \sqrt{\frac{2}{\text{Re}_\omega}} \right] + j \left[-4 \sqrt{\frac{2}{\text{Re}_\omega}} \right] \quad (3.78)$$

such that

$$m_{add} \sim \text{Re}\{H(\alpha)\} \quad (3.79)$$

$$b_{add} \sim -\omega \text{Im}\{H(\alpha)\} \quad (3.80)$$

Figure 3-10 shows the frequency dependence of m_{add} and b_{add} .

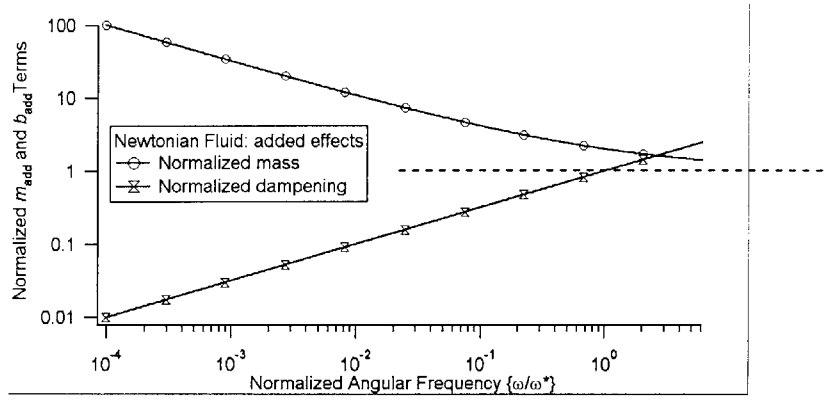


Figure 3-10: Added mass and dampening terms as a function of frequency. The normalized mass and dampening were defined as m_{add}/m_{disp} and $b_{add}/m_{disp}\omega^*$, respectively. The normalized frequency was defined as ω/ω^* .

$\omega^* = (32\eta)/(\rho D^2)$ was determined by setting the real part of $H(\alpha)$ equal to zero. The normalizing factor for the dissipation is $b^* = m_{disp}\omega^* = 32\pi\eta L$. The dashed line is to indicate that the added mass asymptotically approaches the added mass of the displaced fluid as high frequencies.

3.3.2 Visco-Elastic FSI

Recall that the focus of this research was to quantify the visco-elastic fluid properties from the response of SPM probes. Therefore, visco-elastic fluid properties needed to be incorporated into the FSI models. As noted in the background, visco-elasticity is often included by making use of a complex viscosity, which for a given constitutive relation such as the Maxwell model, equations (3.82) and (3.83) were defined.

$$\eta^* = \eta' - j\eta'' \quad (3.81)$$

$$\eta' = \frac{\eta_0}{1 + (\lambda_1\omega)^2} \quad (3.82)$$

$$\eta'' = \frac{\eta_0(\lambda_1\omega)}{1 + (\lambda_1\omega)^2} \quad (3.83)$$

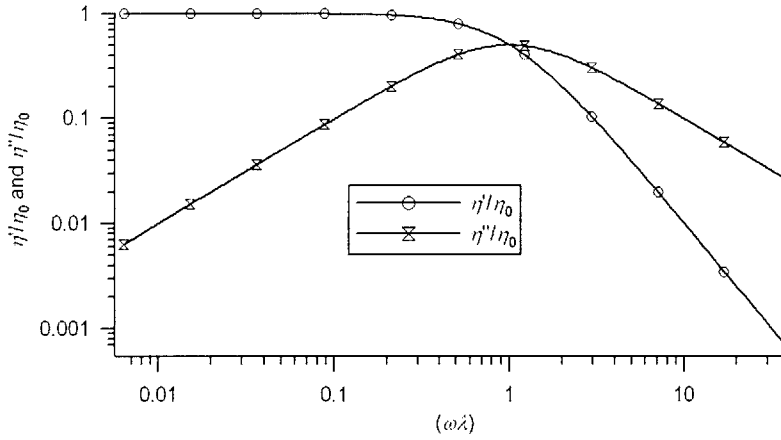


Figure 3-11: Normalized plots of η' and η'' for a Maxwell fluid

Figure 3-11 shows plots of η' and η'' normalized to η_0 as a function of $\lambda\omega$.

The work presented in this thesis made use of η^* to include visco-elasticity into the FSI models via a complex kinematic Reynolds number.

$$\text{Re}_\omega^* = \frac{\rho D^2 \omega}{4\eta^*} \Rightarrow \alpha^* = \sqrt{j \text{Re}_\omega^*} \quad (3.84)$$

Including this in the aforementioned FSI resulted in a newly defined function for $H(\alpha)$.

$$H^*(\alpha) = 1 + \frac{K_1(\alpha^*)}{\alpha^* K_0(\alpha^*)} \quad (3.85)$$

The superscripts will be dropped from future references, since $H(\alpha)$ is always complex and the “*” was only used here to complete the analogy.

Now there exists a new model to connect visco-elastic fluid properties to changes in spectral response of SPM probe. As before, lumped parameters can be defined for the fluid effect. However, since the inertial and elastic responses have the same phase, they are not explicitly separable. Analogous to the purely viscous added terms shown in Figure 3-10, equation (3.86) and (3.87) give the relations for the added terms in a visco-elastic fluid

$$\left(m_{add} - \frac{k_{add}}{\omega^2} \right) = m_{disp} \operatorname{Re}\{H(\alpha)\} \quad (3.86)$$

$$(b_{add}) = (-\omega) m_{disp} \operatorname{Im}\{H(\alpha)\} \quad (3.87)$$

Therefore, the parenthetic term in equation (3.86) will simply be referred to as m_{add} , but the effect of elasticity in the fluid on this term is evident when the results are plotted in Figure 3-12.

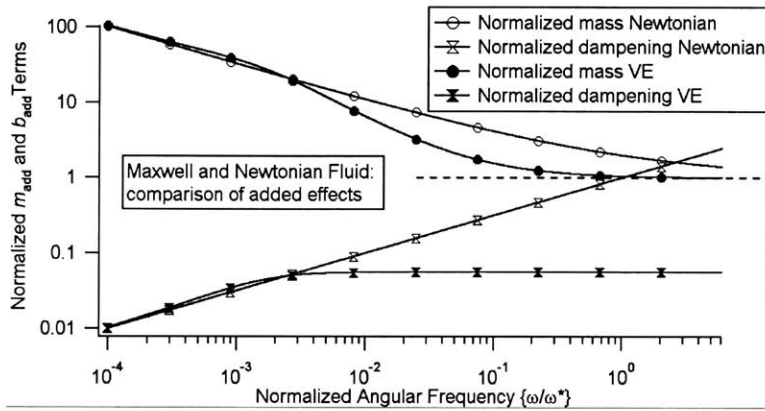


Figure 3-12: Added mass and dampening terms for a Maxwell fluid ($\eta_0=0.008Pa\ s$ and $\lambda=0.8ms$) compared to that of a Newtonian fluid with the same viscosity.

There are some notable difference between the Newtonian theory and this new visco-elastic theory that has been put forth in this thesis. The two possess completely different frequency dependant behavior. The most apparent deviation is the order of magnitude changes in the dissipative term, which has notable effects on the model response of the SPM probes. In fact, a reduction in m_{add} and b_{add} will tend to increase modal frequencies and qualities, as equation (3.46) demonstrated. This is the exact effect that was discussed in the motivation section. The higher modes of the probe will perturb the fluid in a more elastic region and the resulting modal response will reflect this fact, allowing one to quantify the visco-elastic properties of the fluid.

3.3.3 Scaling effects

For completeness, it needs to be noted that the above theory is valid only for a fluid environment in which there are no boundaries near the oscillating probe, Figure 3-13.

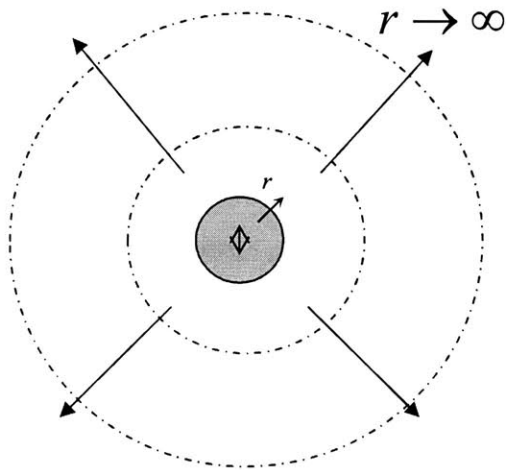


Figure 3-13: Infinite Boundary Condition for fluid structure interaction model

From a practical perspective, this requires that any boundaries do not exist within a couple diameters of the probe. However, to be used as an interfacial probe, Figure 3-14 is a more accurate representation of the probe environment.

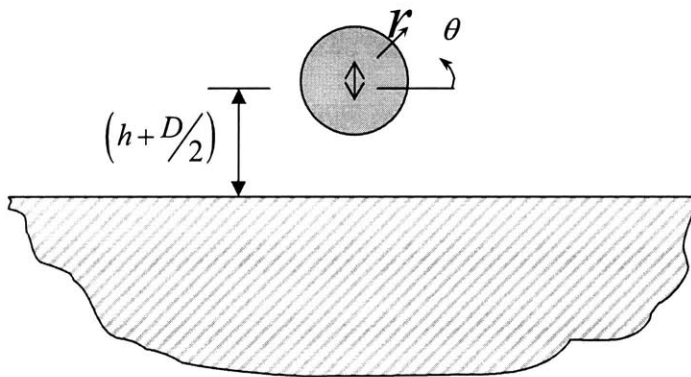


Figure 3-14: Planar viscous boundary condition for fluid structure interaction model

Analytically, this is significantly more complicated than the aforementioned case. In the progress of this work, many possible solution techniques were attempted ranging from eccentric translating cylinders to methods of imaging across the symmetric viscous boundary. Although not included in this thesis, methods such as Fourier-Bessel analysis deal with geometries in which cylindrical and planar boundary conditions are encountered and you have both transmitted and reflected waves propagating from the vibrating body. Experimentally, it may be more practical to calibrate out the effect of the surface. Once a platform and theoretical model is established for the bulk visco-elastic response of the probe in the fluid, which is the context of this thesis, one could envision running experiments to isolate the effect of the boundary from true variations in interfacial fluid properties.

The effect of the viscous boundary will influence the resolution of this technique. As the probe approaches the boundary, there will be an increased dissipative effect. As with any instrumentation, measuring small signals in a large background is problematic. In Chapter 6, the limitations of this technique will be discussed and the boundary effects will be discussed.

4 Experimental Setup and Testing Procedures

This chapter will discuss the hardware and procedural aspects associated with this research. Additional aspects of the AFM and how it was integrated with a separate Data Acquisition (DAQ) system to acquire the data will be discussed. The testing procedures and post-processing will then be discussed to illustrate how the data was used to obtain the resulting fluid properties. The results will be discussed in detail in the chapter 5.

4.1 Experimental Testing Configuration

4.1.1 AFM and DAQ Integration

Figure 4-1 illustrates the how the AFM hardware was integrated with a separate DAQ system. A Signal Break-Out Box (SBOB), which gives the user complete access to control and data signals, was placed in line between the Nanoscope controller and the microscope. With simple toggle switches, the user could either monitor data and control signals or had the ability to interject their own signals to both the controller and microscope. This completely opened the functionality of the AFM for any experimental needs. As will be discussed in the data acquisition section, a stand alone DAQ system was used in conjunction with the SBOB to meet our experimental needs.

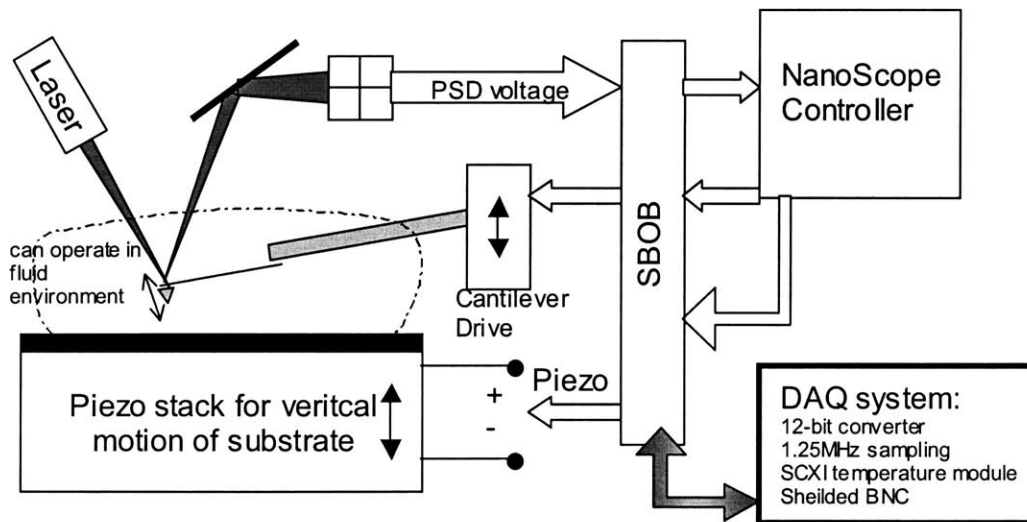


Figure 4-1: Integration of AFM and separate data acquisition system

4.1.2 Cantilevers: triangular and rectangular w/ and w/o tips

Although the theory, in the Chapter 3, related to rectangular beams, there are many different types of cantilevers available for various SPM techniques. As shown in Figure 2-14, there are several triangular shaped beams, which are used for applications ranging from fluid tapping to DNA and polymer pulling experiments. There are also very stiff, high resonant frequency, beams used for tapping mode experiments in air.

To align with the analytical models, model # CLFC-NOBO, force calibration cantilevers from Veeco Metrology were first chosen for testing. These were uncoated single crystal silicon rectangular cantilevers without tips. The driving reason for this decision is illustrated in Figure 4-2.

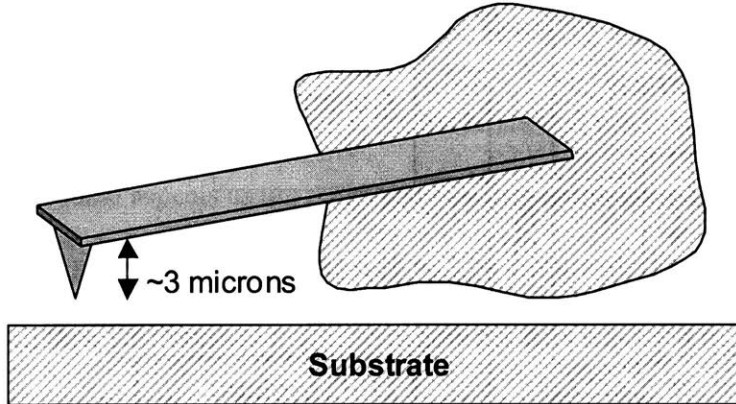


Figure 4-2: Tipped cantilevers limit the minimum separation between a cantilevered beam and substrate.

Using a tipped cantilever, the minimum distance to the substrate that the thermal oscillations could be acquired was the height of the tip. Considering most tips were on the order of $3\ \mu\text{m}$, the influence of the fluid medium was still clearly in the bulk regime. However, the tipless force calibration cantilevers were not intended for imaging, and were therefore not coated or optimized for a good signal to noise ratio. Therefore several attempts were made to improve the signal of the reflected laser beam off the backside of the cantilever by applying low-pressure vapor deposited Silver coatings. Although there was a noted improvement in the signal levels, it was not consistent, the signal to noise ratio levels were still below the Veeco Au coated beams. Combined with the fact that the focus of this work was bulk validation of visco-elastic measurements, model # MLCT-AUNM rectangular beams with tips were chosen for testing, see

Table 4-1.

Cantilever Type	B-rectangular
Cantilever Length	$200\ \mu\text{m}$
Cantilever Width	$20\ \mu\text{m}$
Cantilever Thickness	$0.6\ \mu\text{m}$
Tip Height	$3.0\ \mu\text{m}$
Spring Constant	$0.02\ \text{N/m}$
Resonant Frequency	$15\ \text{KHz}$

Table 4-1: Typical cantilever parameters

The mass of the tip was significantly smaller than that of the beam and had no observable effect on the beam dynamics, which will be evident when the results are discussed. Assuming the tip is pyramidal, $V_{tip} = \frac{1}{3} A_{base} H$, where H is the height of the tip. The resulting mass ratio was negligible, $\frac{m_{tip}}{m_{beam}} = 0.007$.

4.2 Data Acquisition

4.2.1 Testing

In order to acquire the necessary data, with the AFM in advanced force mode, a separate DAQ system was required because the sampling rate and AFM onboard DAQ options were not sufficient. Specifically, the AFM was configured to acquire data when the probe was either approaching or retracting from the substrate. Figure 4-3 shows a conceptual experimental test.

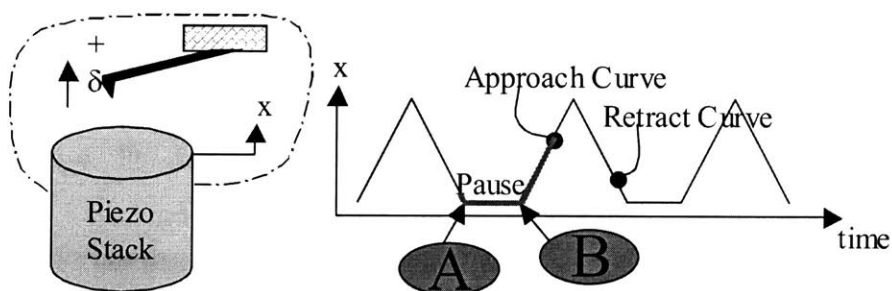


Figure 4-3: A conceptual experiment in which data would be acquired during the pause in the retracted position, and the approach curve would give the precise location at which the thermal was captured

The piezo stack was driven up toward the probe until contact was made with the probe and then retracted. The piezo stack was then paused in this retracted position, and the thermal fluctuations of the cantilevered probe were acquired between labels “A” and “B”. Immediately

following the pause, a subsequent force curve was generated, in which the piezo was again driven up until contact was made with the substrate and then retracted. The distance from the surface at which the thermals were acquired was then computed to within $\pm 1\text{ nm}$. This testing procedure also eliminated any issues related to drift in the piezo stack. This type of precision testing is precisely why the AFM platform was so well suited for the needs of interfacial research. However, as already stated, a separate DAQ system was required to capture the photodiode signal in the retracted position, and was triggered off the z-piezo position. Samples of the recorded data, highlighted between “A” and “B”, will be discussed later in this chapter.

4.2.2 Data Acquisition Hardware

The DAQ card used was a National Instruments PCI series 6071E card. This was a 12-bit programmable card with 64 AI, 2 AO, and 1.25MHz sampling, which was used with a BNC box to shield all signals. An attached SCXI chassis with a TC 2095 temperature module, capable of 32 separate temperature measurements, was used to measure the environment temperature. All of the DAQ hardware was controlled with a LabVIEW interface.

4.3 Testing Procedure and Post-Processing

The following two sections will discuss the experimental testing procedures and step through the post-processing steps required to extract the viscosity and relaxation time, η_0 and λ , at a known height, h . Figure 4-4 illustrates this data flow graphically.

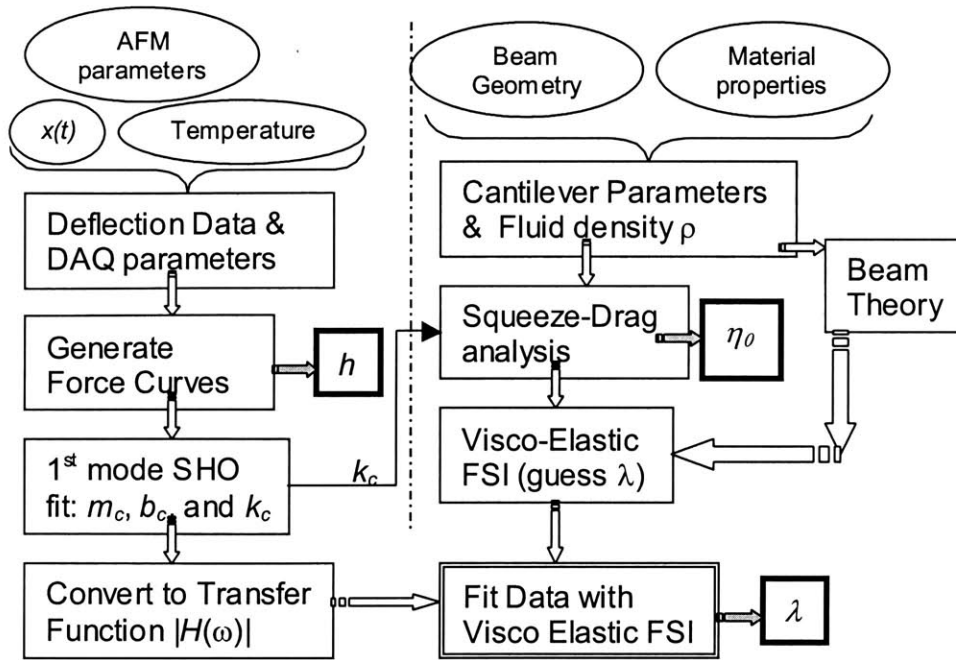


Figure 4-4: Testing parameter input and post-processing flow chart to yield visco-elastic fluid properties: η_0 and λ , at a know height above the substrate, h .

The first section will discuss the critical steps during the data acquisition procedure and explain why they were required for post-processing. The following section will discuss how the deflection data, DAQ parameters, and user input data were used in the post-processing program, Figure 4-4. The details associated with each step will be discussed.

4.3.1 Experimental Testing Procedure

Figure 4-5 is an excerpt from a larger experimental testing procedure, which was developed through trial and error, but captures critical steps required for accurate results in the post-processing stage.

- | |
|---|
| <ul style="list-style-type: none"> □ Bulk air thermal (yield cantilever m, b, k constants) <ul style="list-style-type: none"> ○ Contact surface and compute OLS [nm/V] ○ Delay $\cong 110\text{ms}$ (prefer 220ms) for adequate number of points ○ Speed/pull such that can identify end of thermal and start of approach ○ Check parameters on DAQ (OLS, delay, speed, etc) ○ Raise Stepper Motor to approx. 60micron for thermal ○ Zero Photo-Receiver about thermal ○ Adjust Analog-to-Digital range on DAQ ○ Save at least two sets of Data □ Fill system with fluid and re-align laser on cantilever □ Bulk fluid thermal |
|---|

Figure 4-5: Portion of testing procedure checklist, which illustrates critical aspects of the experimental testing

In general, there were three parts to every test. The first part consisted of quantifying the cantilever parameters. As noted in previous chapters, it is necessary to know the m_C , b_C and k_C of the cantilever, such that when immersed in fluid, any changes in the spectral response can be related to m_{fluid} and b_{fluid} of the fluid. Therefore, the testing portion labeled “bulk air thermal” is the calibration procedure required any time a new cantilever was used. The second part was the re-alignment of the AFM laser system. Since the refractive index of the fluid is different than that of air, it was essential to re-align the optical system since the optical path was now different. Finally, the third part was essentially another calibration in the bulk of the fluid, as in the air.

Before discussing any data, a brief explanation of the steps under the “bulk air thermal” will be given since they were essential for successful results. The first step involved computing the OLS, optical lever sensitivity, of the probe. This was a conversion factor from the measured voltage output of the photo-diode to a nm displacement. To compute this, the cantilever was brought into hard contact with the piezo-controlled substrate, such that any displacement, change in photo-diode voltage, was exactly the displacement of the piezo stack, which was known.

The next step was to ensure adequate time of sampling in the retracted paused position, such that after Fourier transforming and averaging the spectrums, there were sufficient data at

both high and low frequencies. Furthermore, the beginning and end of the thermal oscillations needed to be identifiable such that portions of the spectrum did not include any noise induced by piezo motion.

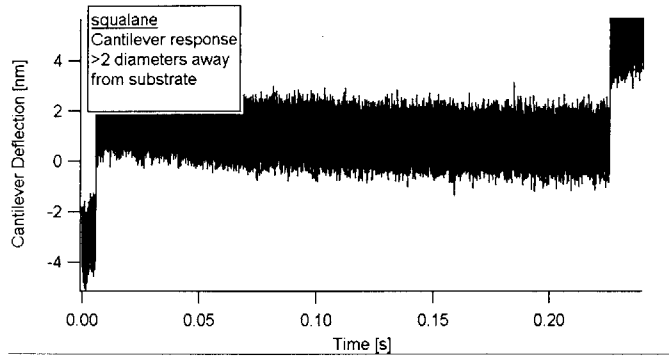


Figure 4-6: Time response of probe in Squalane. The motion of the piezo clearly affects the deflection data and needed to be identified to avoid inclusion in the spectra.

The next step was to ensure that all user input variables in the LabVIEW interface were entered correctly. The cantilever was then raised with a stepper motor to eliminate any substrate influence, and the photo-diode and programmable DAQ gains were set to maximize resolution and minimize any quantization noise[40] in the final result. The power spectrum of the quantization noise has a value given by equation (4.1).

$$S_{quant} = \frac{(\Delta V_{min})^2}{12 f_{nyquist}} = \frac{\left(\frac{0.1V}{2^{12}}\right)^2}{12 \frac{1.25e6Hz}{2}} \approx 10^{-16} \frac{V^2}{Hz} \quad (4.1)$$

4.3.1.1 Typical Data Set

The thermal oscillations in the bulk of the fluid were the focus of the results, as they served to validate this new visco-elastic fluid structure interaction theory and were compared with other bulk techniques. However, keeping with the theme of using this as an interfacial probe, the next procedural step was to lower the probe such that there was hard contact with the substrate as the

piezo extended upward, recall Figure 4-3. A typical resulting cantilever deflection is shown in Figure 4-7.

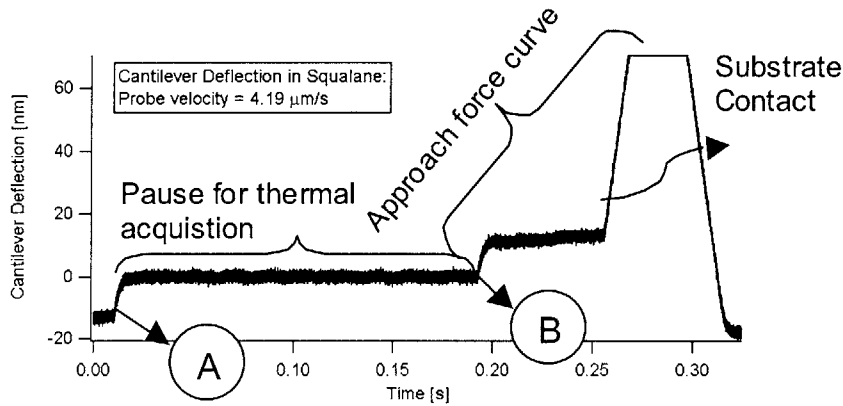


Figure 4-7: This is un-processed cantilever deflection corresponding to piezo motion illustrated in Figure 4-3. The relaxation of the cantilever at "A" and the linear deflection region at hard contact with the substrate is apparent.

Figure 4-7 is typical of all data sets taken. The beginning and end of the thermal was identifiable. The linear deflection region indicated hard contact with the substrate, and was subsequently used in the post-processing to determine the thermal height, which will be discussed. It is also instructive to think of the cantilever deflection, or force versus the piezo position, Figure 4-8.

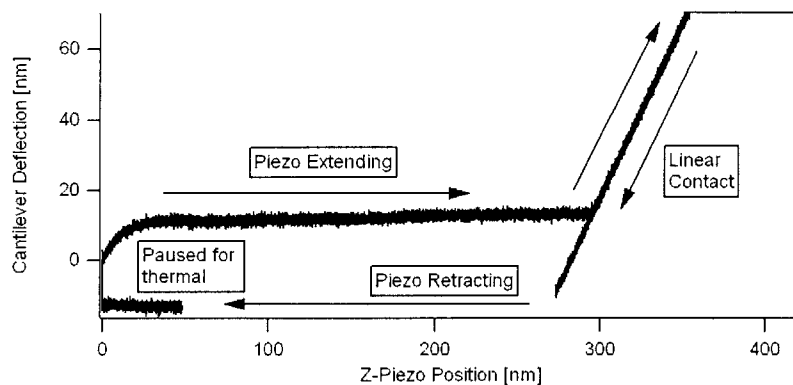


Figure 4-8: Cantilever deflection, or force, versus substrate position as the piezo is extended and retracted.

The hysteresis loop was due to viscous dissipation as the probe was dragged through the fluid.

The magnitude of this separation between the extending and retracting paths, Figure 4-8, will be discussed in the post-processing when the squeeze-film drag analysis is discussed.

4.3.2 Post-processing

IGOR was the program of choice for handling and processing the data for several reasons, primarily because of its ability to handle large data sets, 10^6 data points, and smoothly generate plots without taxing the computers. Additionally, IGOR is tailored for fitting functions to a variety of data sets. The large data sets were a consequence of sampling at 1.25MHz , such that the higher modes were captured, while sampling for 300ms , such that the lower frequencies were captured as well.

Data and parameters were imported into a workspace and all of the post-processing was menu driven by macros and user-defined functions, which guided the user from step to step, giving instructions on how to proceed depending on each situation. All macros and functions required were loaded via a single procedure file with the necessary command lines, see Appendix A.

4.3.2.1 Processing of Experimental Data

Deflection data and DAQ parameters were loaded from LabVIEW exported text files. The user was then required to identify points in the waves, which were entered into a pop-up window, that defined the thermal wave, approach wave and retract wave.

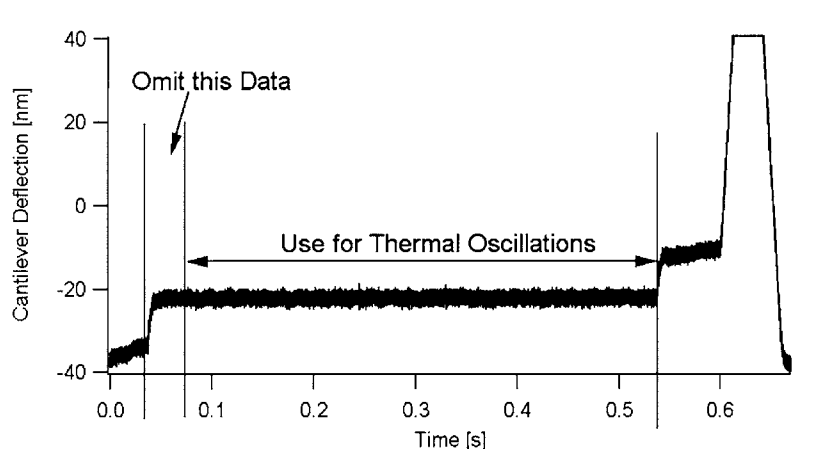


Figure 4-9: When defining thermal wave, one must omit portions where the cantilever is relaxing in order to minimize spectral errors.

The user must take care to eliminate the relaxation portion, Figure 4-9, of the thermal wave or the Fourier transform will have an erroneous low frequency component.

4.3.2.1.1 Generate Force Curves

Force curves were used to determine the height above the substrate. The first step was to verify that the optical lever sensitivity was correct by plotting deflection verses piezo position, Figure 4-10.

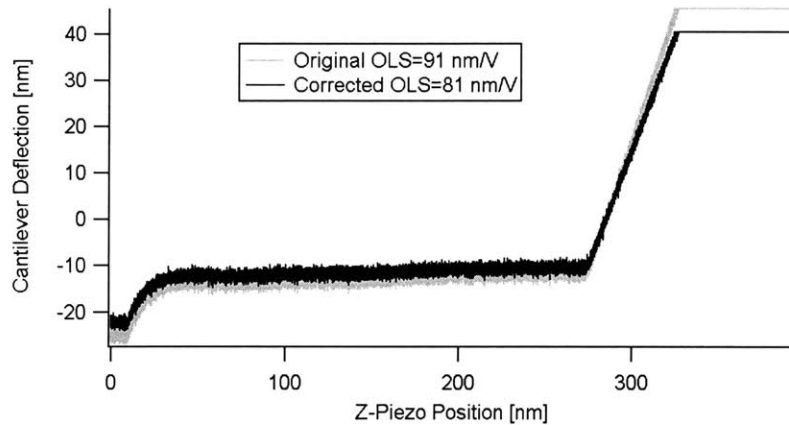


Figure 4-10: One must plot the cantilever deflection versus the piezo position such the optical lever sensitivity, [nm/V], can be recalculated to ensure correct conversion from photo-diode voltage signal to nm deflection

By the method in which the sensitivity was determined, the linear region should have a slope of one, but because of slight changes through testing, such as laser position of the photo-diode, the OLS is slightly incorrect. Therefore, the correct OLS is given by equation (4.2).

$$OLS_{new} = \frac{OLS_{old}}{slope_{linear}} \quad (4.2)$$

This correction was critically important, because although it can be seen in Figure 4-10 that the slope was virtually the same, the optical lever sensitivity value determined the deflection values. Any errors would propagate throughout the entire post-processing. The final step was to plot deflection versus cantilever-substrate separation, $Z_{separation} = Z_{piezo} - Z_{deflection}$. Shifting this plot to the correct zero values, one can easily determine the thermal height, $h=250nm$ for Figure 4-11.

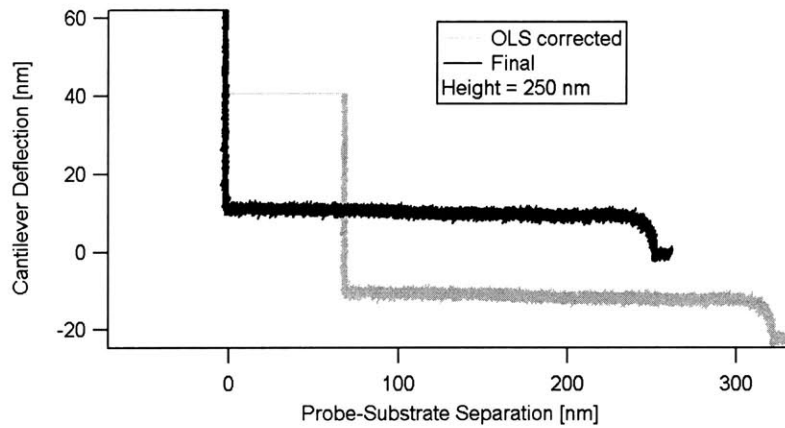


Figure 4-11: The cantilever deflection, y-axis, and separation, x-axis, need to be zeroed such that the height at which the thermal was obtained can be determined. This force curves was obtained in squalane Figure 4-7.

4.3.2.1.2 Generate Power Spectral Density

To capitalize on the computational efficiency for computing FFTs, equation (4.3), the data needed to be broken into 2^n data length segments.

$$S_{out} = |X|^2 \quad (4.3)$$

It was necessary to check that the user did not enter a segment length larger than the data set itself. Although the program would still give a result, it was an incorrect result. The program was written such that the data was windowed prior to computing the FT. The Hanning window, set as the default, was used to match end points and minimize noisy FT results by eliminating sudden jumps at data ends, since FFT routines expect infinitely repeating units. The discrete FT components of $x(t)$ were given by equation (4.4).

$$X_k = \frac{2}{n} \sum_{m=0}^{n-1} e^{-j(2\pi k)\frac{j}{m}} \quad (4.4)$$

To view the FT components as a function of frequency, the f_k 's needed to be scaled according to equation (4.5).

$$f_k = k \left(\frac{f_{\text{sampling}}}{n} \right) \quad (4.5)$$

The Fourier transformed segments, usually two or three, were averaged to smooth the results. An example of the resulting spectrum will be shown in the next section, when the SHO fit is discussed.

4.3.2.1.3 SHO fit to First Mode

The next few steps prompted the user to enter values required for performing the SHO fit. First, the user was asked to enter the frequency, f_{lower} , where the $1/f$ noise began to dominate the system. On a log-log plot, this noise has a slope of (-1), as seen in Figure 4-12.

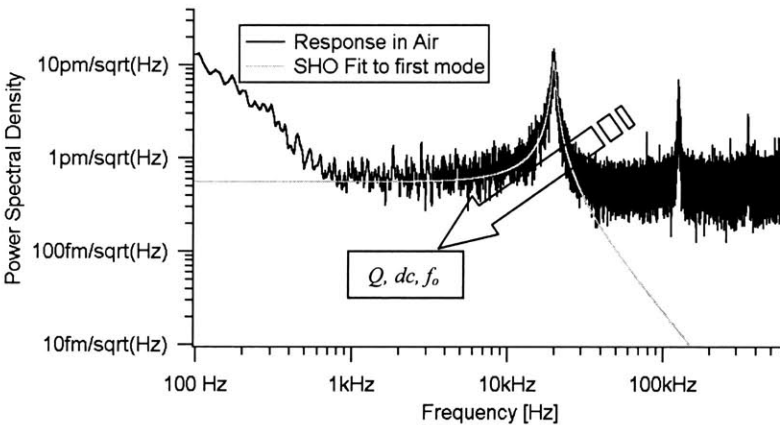


Figure 4-12: A SHO model is fit to the first mode of the power spectral density to determine the m_c , b_c and k_c of the cantilever.

The next step was to enter a bandwidth, usually 500Hz, to filter spikes in the spectrum resulting from monitors and other electronic equipment. Next, a sliding box filter was applied and a crawler routine searched the spectrum for the first mode. Once the program located the first mode, the user was asked for a width about f_0 from which to fit the SHO model. The final result is shown in Figure 4-12.

Note the units of the y-axis are $\left[\frac{m}{\sqrt{Hz}} \right]$ or $\sqrt{S_{out}}$, such that when the SHO fit returns

values for f_0 , dc_{fit} and Q , the units on dc_{fit} need to be changed to compute the equivalent m_C , b_C and k_C . Recall from the theory chapter that at dc $|H(j\omega)| = 1/k_C$. Therefore, since we already

have

$$S_{out} = |H|^2 S_{in} \quad (4.6)$$

and we know S_{in} such that

$$S_{out} = \left(\frac{1}{k_C} \right)^2 4k_B T b \quad (4.7)$$

then substituting for

$$b_C = \frac{k_C}{(2\pi f_0) Q} \quad (4.8)$$

the result can be rearranged to yield k_C , equation (4.9).

$$k_C = \frac{4k_B T}{(2\pi) f_0 Q (S_{out}|_{f=0})} \quad (4.9)$$

Now that k_C , f_0 , Q and b_C are known in terms of parameters from the SHO fit, m_C is the only remaining unknown, equation (4.10).

$$m_C = \frac{k_C}{(2\pi f_0)^2} \quad (4.10)$$

4.3.2.1.4 Convert PSD to Magnitude of Transfer Function

All the information is now available to convert the measure S_{out} , with units of m^2/Hz , to an equivalent transfer function by rearranging equation (4.6).

$$|H| = \sqrt{\frac{S_{out}}{S_{in}}} \quad (4.11)$$

such that

$$|H(f)| = \sqrt{\frac{S_{out}(f)}{4k_b T b}} = \sqrt{\frac{S_{out}(f)}{4k_b T \left(\frac{k_c}{(2\pi f_0) Q} \right)}} \quad (4.12)$$

Figure 4-13 shows the result of this conversion. As noted, the dc value is equal to the reciprocal of k_c .

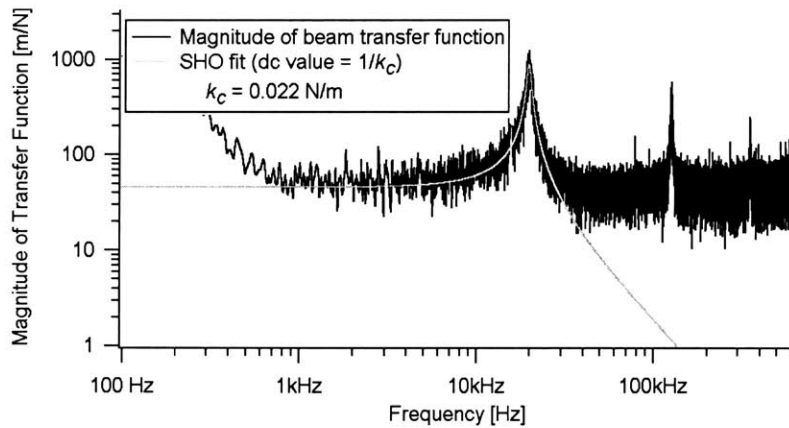


Figure 4-13: The power spectral density can be converted to the effective magnitude of a SHO transfer function.

4.3.2.2 Processing of Theory

4.3.2.2.1 Beam theory and visco-elastic FSI

At this point the experimental data had been converted to a transfer function magnitude, $\left| \frac{X}{F} \right|$, which could be compared to equation (3.44) and Figure 3-7. It was now time to consider the influence of the fluid environment on the spectral response of the probe. Recall equation (3.74).

$$\left| \frac{X}{F} \right|^2 = \sum_n \frac{1}{(k_n - (m_n + m_{add})\omega^2)^2 + ((b_n + b_{add})\omega)^2} \quad (4.13)$$

With the user-entered parameters, on the right hand side of Figure 4-4, the beam theory (m, b, k) and subsequent FSI (m_{add}, b_{add}) could be computed. To compute the beam response, it will be assumed for now that η_0 is known, but a micro-viscometer method is discussed in the following section, where η_0 is computed from the relaxation process that was omitted in Figure 4-9.

Using equation (4.13) and assuming a Maxwell model, as discussed in the theory chapter, a theoretical response of the beam can be computed. The analytical solutions for m_C, b_C and k_C have been derived and the new theory for visco-elastic FSI was solved to yield $m_{add}(2\pi f)$ and $b_{add}(2\pi f)$.

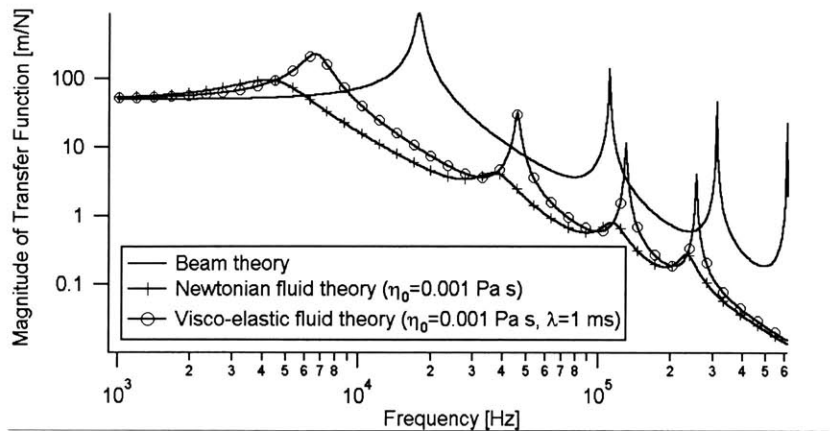


Figure 4-14: Theoretical comparison of beam theory, Newtonian FSI theory and visco-elastic FSI theory. The resulting spectral response of the beam is shown in Figure 4-14 for both an aqueous type Newtonian fluid and visco-elastic fluid with the same viscosity and $\lambda=1\text{ ms}$. In agreement with what was discussed in chapter 3, elasticity has the effect of reducing m_{add} and enhancing the quality of the modes at higher frequencies, since they are probing the fluid in its elastic regime. These plots will be compared to experimental data at the end of this chapter.

4.3.2.2 Squeeze Film Analysis

This section will discuss how η_0 was computed. A schematic of the required system variables is shown in Figure 4-15.

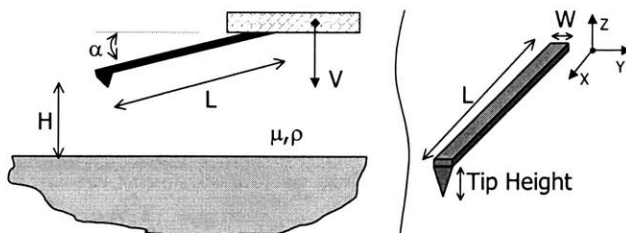


Figure 4-15: Schematic of cantilever and relevant system variables

The following sections will outline the theory associated with the squeeze-film and drag forces acting on the cantilever and compare the models with measured data.

4.3.2.2.1 Drag on a Cylinder

To approximate the drag force on the rectangular cantilever, the drag for an equivalent cylinder[41] was used, where the diameter in equation (4.14) was equal to the width of the beam. Many researchers have modeled AFM cantilevers as spherical and cylindrical bodies and results have shown this is an appropriate estimate for many applications of SPM cantilevers[38, 42]

$$C_D = \frac{8\pi}{\text{Re}_D \text{Log}\left(\frac{7.4}{\text{Re}_D}\right)} \quad (4.14)$$

Re_D represents the Reynolds number for the equivalent cylinder, $\text{Re}_D = \rho DV / \mu$, and the resulting force acting on the cantilevered beam is given by

$$F_d = C_d \frac{1}{2} \rho V^2 (DL) \quad (4.15)$$

For results shown in this thesis, the values of Re_D range from 6.0e-6 to 6.0e-3.

Bulk Drag on SPM cantilevers is justifiably neglected in many applications that involve fluids with viscosities on the order of water. However, when applications with more viscous fluids are required, such as lubricants and oils, or fast velocities as seen in Figure 4-16, the bulk drag must be considered.

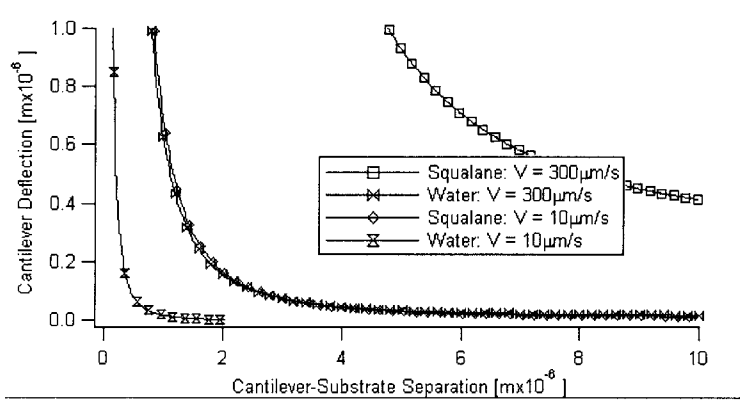


Figure 4-16: Full range of theoretical deflection curves discussed in this paper. All curves have similar shape but are shifted according to fluid properties and testing dynamics.

As will be shown, drag effects dominate the response of the cantilever under certain experimental conditions.

4.3.2.2.2 Squeeze-Film Theory

Once the cantilever nears the surface, relative to its width, squeeze-film effects between the cantilever and substrate dominate the force response of the cantilever. To explain the impact of the squeeze films in our experiments, we will begin by outlining an idealized solution and then show added corrections for a more practical model of the SPM cantilevers.

Recalling Figure 4-15, if one first considers a beam parallel to the substrate, $\alpha=0$, with an aspect ratio, $\varepsilon = W/L \ll 1$, and a normalized gap, $S = H/W \ll 1$, then the governing equation for the fluid simplifies to the well know Stokes flow equation in a thin gap, for the incompressible and viscous dominated limit.

$$0 = -\frac{dP}{dy} + \mu \frac{d^2v}{dz^2} \tag{4.16}$$

If one allows the gap to be reduced at a constant speed, V , then the resulting Force on the parallel beam is

$$F_s = \mu VL \left(\frac{1}{S} \right)^3 \quad (4.17)$$

Although this force is felt over the entire cantilever, it cannot be used with the commonly used spring constant for an end loaded cantilevered beam[37] to compute displacement.

$$k_c = 3 \frac{EI}{L^3} \quad (4.18)$$

To compute the correction for k_c , we need to consider a distributed loaded beam. Neglecting the inertial response of the beam, the deflection, w , of a distributed loaded cantilever is governed by

$$\frac{d^2 w(x)}{dx^2} = \frac{3M(x)}{k_c L^3} \quad (4.19)$$

where

$$M(x) = \int_0^w \int_x^L P(x', y') \cdot (x' - x) dx' dy' \quad (4.20)$$

Solving the governing equations with the appropriate boundary conditions for a cantilevered beam, the resulting deflection measured at the end of the cantilever is given by

$$w(L) = \frac{3}{8} \frac{\mu VL}{k_c} \left(\frac{1}{S} \right)^3 \quad (4.21)$$

Since the cantilevers used in our experiments, can have large variations from their published nominal values, k_c was experimentally determined by fitting the lowest mode of the cantilever to a SHO model[42, 43], which will be discussed in the post-processing section.

Although the above analysis provides an estimate for the squeeze-film forces on SPM cantilevers, there are some notable differences in the practical configuration that need to be considered. The probes are cantilevered beams with finite aspect ratios, mounted on angles, relative to the substrate, and are usually separated from the substrate such that 2-D effects must

be considered. Recent work by Vinogradova[44] suggests a first order analytical correction for these practical operating conditions.

$$w(L) = \frac{3}{8} \frac{\mu VL}{k_c} \left(\frac{1}{S} \right)^3 (\beta_1 \beta_2) \quad (4.22)$$

These multiplying correction factors can be directly applied to the idealized squeeze-film results, where

$$\beta_2 = \left[1 - \left(\frac{2}{\pi} \right)^7 \varepsilon \sum_j \frac{-3\varepsilon\pi j + 2[3\varepsilon^2 + (\pi j)^2] \tanh\left(\frac{\pi j}{2\varepsilon}\right)}{j^7} \right]; \varepsilon = \frac{W}{L} \quad (4.23)$$

corrects for the 2-D effects, resulting from a finite aspect ratio, and

$$\beta_1 = \left[\frac{4\gamma}{3} \left(1 - \frac{3\gamma}{2} + 3\gamma^2 - 3\gamma^3 \ln\left(1 + \frac{1}{\gamma}\right) \right) \right]; \gamma = \frac{H}{\alpha L} \quad (4.24)$$

corrects for the inclination of the cantilever. β_2 , which depends solely on cantilever geometry, was $\beta_2=0.92$ for the cantilevers used in our experiments. It is worth noting that these correction factors possess the correct asymptotic behavior such that the squeeze film results are recovered in the limit of infinitely small aspect ratio and $\alpha=0$.

In order to quantify the measured response of the SPM cantilevers, the total force acting on the cantilevers was modeled as the superposition of the drag and squeeze-film force.

$$F_{net} = F_d + F_s = \frac{8\pi}{\text{Log}\left(\frac{7.4}{\text{Re}_D}\right)} \frac{1}{2} V \mu(L) + \frac{3}{8} \mu VL \left(\frac{1}{S} \right)^3 (\beta_1 \beta_2) \quad (4.25)$$

or

$$\bar{F} = \frac{3}{8} \left(\frac{1}{S} \right)^3 (\beta_1 \beta_2) + \frac{4\pi}{\text{Log} \left(\frac{7.4}{\text{Re}_D} \right)} \quad (4.26)$$

where

$$\bar{F} = \frac{F_s + F_d}{\mu VL} \quad (4.27)$$

As shown in Figure 4-17, all of the normalized force curves should collapse into a single curve, with only the additive drag force distinguishing the plots at larger distance from the substrate.

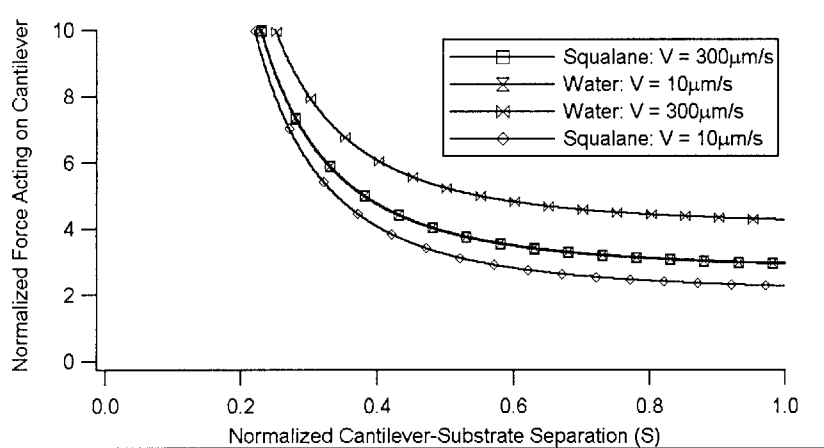


Figure 4-17: Theoretical dimensionless force curves. All force curves collapse in the squeeze-film regime, but are offset at father distances from the substrate by drag effects

To provide a baseline for comparison, results for various approach velocities in distilled water are first presented. Results for all fluids were fit to the squeeze-drag superposition model. As seen in Figure 4-18, the cantilever deflection, for the lower cantilever speeds, is well characterized by the model and is dominated by squeeze-film effects as the cantilever approaches the substrate.

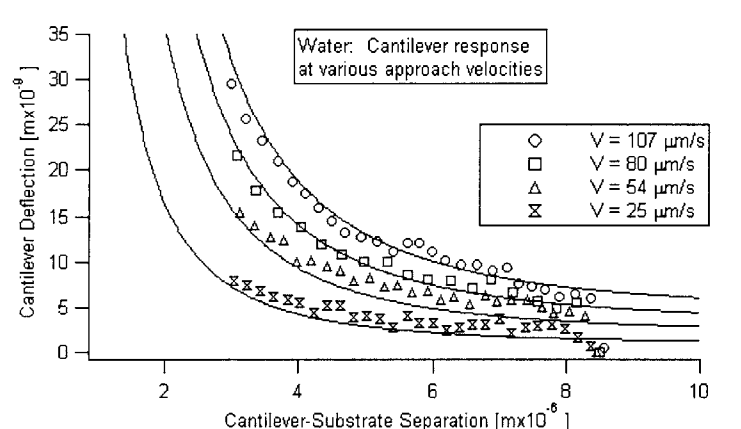


Figure 4-18: Cantilever response in water with approach velocity of 24.7 $\mu\text{m/s}$ to 107 $\mu\text{m/s}$

The drag effects in water and other aqueous solutions only account for 2nm to 5nm of the observed cantilever deflection. For this reason, bulk drag on cantilevers is often successfully neglected when SPM cantilevers are operated in aqueous or other low viscosity fluids. However, when faster cantilever speeds are required, the vertical shift in the models at larger separations becomes pronounced, which indicate increased bulk drag on the cantilevers. The rise time of the cantilever can even be observed for the faster cantilever speeds as the sudden increase in cantilever deflection at the start of each force curve.

Figure 4-18 shows that the superposition model of squeeze-film and drag forces adequately described the cantilever response in water for a large range of cantilever speeds.

Figure 4-19 illustrates the effect of fluid viscosity on cantilever deflection.

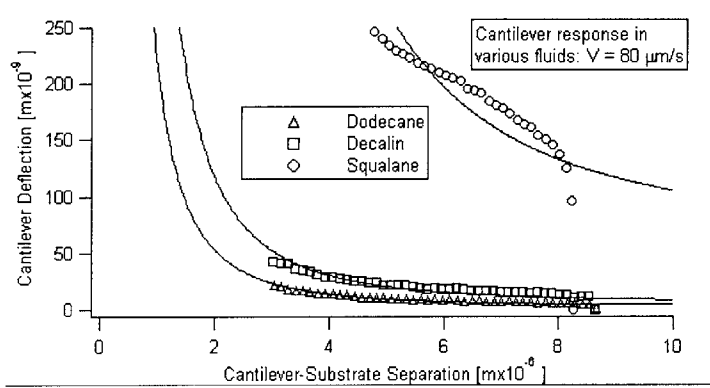


Figure 4-19: Effect of viscosity on force curves. All curves were measured at 80 $\mu\text{m/s}$

From the solid line fits in Figure 4-19, it is clear that as the viscosity is increased, the theory begins to breakdown for higher viscosity fluids. In addition to the tip affecting the force curves, there also appears to be cantilever dynamics in response to the step inputs of velocity. In dodecane, large oscillations were quickly damped out at the start of each approach curve and are not visible in Figure 4-19. However, in the more viscous fluids, these dynamics persist throughout the force curve due to increased viscous relaxation times, equation (4.29).

4.3.2.2.2.3 Micro-Viscometer

Through the course of our research, independent viscosity measurements for each test were required. Therefore, a method for quantifying the viscosity of each fluid was needed. To accomplish this we chose to fit the relaxation of the cantilever after the steady state piezo motion was stopped in the retracted position.

With the system at rest, this relaxation process consisted only of cantilever motion, whereas, the approach process involved both excited piezo and cantilever motion. The relaxation, Figure 4-20, was fit to an exponential function

$$\delta z = A \left(1 - \exp\left(\frac{-1}{\tau}\right) \right) \quad (4.28)$$

where the time constant,

$$\tau = \frac{b_{fluid}}{k_c} \quad (4.29)$$

gave a direct measure of the fluid dampening.

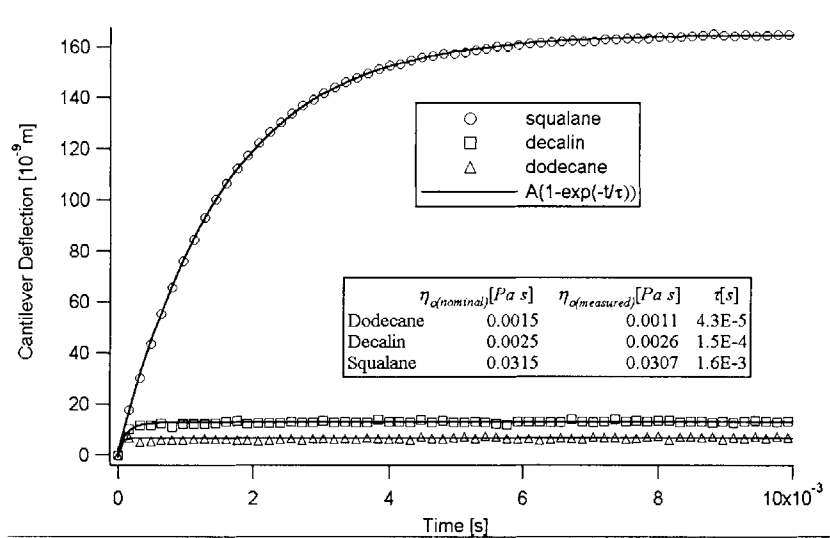


Figure 4-20: Cantilever relaxation from 80.2 $\mu\text{m/s}$ in dodecane, decalin, and squalane

To compute the fluid viscosity from this relaxation process, equation (4.25) was used in conjunction with $w(L)=(3/8)F_{net}$, to solve for the viscosity at the retracted height. When the relaxation was measured far from the substrate, $>2D_{cyl}$, the squeeze-film effect could be neglected. Since the drag is a transcendental equation with respect to μ , an explicit equation could not be written. Therefore, equation (4.30) was a useful correlation for thinking about the parametric influence on μ when the relaxation was measured far from the substrate.

$$\mu = \frac{w(L)k_c}{V_{cant}L} (0.4539) \quad (4.30)$$

The nominal published viscosities and the measured viscosities from this method are compared in Table 4-2.

Fluid Name	$\tau[s]$	$\rho_{nominal}[Kg/m^3]$	$\mu_{nominal}[Pa s]$	$\mu_{measured}[Pa s]$
Dodecane	4.3e-5	748.7	0.0015	.0011
Decalin	1.48e-4	870	0.0025	.0026
Squalane	1.55e-3	810	0.0315	.0307

Table 4-2: Results from micro-viscometer testing

From the measured values in the table it is clear that this technique functions as an accurate micro-viscometer for bulk fluid viscosity. At this point of the processing, an experimental technique has been demonstrated to quantify h and η_0 . The only remaining piece of the puzzle was to fit the theoretical plots in Figure 4-14 to experimental data and compute λ . The next section will show how λ was determined.

4.3.2.3 Fit visco-elastic FSI theory to experimentally measured data

To illustrate the final step of the post-processing, determination of λ , the response of the probe in a 0.10% by weight solution of Polyethylene Oxide (PEO), $M_w=2e6$, in water will be shown. Various solutions of PEO were chosen for testing since their viscosity and relaxation time could easily be varied with concentrations. All data shown from this point on will be restricted to measurements far from the substrate to eliminate any boundary effect.

As just outlined, the spectral response of the probe was first measured in air to give m_C , b_C and k_C . The spectral response was then quantified in the fluid environment. The data was processed to an equivalent transfer function, the k_C was passed to the squeeze-film analysis and the resulting value for η_0 was determined.

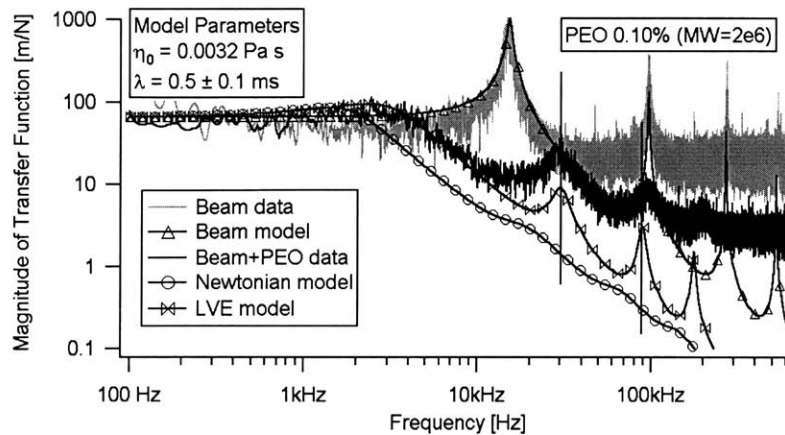


Figure 4-21: Fit visco-elastic theoretical response of modes to measured modal response. The Newtonian response is shown for comparison of the old FSI theory with the new VE-FSI theory.

The associated beam theory and visco-elastic FSI response was computed and the results were adjusted, via λ , to fit the experimental data, Figure 4-21.

Although the resolution and accuracy will be discussed in chapter 5, it is worth noting that this new technique gave $\eta_0=0.0032 \text{ Pa s}$ and $\lambda=500 \mu\text{s}$ for 0.1% PEO while other techniques gave $\eta_0=0.0032 \text{ Pa s}$ and $\lambda=4.9 \text{ ms}$. To validate this new method, other techniques were required to provide an independent measure of both η_0 and λ . To measure η_0 , an AR1000 Rheometer, by TA Instruments, was used for both steady-state flow and oscillatory experiments to measure η_0 , η' , and η'' . The relaxation time was a bit more difficult, since λ approached values as small as $100 \mu\text{s}$ and standard rheometers are not able to measure such short relaxation times. Therefore, a Capillary Breakup Extensional Rheometer (CaBER™), by Cambridge Polymer Group, was used[45]. Both the Rheometer and CaBER™ will be discussed in Chapter 5.

5 Results and Discussion

This chapter will present the actual data and analysis associated with determining the rheological parameters, η_0 and λ , via this new thermal technique. The first section will illustrate how the procedural techniques allowed one to measure the thermal spectrum at known heights with nm resolution. The second section will present the baseline data to which this thermal technique was compared. Specifically, η_0 and λ were determined by other bulk techniques available and these values served as a standard by which to judge the success of the thermal method. The remaining sections will present the data and the current limitations will be discussed in chapter 6.

5.1 Demonstrate thermal acquisition at known height with AFM platform

The AFM platform was chosen to determine thermal heights because of its spatial precision. To demonstrate this, thermal oscillations were acquired and their respective heights, h , were computed according to the procedure discussed in Chapter 4.

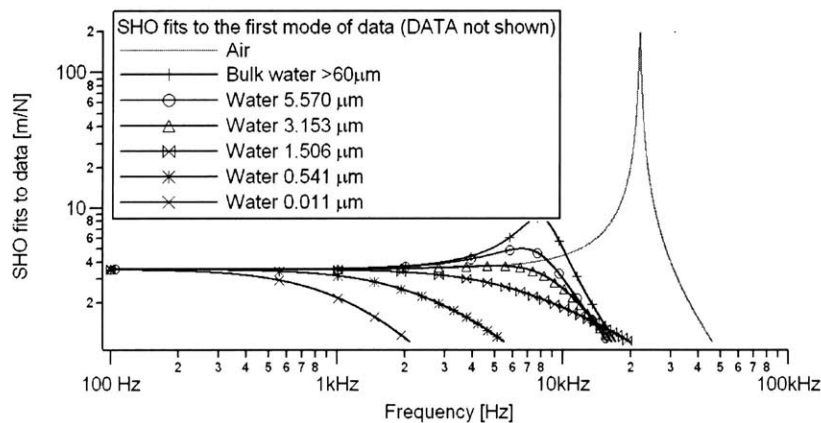


Figure 5-1: SHO fits to the first mode of cantilever response at varying heights in water, ranging from $>60\mu m$ to $11nm$

Figure 5-1 demonstrates the ability to distinguish variations in the spectral response of the SPM probe at heights ranging from bulk to *nm* scales. It should be noted that this is measuring increased dissipative effects due to the presence of the planar boundary. One may think it would become increasingly difficult to distinguish between heavily damped modes in the interface. However, it will be shown that when the lower modes of the cantilever become heavily damped by a visco-elastic fluid, the higher modes of the probe, which perturb the fluid on shorter time scales, become enhanced with an increase in the elastic response of a fluid. Ultimately, Figure 5-1 illustrates how this testing and processing procedure is capable of providing a measured thermal spectrum at a known height from the bulk regime to the interfacial regimes. The thermal spectra were fit with the SHO model from which effective properties can be extracted.

5.2 Baseline Techniques

5.2.1 Rheometer

The AR1000, by TA Instruments, was used to measure baseline values for η_0 . For all rheometer tests, a 6cm diameter 1° Acrylic cone and plate configuration was used for testing.

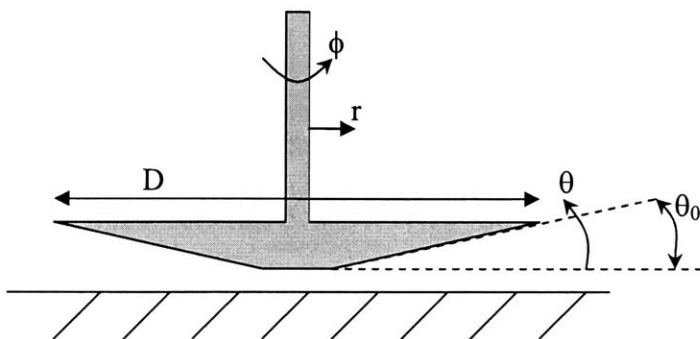


Figure 5-2: Schematic of cone and plate rheometer configuration

Figure 5-2 shows a schematic of a typical cone and plate rheometer test. To conduct steady state flow experiments, the cone is rotated at a steady angular velocity and the torque required to maintain this steady rotation is used to compute the viscosity. The Cone and plate configurations is a common set-up, particularly for steady-state flow experiments, since the strain rate, $\dot{\gamma}_{\phi\theta}$, throughout the gap is constant, equation (5.1).

$$\dot{\gamma}_{\phi\theta} \rightarrow \frac{1}{r} \frac{\partial V_{\phi}}{\partial \theta} \rightarrow \frac{\dot{\phi}}{\theta_0} \quad (5.1)$$

To compute the viscosity from the measured torque, the stress, $\tau_{\phi\theta} = \eta \dot{\gamma}_{\phi\theta}$, was integrated over the area of the cone, equation (5.2).

$$T = \int_0^R r \tau_{\phi\theta} (2\pi r dr) = -\frac{2}{3} \pi R^3 \left(\frac{\dot{\phi}}{\theta_0} \right) \eta \Rightarrow \eta \quad (5.2)$$

Re-arranging equation (5.2) gave a value for viscosity.

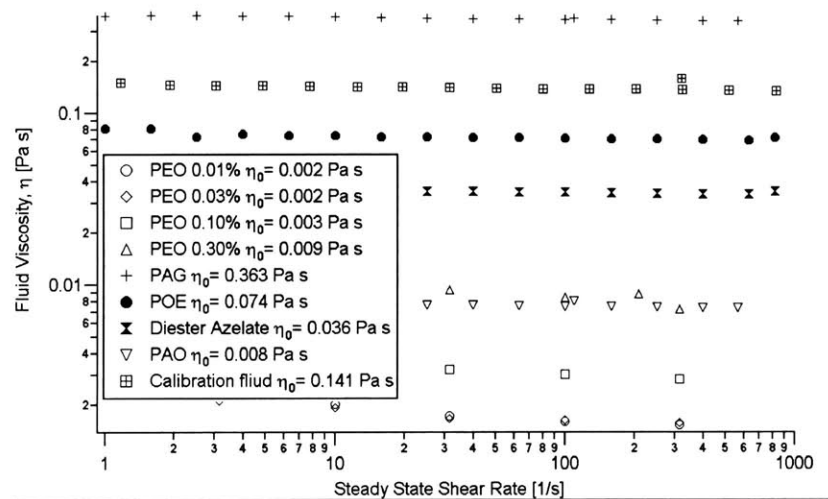


Figure 5-3: Viscosity versus steady-state shear rate data

Figure 5-3 shows the combined results of the steady-state flow experiments for several fluids discussed in this chapter.

In addition to the steady flow experiments, oscillatory tests were run, which quantified η_0 and λ as discussed in chapter 3 (SAOS).

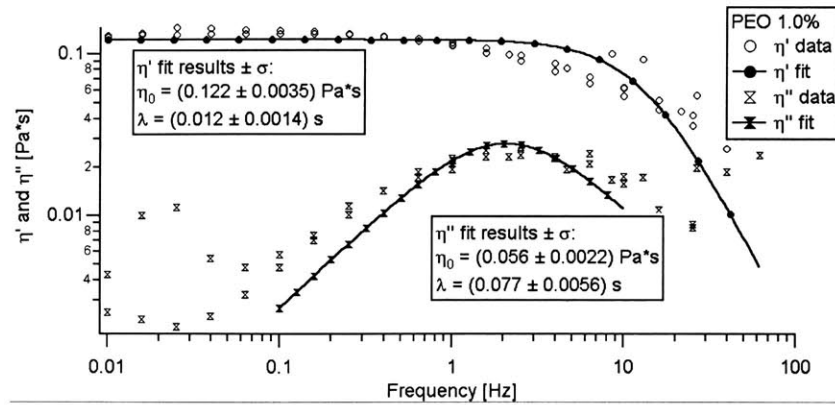


Figure 5-4: Oscillatory rheometer data for polyethylene oxide 1.0%

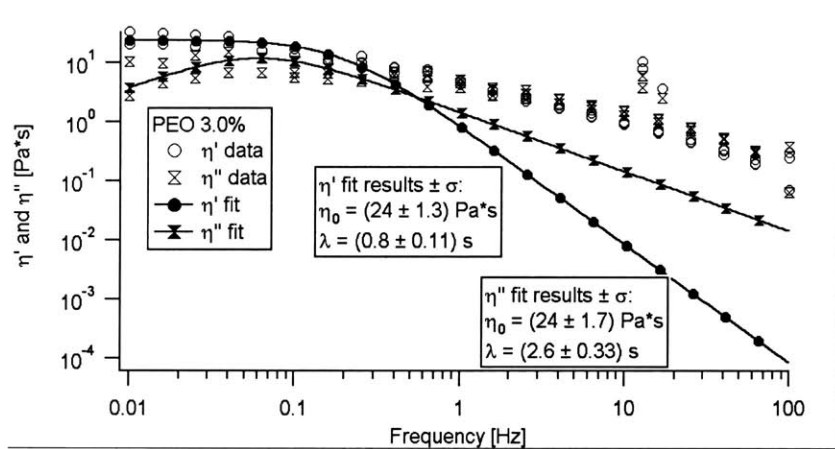


Figure 5-5: Oscillatory rheometer data for polyethylene oxide 3.0%

In Figure 5-4 and Figure 5-5, both η' and η'' were fit to the data, but the single mode Maxwell model failed to capture the fluid behavior at higher frequencies and there was significant disagreement between η_0 and λ values from the η' and η'' fits. Since the low frequency response of η' was not effected by the use of the single mode model, η_0 from the η' fit was used for the baseline viscosity values.

5.2.2 Caber

Since most of the fluids used had relaxation times $< 0.1s$ the CaBER™ testing was used to measure the relaxation times because this was beyond the rheometer capabilities.

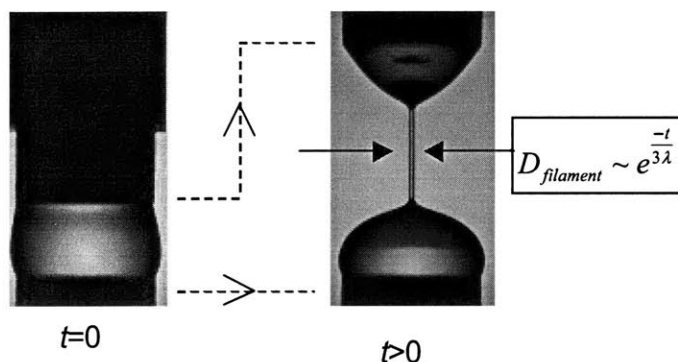


Figure 5-6: Schematic of how CaBER™ was used to determine fluid relaxation time, λ .

As shown in Figure 5-6, a step elongation was imparted to the fluid column and the time dependence of the filament diameter was related to the relaxation time of the fluid. This technique was capable of measuring relaxation times down to $\sim ms$. However, for highly dilute solutions with shorter time scales, $< 1ms$, Zimm theory was used for comparison, since experimental techniques were unavailable for these short relaxation times.

As noted, the time dependence of the fluid filament was given by equation (5.3).

$$D(t) \sim e^{-\frac{t}{3\lambda}} \quad (5.3)$$

On a semi-log plot, equation (5.3), becomes

$$\ln(D) = \text{const.} + \frac{-t}{3\lambda} \quad (5.4)$$

which is a straight line. However, for fluids with $\lambda < 1ms$ the filament was governed by viscous rather than elastic times scales, provided the viscosity was sufficient to sustain a filament. In

these cases the time dependence of the diameter was linear and the data would not fit a line on a semi-log plot.

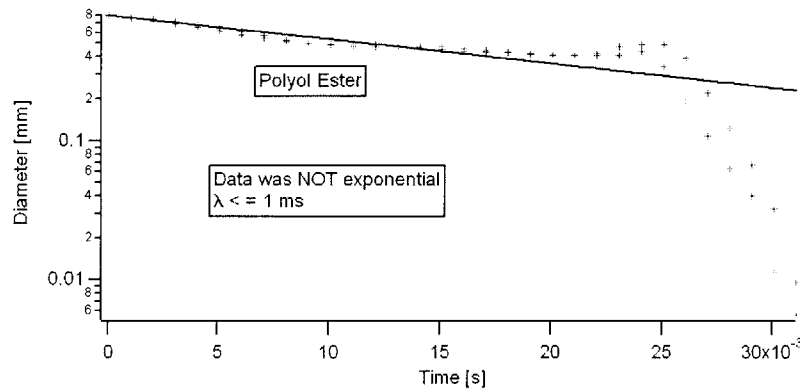


Figure 5-7: CaBER data and exponential fit for polyol ester

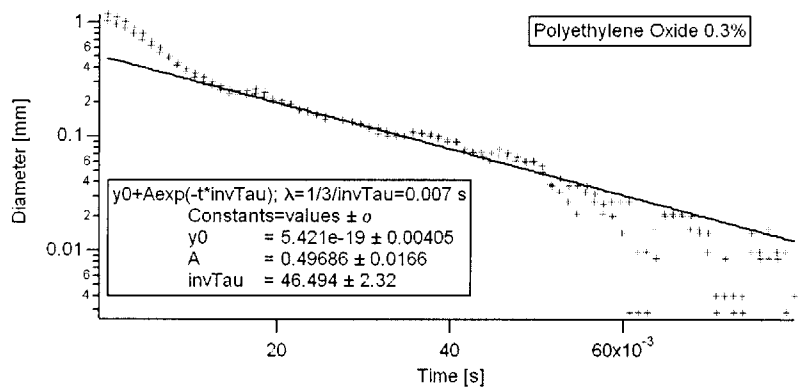


Figure 5-8: CaBER data and exponential fit for polyethylene oxide 0.3%

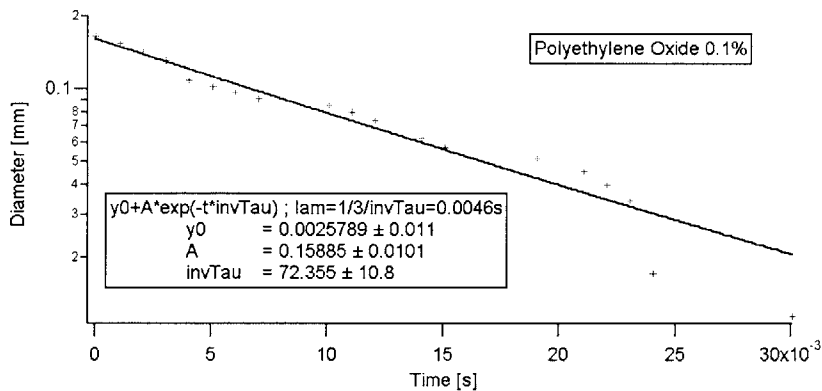


Figure 5-9: CaBER data and exponential fit for polyethylene oxide 0.1%

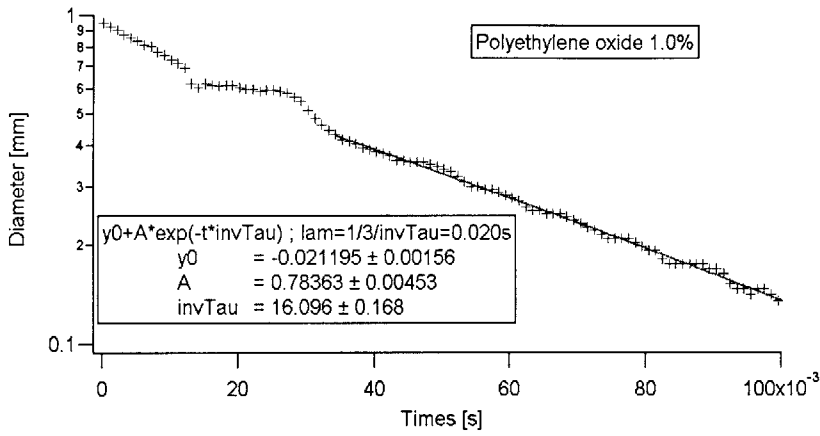


Figure 5-10: CaBER data and exponential fit for polyethylene oxide 1.0%

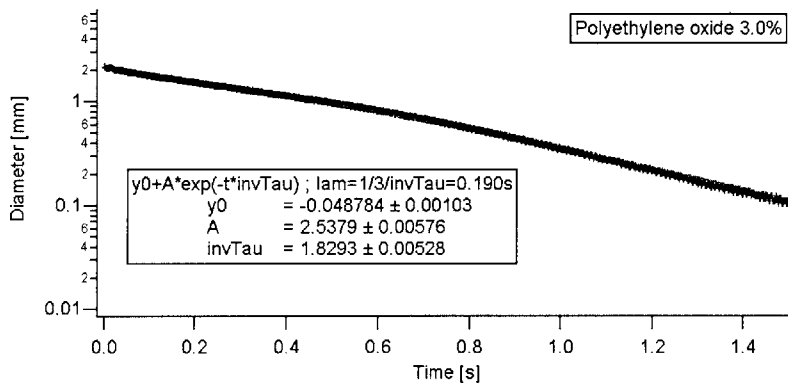


Figure 5-11: CaBER data and exponential fit for polyethylene oxide 3.0%

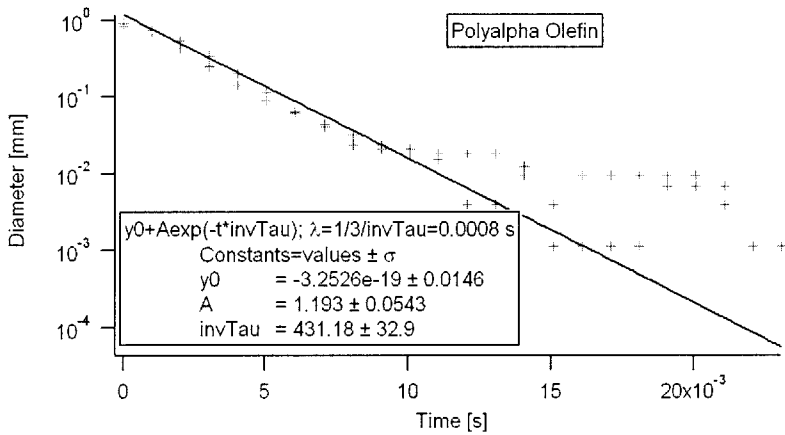


Figure 5-12: CaBER data and exponential fit for polyalpha olefin

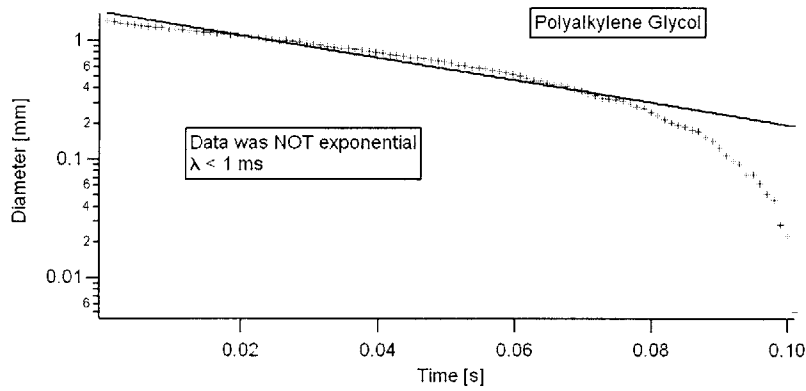


Figure 5-13: CaBER data and exponential fit for polyalkylene Glycol

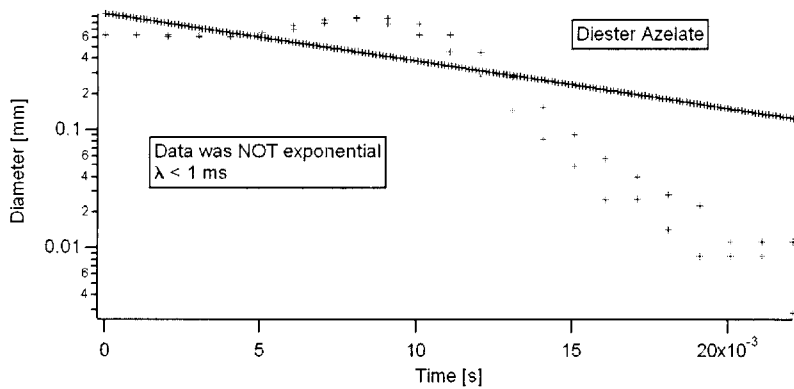


Figure 5-14: CaBER data and exponential fit for diester azelate

For Figure 5-7 through Figure 5-14, λ was determined for the data that obeyed equation (5.3). All but the POE, DEA and PAG data obeyed the exponential dependence such that λ was easily determined by fitting the diameter data. The best that could be said about PEO, DEA and PAG was that $\lambda < 1\text{ms}$. The results are summarized in Table 5-1.

Fluid	η_0 [rheometer]	λ [CaBER™]
Rheometer Calibration Fluid	0.141 Pa s	<1 ms
Water	0.001 Pa s	<1 ms
Diester Azelate	0.036 Pa s	<1 ms
PolyAlphaOlefin	0.008 Pa s	0.8 ms
PolyolEster	0.074 Pa s	<1 ms
PolyAlkyleneGlycol	0.363 Pa s	<1 ms
PolyEthyleneOxide (PEO) 0.01% wgt	0.002 Pa s	0.350 ms
PEO 0.03%	0.002 Pa s	0.350 ms
PEO 0.10%	0.003 Pa s	4 ms
PEO 0.30%	0.009 Pa s	7 ms
PEO 1.0%	0.122 Pa s	20 ms
PEO 3.0%	24 Pa s	190 ms

Table 5-1: Summary of η_0 and λ from baseline techniques used for comparison of the new thermally oscillating technique

The values in Table 5-1 summarize all the results from the baseline testing. Included in Table 5-1 are values for PEO 0.01% and 0.03%. In these dilute regimes, λ was independent of concentration, which will be confirmed with the results of the new thermal technique discussed in this chapter, and Zimm theory was used to approximate λ : $\lambda \approx (350 \mu s)$. Once the results are discussed from the new thermally oscillating technique, the values in Table 5-1 will be used to validate and establish confidence in the new method.

5.3 Bulk Validation

Before showing the various results for the fluids, an illustrative example set will be processed to note some additional details regarding the fitting procedure and techniques used to determine the fits. The thermal data obtained in PEO 0.3% will be discussed in the context of the theory and procedure that was put forth in chapter 4.

5.3.1 Squeeze-film analysis to determine η_0

Recalling the procedural flow in chapter 4, once the first mode of the beam had been fit with a SHO model, the values for k_C was passed to the squeeze-drag analysis. Since this data was only in the bulk, only drag forces were considered.

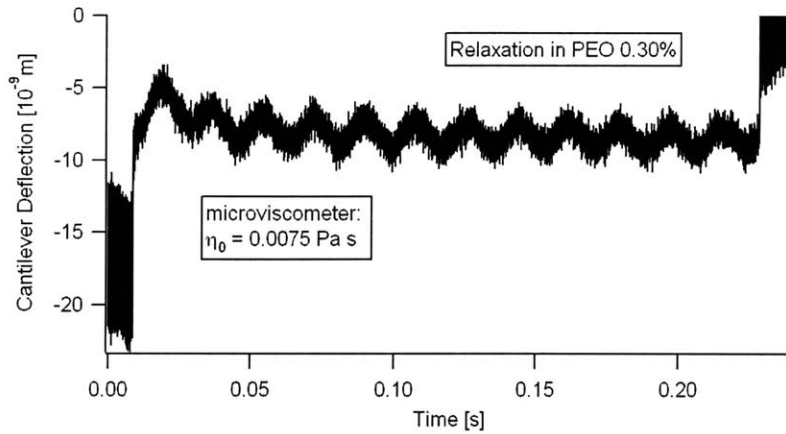


Figure 5-15: Cantilever relaxation in PEO 0.3%: $k_C=0.02N/m$, $\delta=8.9nm$, $V_{probe}=53.5\mu m/s$

To compute viscosity, only the deflection in steady-state motion had to be measured, which was $8.9nm$ for the data in Figure 5-15. The value for the deflection, δ , was determined by either measuring the mean of the two data levels, as seen in Figure 5-15, or fitting the data to equation (5.5).

$$w(L) = \delta \left(1 - e^{-L/\tau}\right) \quad (5.5)$$

Equation (5.5) was used when the viscosity of the fluid such that the relaxation looked like an R-C circuit response, where $\tau \approx \frac{\eta L}{k_c}$. The static deflection value, in conjunction with the user defined variables for the cantilever dimensions, were then used to compute η_0 as discussed in Chapter 4.

One final comment should be made about the observed oscillations seen in Figure 5-15. These type of oscillations were seen in the aqueous type viscosity fluids. Similarly, they all have the same frequency of 60Hz, which is indicative of both electrical and low frequency building vibrations. Since 60Hz was well below any frequencies used in the results to follow, this low frequency oscillation had no impact on the data. As will be seen, Figure 5-18, Figure 5-20 and Figure 5-22 exhibited the same low frequency component.

5.3.2 Fit new FSI theory to spectrum to determine λ

As discussed in the procedural flow, the cantilever dimensions and material properties were also used for the beam theory. The resulting theoretical spectrum and measured spectrum were compared to ensure the location and quality of the modes was correct.

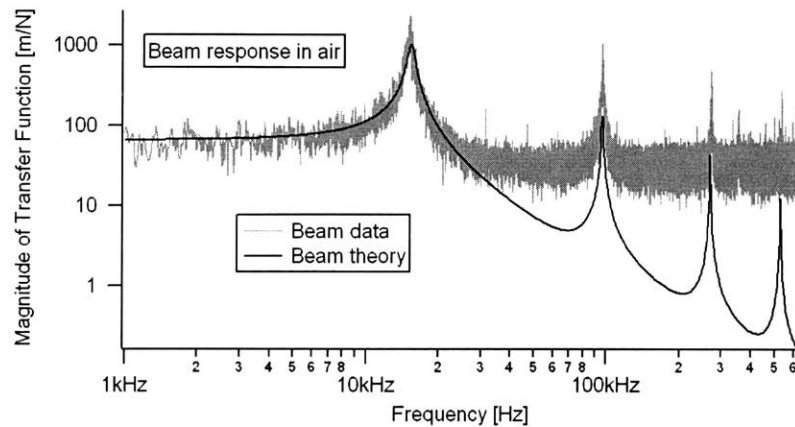


Figure 5-16: The measured beam response in air, which resulted in m_C , b_C and k_C , was used to check the beam theory output.

Mode	f_{theory}/f_{fit}	k_{theory}/k_{fit}
1	15.3 kHz / 15.2 kHz	0.015 N/m / 0.016 N/m
2	96.7 kHz / 96.8 kHz	0.594 N/m / 0.15 N/m
3	270 kHz / 273 kHz	4.65 N/m / 0.60 N/m
4	530 kHz / 538 kHz	17.8 N/m / 1.5 N/m

Table 5-2: Comparison of beam theory and experimental data

Figure 5-16 and Table 5-2 shows that the agreement with the modal location was good to within 0.1% for all modes. However, the relative stiffness becomes progressively worse. This was a consequence of trying to fit a SHO model to a smaller and smaller portion of the measured response. This initial correlation was essential since any error in modal locations in the beam theory would cause the user to overcorrect when fitting the modes of the visco-elastic FSI (VE-FSI) theory.

The next procedural step was to use m_C , b_C and k_C to convert the measured data to a transfer function and use η_0 , from the drag analysis, to calculate the VE-FSI. To correct for the difference between an infinite translating cylinder and a cantilevered beam, the value for m_{add}

and b_{add} were multiplied by 0.29, in the same way it was shown in chapter 3 that

$$m_{eff} = 0.247 m_{cantilever}$$

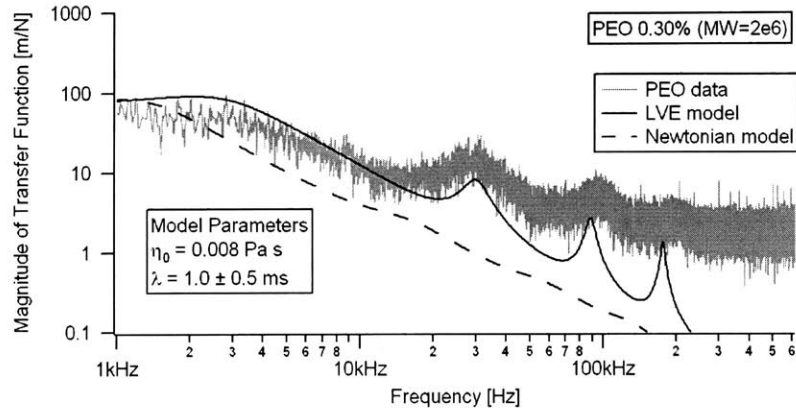


Figure 5-17: Visco Elastic FSI theory was fit to the measured response of the beam in PEO 0.3%.

It was found that the best method for determining the fit was to enter η_0 and $\lambda = 10^{-10} s$, practically Newtonian, and adjust λ until the higher modes had the same location and quality. Determination of λ was subject to the user's interpretation, but there was a clear range, outside of which, that agreement was not acceptable. This subjectivity in the modal location and quality was illustrated in Figure 5-17. The mode locations do not agree exactly, but emphasis was usually given to the 2nd mode since it was not heavily damped and was above the noise floor. The noise floor, which incorrectly appears to have decreased from Figure 5-16 to Figure 5-17, will be discussed in Chapter 7 and its effect on how well the higher modes agree with the data will be discussed. Ultimately, this subjectivity was quantified with the ranges for values shown in each of the figures where the VE-FSI theory was fit to the data.

5.3.3 Visco-Elastic FSI Bulk Validation Data

This section will show and discuss the data associated with computing η_0 and λ for a range of fluids. After which, the values determined by the thermal VE-FSI method will be compared

with the values of Table 5-1. In keeping with the illustrative PEO example some more PEO results, of varying concentrations, will be presented in addition to some lubricant base stocks.

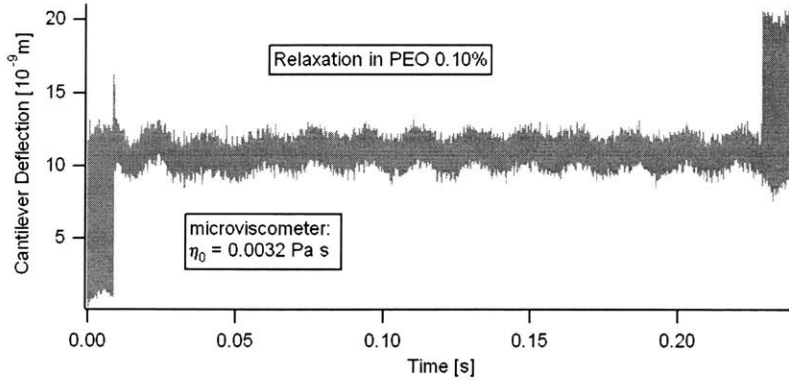


Figure 5-18: Cantilever relaxation in PEO 0.1%: $k_C=0.02N/m$, $\delta=3.8nm$, $V_{probe}=53.5\mu m/s$

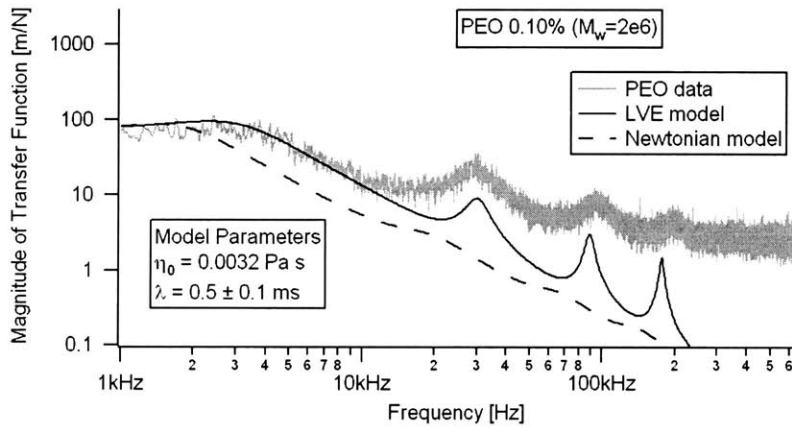


Figure 5-19: Visco Elastic FSI theory fit to the measured response of the beam in PEO 0.1%.

Figure 5-18 and Figure 5-19 presents the results for PEO 0.1%. The value for η_0 was exactly that of Table 5-1. The agreement between the λ values was not as exact. In fact, it was almost an order of magnitude lower for the VE-FSI method. It was expected that this new method might give lower values for λ since it measured the fluid about an equilibrium state, while the CaBER measured λ in a highly strained state. More discussion on the correlation between these methods will be given in a later section.

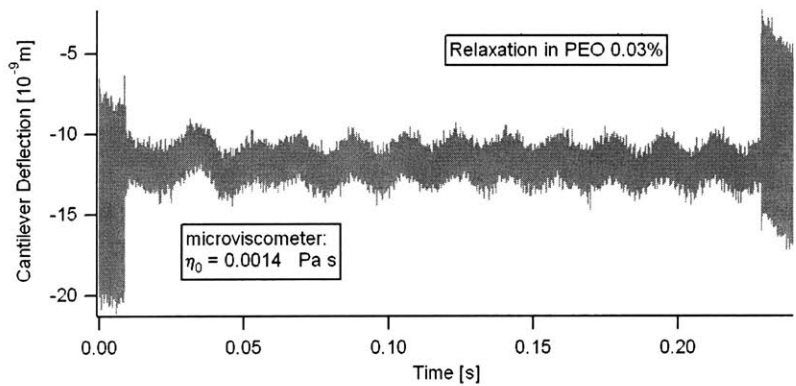


Figure 5-20: Cantilever relaxation in PEO 0.03%: $k_C=0.017N/m$, $\delta=1.9nm$, $V_{probe}=53.5\mu m/s$

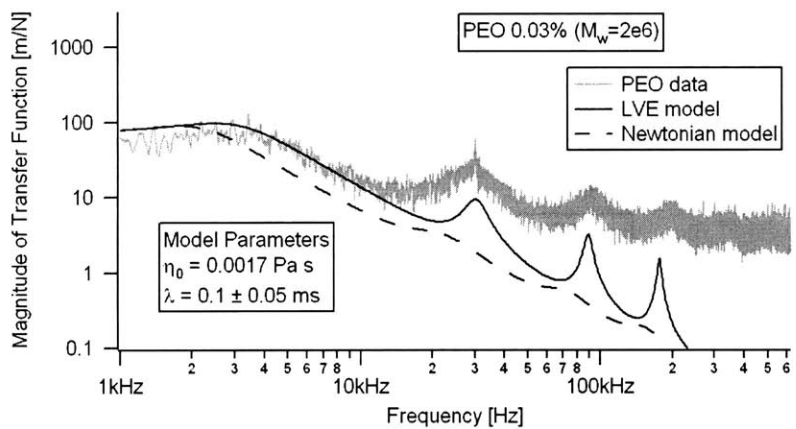


Figure 5-21: Visco Elastic FSI theory fit to the measured response of the beam in PEO 0.03%.

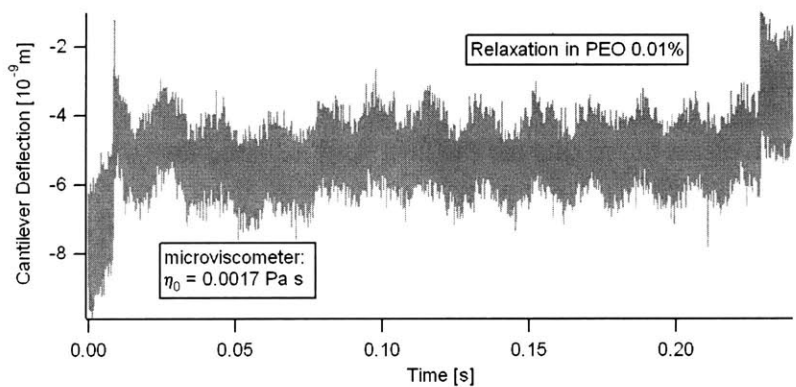


Figure 5-22: Cantilever relaxation in PEO 0.01%: $k_C=0.02N/m$, $\delta=2.0nm$, $V_{probe}=53.5\mu m/s$

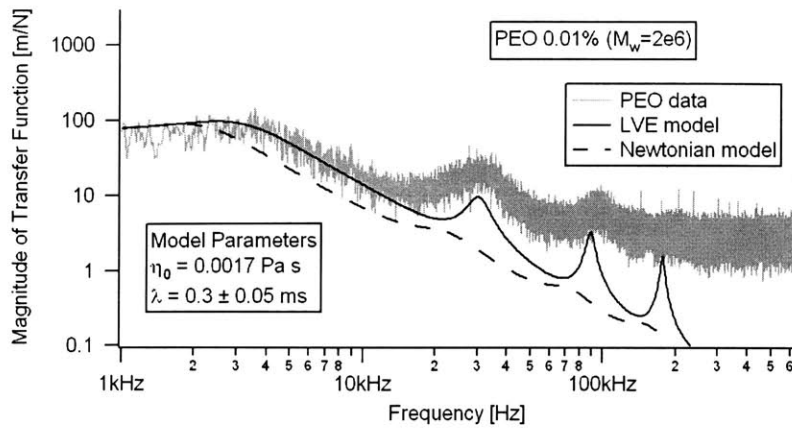


Figure 5-23: Visco Elastic FSI theory fit to the measured response of the beam in PEO 0.01%.

Figure 5-20 through Figure 5-23 give the results for PEO 0.03% and PEO 0.01%. As before, the η_0 values agreed quite well, but the λ values were again lower. Recall that these values for λ in Table 5-1 are from Zimm theory, which comes from kinetic theory of polymers. Zimm theory is thought to be an idealized lower limit, therefore, lower λ values obtained with the VE-FSI theory were not expected in this instance. However, it was clear from the plot of Figure 5-21 and Figure 5-23 that this new VE-FSI model was required to capture the probe dynamics. The Newtonian FSI was not adequate and the variation between the two theories was very sensitive to the λ value, which was why the error range on λ values was only $100\mu\text{s}$. The more viscous PEO 1.0% and 3.0% solutions will be discussed later.

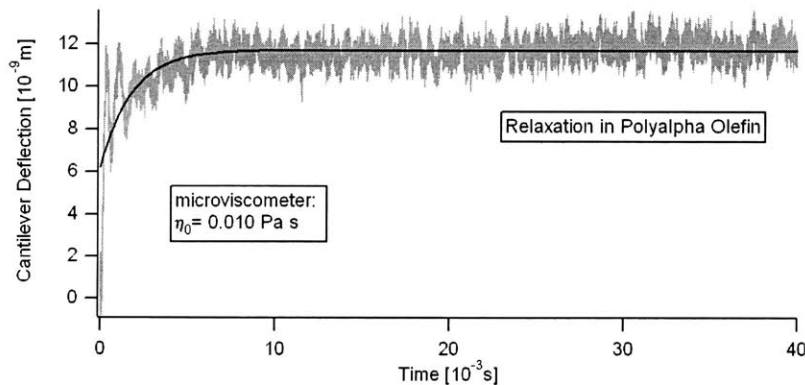


Figure 5-24: Cantilever relaxation in PAO: $k_c=0.02\text{N/m}$, $\delta=11.7\text{nm}$, $V_{probe}=53.5\mu\text{m/s}$

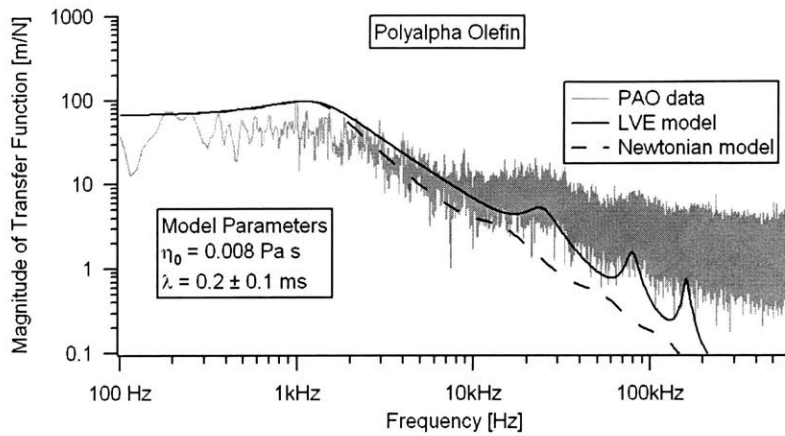


Figure 5-25: Visco Elastic FSI theory fit to the measured response of the beam in polyalpha olefin.

Figure 5-24 and Figure 5-25 give the results for a common lubricant base stock, PAO. Again, η_0 agreed well and λ was less than the CaBER results. Note that the drag data in Figure 5-24 was fit with equation (5.5). This was the preferred method for measuring δ , provided the fluid was viscous enough such that $\tau \sim \frac{\eta_0 L}{k_c}$ was sufficiently large enough to observe the cantilever relaxation.

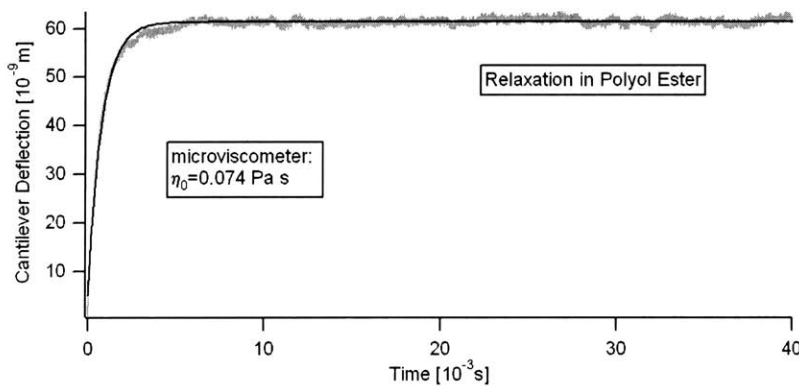


Figure 5-26: Cantilever relaxation in POE: $k_c=0.02N/m$, $\delta=61nm$, $V_{probe}=37.2\mu m/s$

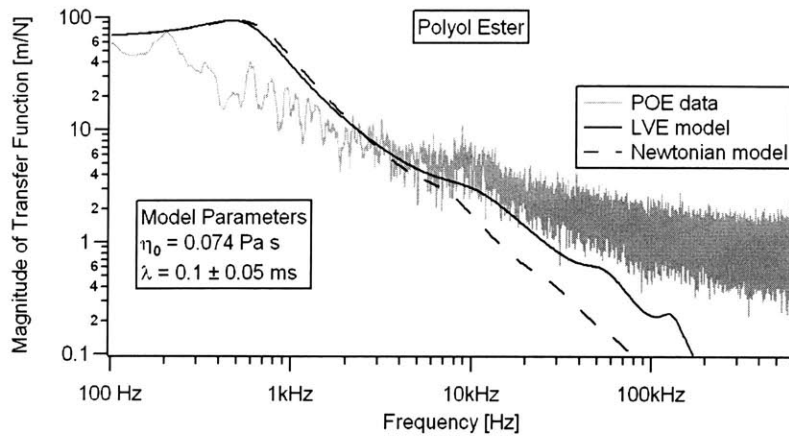


Figure 5-27: Visco Elastic FSI theory fit to the measured response of the beam in polyol ester.

Figure 5-26 and Figure 5-27 give the results for POE. Again, η_0 agreed very well and λ was definitely less than the given range in Table 5-1, $<1ms$. However, the previous fluid viscosities were one to ten times that of water. The viscosity of POE is 74 times larger than water. Therefore there was a change in the agreement of the VE-FSI theory fit. Although the emphasis on the fit was still the 2nd mode, the large discrepancy in the 1st mode raises questions about using the simple SHO model for such highly viscous fluids. Despite the disagreement with the first mode, the location and quality of the 2nd mode was again very sensitive to λ , and a good fit was determined. The viscous limits on the FSI theory will be discussed in chapter 6.

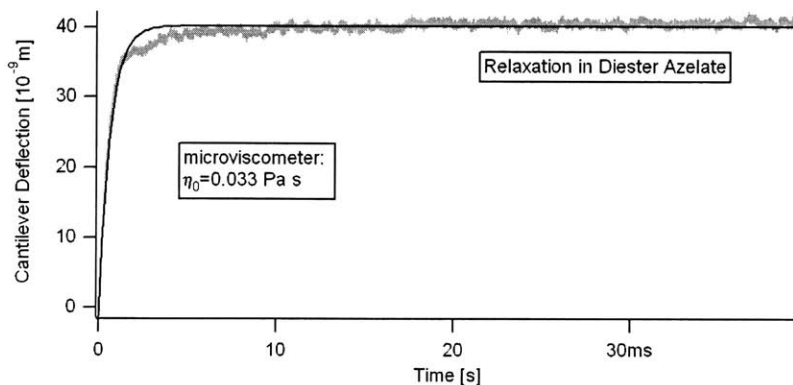


Figure 5-28: Cantilever relaxation in DEA: $k_c=0.02N/m$, $\delta=39nm$, $V_{probe}=53.5\mu m/s$

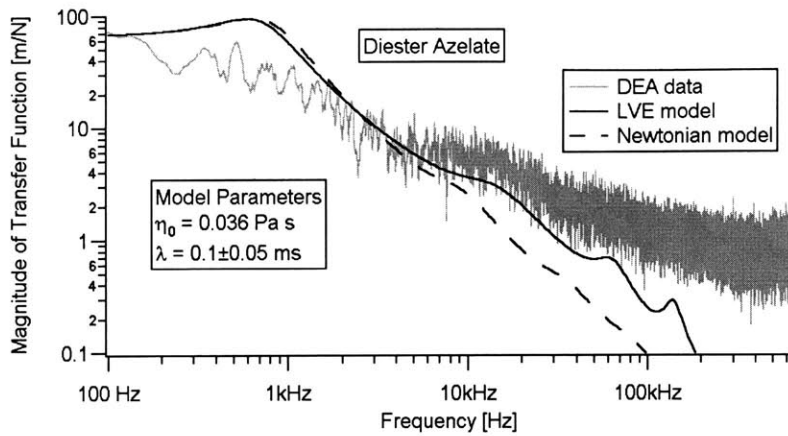


Figure 5-29: Visco Elastic FSI theory fit to the measured response of the beam in diester azelate.

Figure 5-28 and Figure 5-29 give the results for DEA. As with the POE data, the fit in Figure 5-29 does not agree with the 1st mode, but the discrepancy is less since the viscosity is about half that of POE. The error range on λ was still only $100\mu\text{s}$ due to the sensitivity of the 2nd and 3rd mode on the value of λ .

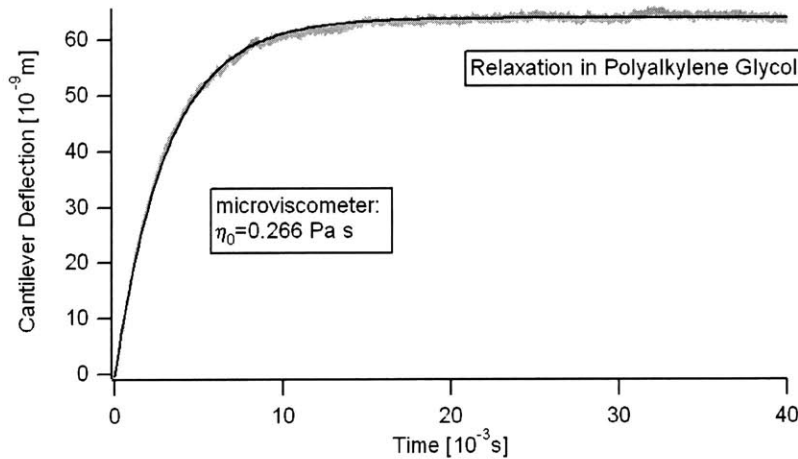


Figure 5-30: Cantilever relaxation in PAG: $k_C=0.017\text{N/m}$, $\delta=64\text{nm}$, $V_{probe}=9.3\text{nm/s}$

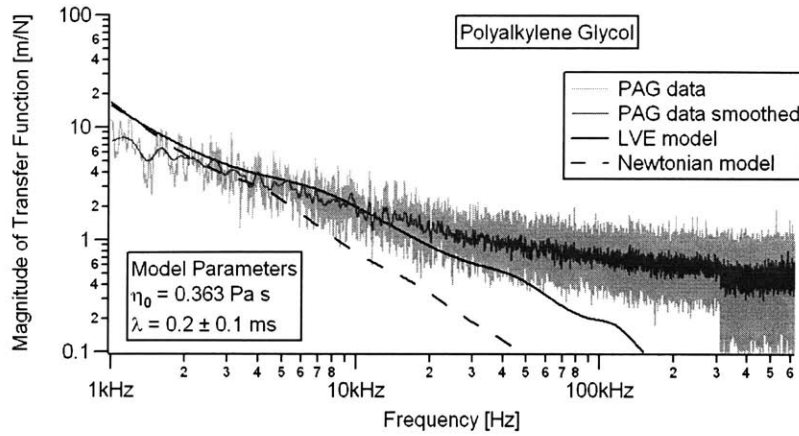


Figure 5-31: Visco Elastic FSI theory fit to the measured response of the beam in polyalkylene glycol.

Figure 5-30 and Figure 5-31 show the results for PAG. The viscosity of PAG is 363 times that of water. Coupled with the fact that PAG has little elasticity, as seen by the CaBER results, all modes were heavily damped. This dramatically reduced the sensitivity of the VE-FSI model to λ , which is why the value in Figure 5-31 was $\lambda=(0.2\pm 0.1)ms$, 50% error. This interplay between η_0 and λ , on the ability to resolve changes in the VE-FSI theory, defines an accessible parameter space, which will be discussed later in chapter 6.

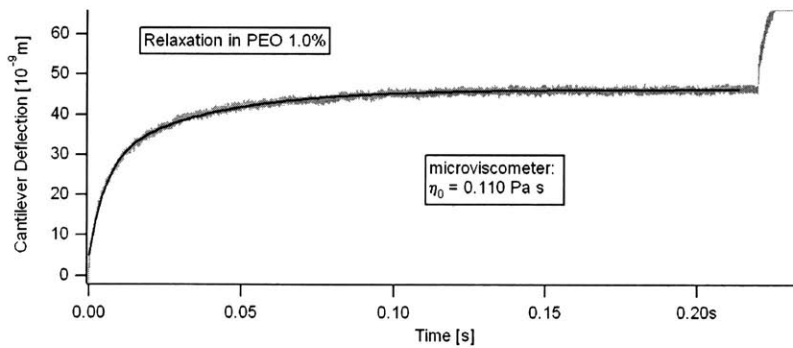


Figure 5-32: Cantilever relaxation in PEO 1.0%: $k_C=0.02N/m$, $\delta=45nm$, $V_{probe}=18.6\mu m/s$

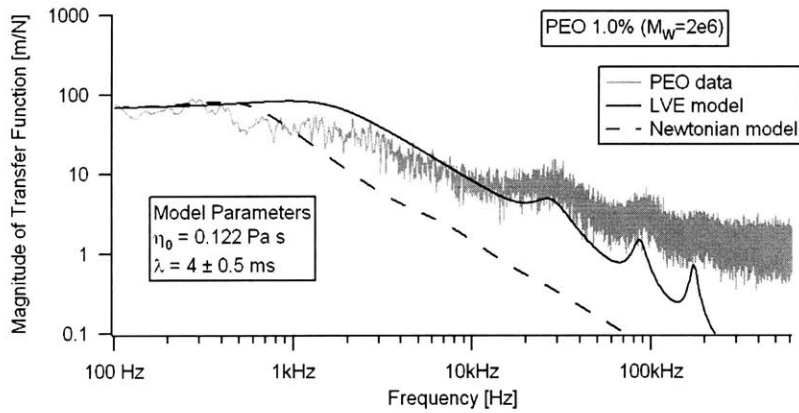


Figure 5-33: Visco Elastic FSI theory fit to the measured response of the beam in PEO 1.0%.

Figure 5-32 and Figure 5-33 were the results for PEO 1.0%. Although the viscosity was the same order as PAG, the modes were dramatically enhanced due to the elasticity of the high molecular weight PEO molecules. Although there was some disagreement in the 1st mode, the 2nd, 3rd and 4th modes agreed very well. Again, λ obtained via the VE-FSI theory was less than that of the CaBER.

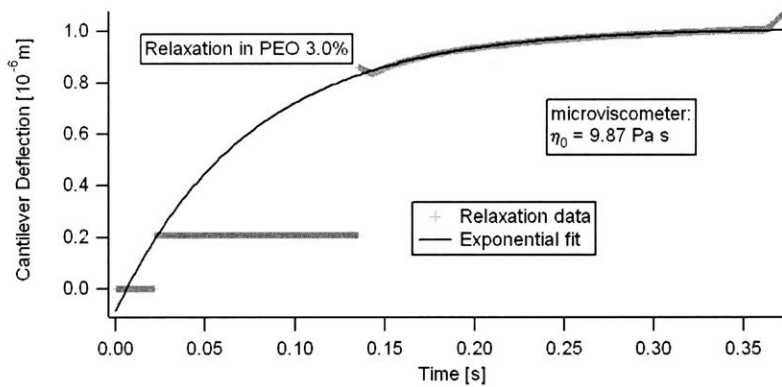


Figure 5-34: Cantilever relaxation in PEO 3.0%: $k_c=0.02\text{N/m}$, $\delta=1.011\mu\text{m}$, $V_{probe}=9.3\text{nm/s}$

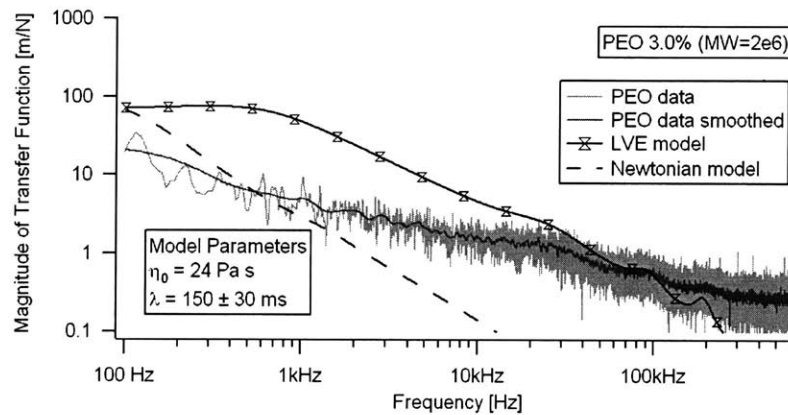


Figure 5-35: Visco Elastic FSI theory fit to the measured response of the beam in PEO 3.0%.

Figure 5-34 and Figure 5-35 were the results for PEO 3.0%. Due to the very large viscosity, $\eta_0=24(Pa s)$, relative to the normal SPM probe environment, this represented a limiting case for the thermal VE-FSI method. For the viscosity calculation, Figure 5-34, the data was offset to fit equation (5.5). The horizontal data below 150ms is artificial data to offset the actual cantilever relaxation data. The real impact of such high viscosity, as well as the true utility of this thermal method, is best illustrated in Figure 5-35. Recall the premise of using the higher modes. Despite lower modes being largely dissipated, the higher modes were probing the elasticity. In Figure 5-35, the 1st nor the 2nd mode agree with the data. In fact, for the first time, the 2nd mode is not the primary focus. The fit to this data focused on the 3rd and 4th modes, which still persisted in the measured data, despite the large viscosity. As stated, the interplay that limits access to certain combinations of η_0 and λ will be discussed in chapter 6. In spite of the heavy dampening, the fit value for λ was only 25% less from the CaBER value.

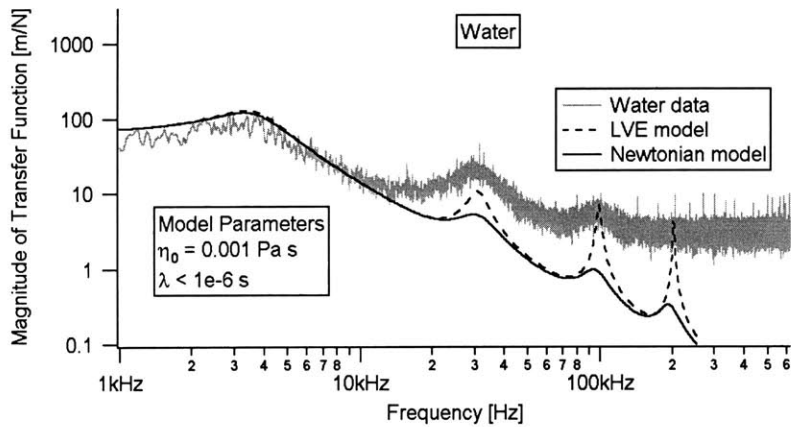


Figure 5-36: Visco Elastic FSI theory fit to the measured response of the beam in water.

On the other end of the viscosity spectrum, where $\eta_0=10^{-3}(Pa s)$, one cannot distinguish below $\sim 1\mu s$. In Figure 5-36, the dashed line is for $\lambda=5\mu s$ to illustrate the sensitivity of the VE-FSI theory to λ . Although the “relaxation” time of water is speculated to be on the order of ps , from the perspective of this new method, the best one can say is that this fluid has a relaxation time of $\lambda < 1\mu s$.

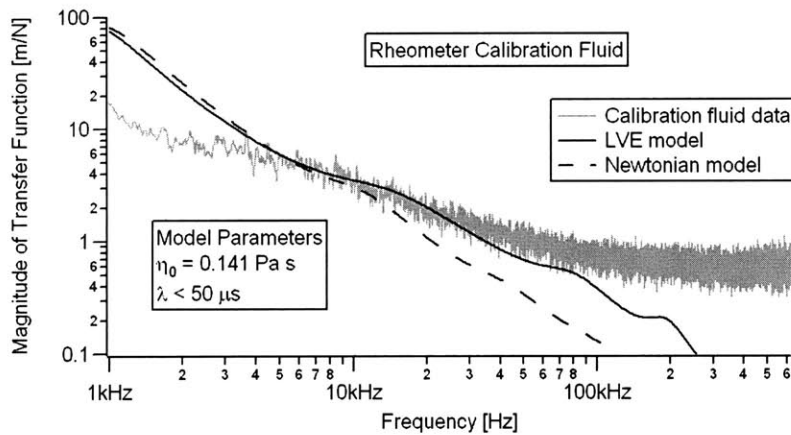


Figure 5-37: Visco Elastic FSI theory fit to the measured response of the beam in calibration fluid.

Similar to the viscosity of PEO 1.0%, but without the elasticity, Figure 5-37 gives the fit of the VE-FSI theory to the rheometer calibration fluid. The word fit was used loosely because there were really no discernible modes in the data. In fact, the statement that $\lambda < 50\mu s$ was

determined simply by the general slope of the theory relative to the data. This was an example of where the η_0 and λ combination were outside the accessible parameter space.

Fluid	η_0 [rheometer]	η_0 [VE-FSI]	λ [CaBER™]	λ [VE-FSI]
Diester Azelate	0.036 Pa s	0.033 Pa s	<1 ms	0.1 ms
PolyAlphaOlefin	0.008 Pa s	0.010 Pa s	0.8 ms	0.2 ms
PolyolEster	0.074 Pa s	0.074 Pa s	<1 ms	0.1 ms
PolyAlkyleneGlycol	0.363 Pa s	0.266 Pa s	<1 ms	0.2 ms
PEO 0.01%	0.002 Pa s	0.0017 Pa s	0.35 ms	0.3 ms
PEO 0.03%	0.002 Pa s	0.0014 Pa s	.035 ms	0.1 ms
PEO 0.10%	0.003 Pa s	0.0032 Pa s	4 ms	0.5 ms
PEO 0.30%	0.009 Pa s	0.0075 Pa s	7 ms	1.0 ms
PEO 1.0%	0.122 Pa s	0.110 Pa s	20 ms	4.0 ms
PEO 3.0%	24 Pa s	9.87 Pa s	190 ms	150 ms

Table 5-3: Comparison of rheometer(η_0) and CaBER(λ) data to η_0 and λ obtained from fitting the new VE-FSI theory to measured responses of the SPM probes.

Table 5-3 summarizes and compares the values of η_0 and λ obtained from rheometric and CaBER testing, respectively, with the values of η_0 and λ obtained by fitting the VE-FSI model to the measured spectral response. The results will be discussed more in the next section, but the general trend was that the viscosity measurements agreed quite well, while the VE-FSI λ values were consistently below those obtained by the CaBER.

5.4 Comparison and Discussion of Techniques

To better compare the performance of this new thermal technique, various correlations were considered. The first value computed for each data set was the viscosity.

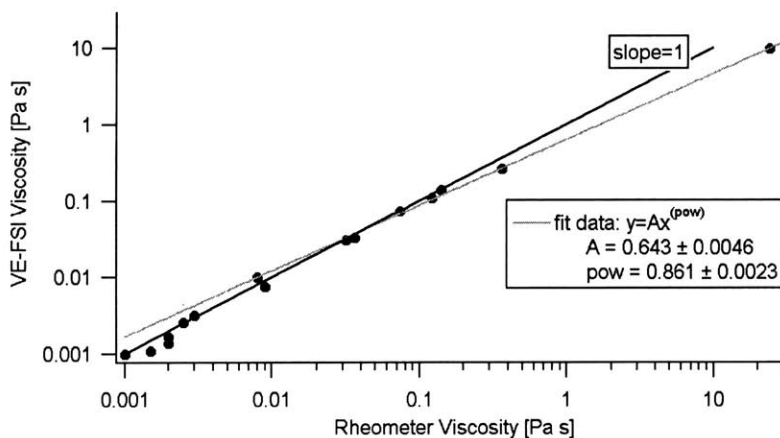


Figure 5-38: Micro viscometer viscosity versus rheometric viscosity. The dark line, with slope=1, represents a perfect correlation between the two techniques for determining viscosity.

Figure 5-38 gives the viscosity, as determined by the drag force in the micro viscometer, plotted as a function of the rheometric viscosity. The dark line represents a perfect correlation, $\eta_{micro} = \eta_{rheom}$, but the data followed a slightly lesser slope. This decreased slope was due to the error associated with fitting the partial relaxation data for the high viscosity fluids such as Figure 5-32 and Figure 5-34, where the micro viscometer values were below the rheometer value for η_0 .

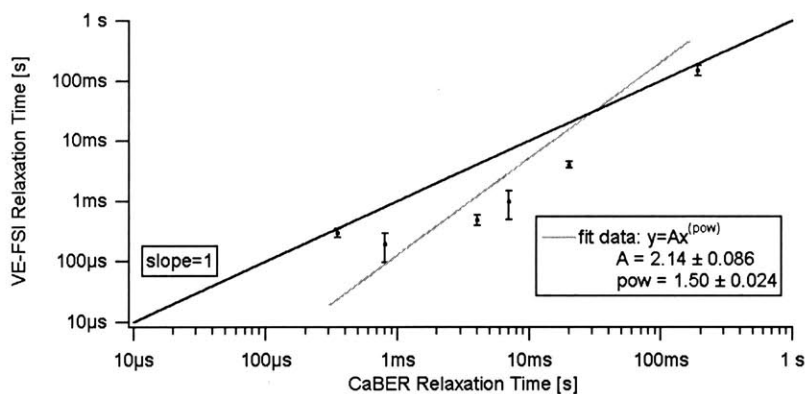


Figure 5-39: VE-FSI relaxation time versus CaBER relaxation time. The dark line, with slope=1, represents a perfect correlation between the two techniques for determining relaxation time.

Figure 5-39 is analogous to Figure 5-38, but compares the VE-FSI λ values with CaBER λ values. Again, the dark line represented a perfect correlation between the two techniques,

$\lambda_{FSI} = \lambda_{CaBER}$. Consistent with the expectation that $\lambda_{FSI} < \lambda_{CaBER}$, the data in Figure 5-39 was below the dark line. The difference in slope is consistent with the fact that the CaBER resolution, $\sim 1ms$, would increase the correlation slope between the two techniques. Nevertheless, the λ_{FSI} values possessed the correct trend and, the values $> 1ms$, have the same order of magnitude as λ_{CaBER} .

Another comparison of the relaxation times was to consider the dependence on PEO concentration.

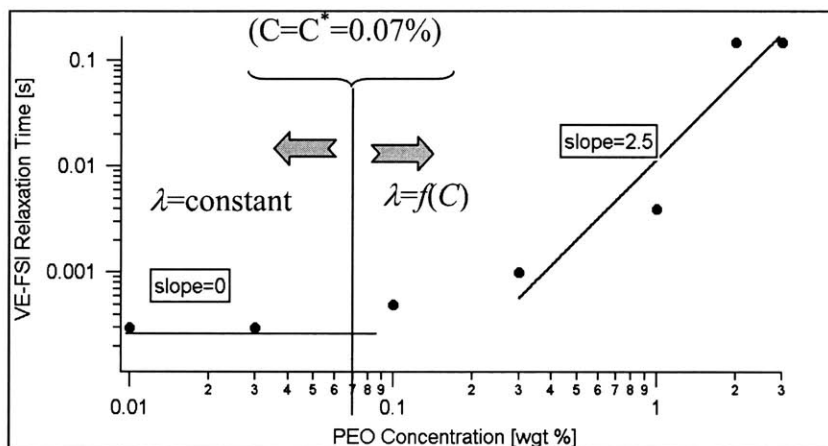


Figure 5-40: Relaxation time of PEO ($M_w=2e6$) was independent of concentration in the dilute regime, and had a power law slope of 2.5 at higher concentrations.

It was noted that varying solutions of PEO were chosen for testing because η_0 and λ could be varied over a wide range by adjusting the concentration. Figure 5-40 was the resulting relaxation times plotted as a function of % weight concentration. In the dilute regime, where polymers are assumed not to interact, Zimm theory applies, which has no dependence on concentration since each polymer does not know the other polymers exist. However, as concentration is increased, the polymers begin to interact. The concentration, C^* , at which this transition should theoretically occur was 0.07%. This corresponded to the observed transition in Figure 5-40. Above C^* there are different theories and scaling arguments regarding how the

relaxation time should depend on concentration. These correlations have power law relations that range from 1 to 3. In the data observed for the PEO ($M_w=2e6kg/kmol$) solutions above 0.1%, a slope of 2.5 was observed on a log-log plot, or the equivalent power law relation was $\lambda \sim (C)^{2.5}$.

6 Limitations of the Technique

There were several issues noted throughout the discussion of results that limited the resolution and range of the technique. The following sections serve to discuss these limitations and provide an understanding of the system's performance as a rheological tool. The first section will discuss the experimental limitations of the photo-diode and how this affected the accessible parameter space. A parameter space is a combination of viscosity and relaxation time that this technique can quantify. The next section will discuss the FSI theory breakdown at low frequencies in large viscosity fluids. The final section will discuss the impact of operating in the interfacial regime on the parameter space and address concerns regarding polymeric dimensions relative to the probe.

6.1 Experimental Limits

The noise floor dominated the higher frequencies in most of the results shown in Chapter 5.

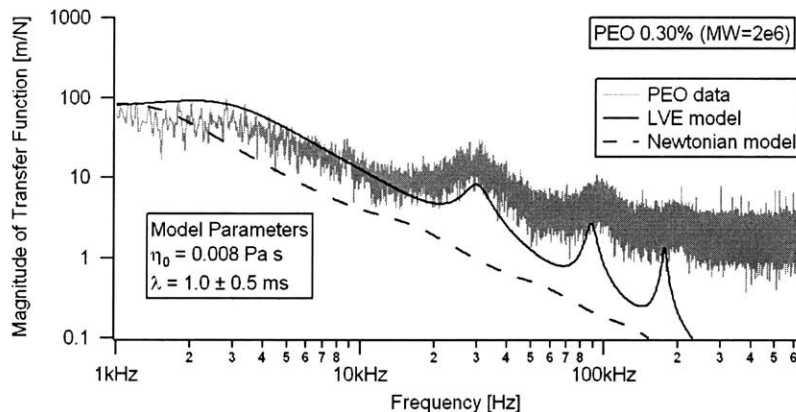


Figure 6-1: Noise in data limits the ability to fit the theoretical visco-elastic FSI at higher frequencies

The noise results in the data flattening at higher frequencies and the resulting fit of the FSI model is consequently more qualitative. In addition, it may have appeared to have different levels in different fluid environments, as noted in Chapter 5.

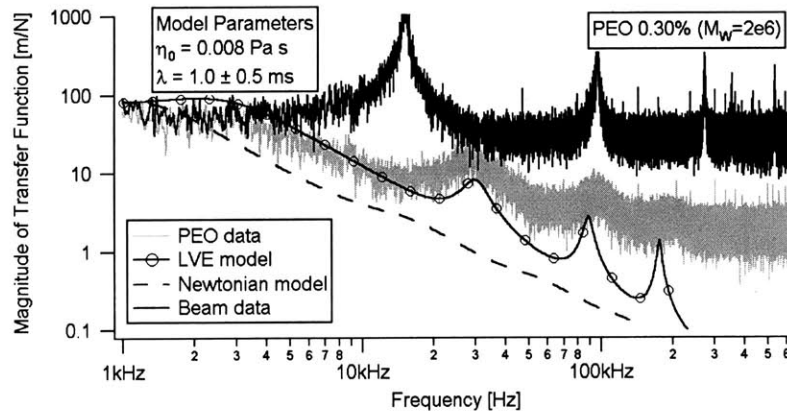


Figure 6-2: Comparison of noise level for identical setup: One spectral response is measure in air and the other response in 0.30% PEO.

Figure 6-2 illustrates the influence of noise on the spectral response of the same probe in air and a viscous fluid. It appears as though there are different noise levels associated with each response. However, it should be noted that when the spectral responses of the cantilevered beams are plotted on an axis with units of m/N , then they should all collapse at a dc value of

$\frac{1}{k_c}$, as they do in Figure 6-2.

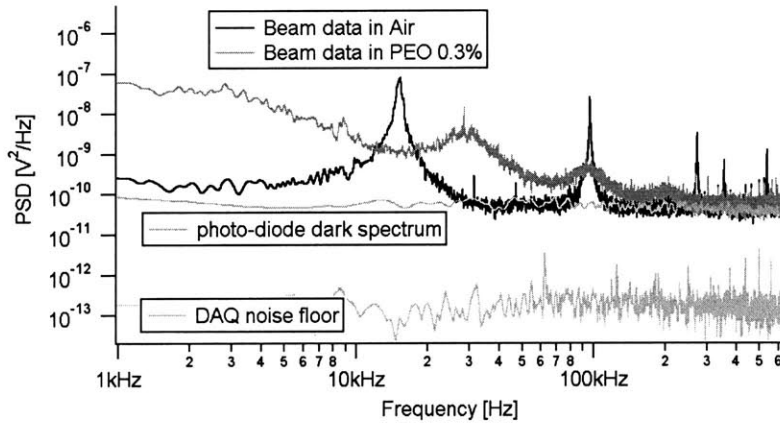


Figure 6-3: Comparison of voltage PSD data for different dissipative environments with noise contributions from the DAQ system and photo-diode dark current

To discuss the noise in the system it is better to view the spectral response of the probe on a voltage PSD scale, see Figure 6-3. These were the measured spectra prior to scaling them to transfer functions, recall equation (6.1) and (6.2).

$$|H| = \sqrt{\frac{S_{out}}{S_{in}}} \quad (6.1)$$

$$S_{in} = 4k_B T b(\eta) \quad (6.2)$$

Accordingly, the plots were scaled differently, depending on the dissipative, η_0 , effects of the environment. Since S_{in} was larger for the more viscous fluid environment the transfer function plot in Figure 6-2 has a lower value. The comparisons in Figure 6-3 show that the noise floor in the system was dominated by the noise from the photodiode, which had a flat noise floor over the frequencies of interest.

To better compare the effect of the photodiode noise, $S_{PD}=10^{-10} V^2/Hz$, this value was included in the measured voltage response. When the voltage power spectrum was then converted to a transfer function, the noise floor would be scaled accordingly to give theoretical plots that were better compared to the experimental results see in Figure 6-2.

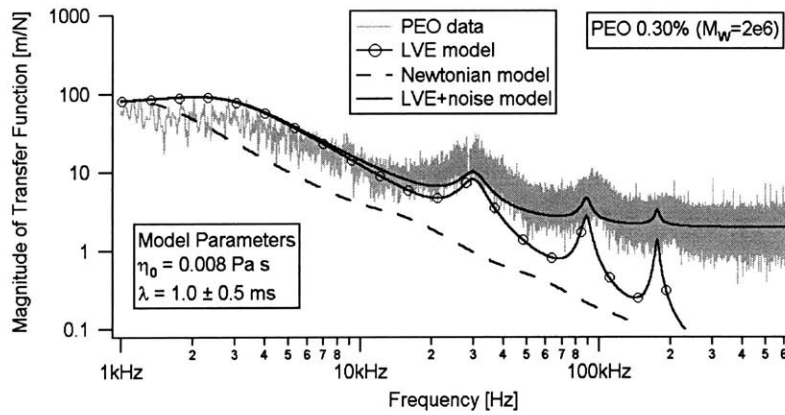


Figure 6-4: FSI theory + photodiode noise fit to measure response of cantilever in 0.30% PEO

Figure 6-4 shows the FSI with the photodiode noise floor included in the theory. This modification allows for a more direct comparison of the observed spectra and theory. Although the relaxation time was still quantifiable, this modified theory illustrates how the noise floor eliminates a significant amount of the spectrum available for fitting.

This limitation is what defined a parameter space. A parameter space was a combination of viscosity and relaxation time that were quantifiable by this technique. To understand this limitation, consider a fluid with the same viscosity as 0.30% PEO, but with a smaller relaxation time.

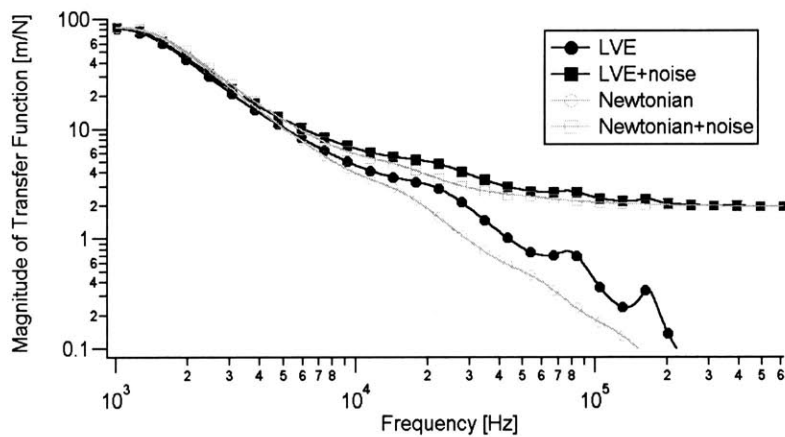


Figure 6-5: Noise floor limits the resolution of λ , such that only $\lambda > 50 \mu s$ was resolvable for $\eta_0 = 8e-3 Pa s$ with a $PSD_{noise} = 10^{-10} V^2/Hz$

Figure 6-5 shows the Newtonian and visco-elastic FSI with and without the inclusion of the photodiode noise. The plots are for $\lambda=50\mu s$ and $\eta_0=8e-3Pa s$. Although the original theory, without noise, is easily distinguished between the Newtonian and visco-elastic models, the modified models, with the noise floor, limits the resolution of λ to values greater than $50\mu s$. In contrast, if there were no noise floor, then the theoretical resolution limit for a fluid with $\eta_0=8e-3Pa s$ would be $\lambda=5\mu s$. That means that the noise floor reduces the relaxation time resolution by an order of magnitude.

Practically there will be a limit to how low the noise floor can be reduced, but consider the effect of reducing the noise floor.

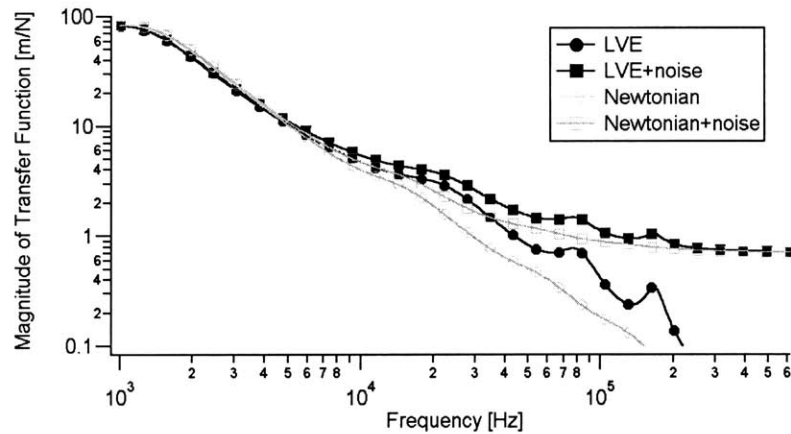


Figure 6-6: Noise floor limits on λ : $\lambda > 20\mu s$ for $\eta_0=8e-3Pa s$ with a $PSD_{noise}=10^{-11}V^2/Hz$

As shown in Figure 6-6 if the noise floor were reduced 1 order of magnitude then one can distinguish $\lambda > 20\mu s$. This leads to a discussion of the theoretical accessible parameter space verses current experimental limitations and what improvements are required to practically use the first four modes of the probe. If one wants to use more than four modes, or a cantilever with higher mode locations, the required noise floor would be accordingly lower.

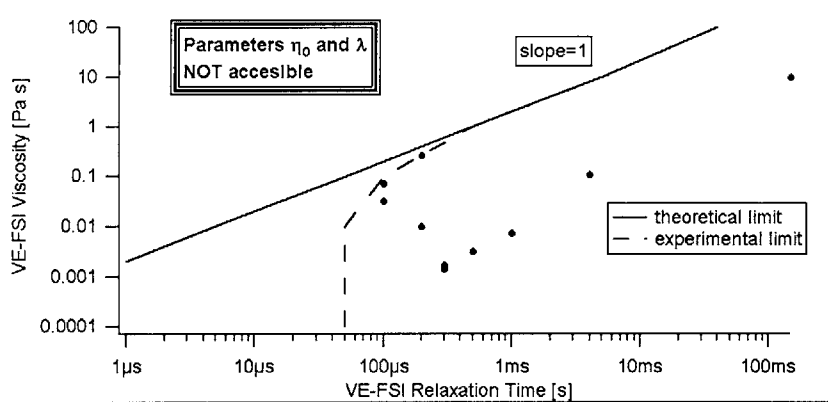


Figure 6-7: Accessible parameter space (combination of η_0 and λ) that the thermally oscillating VE-FSI method can probe. The solid and dashed boundary was determined by consideration of the theoretical changes observed by systematically varying both η_0 and λ .

Several times now, the accessibility to certain combinations of η_0 and λ , viscosity and relaxation time, has been noted. Figure 6-7 represents the parameter space of the results shown in chapter 5, which were obtained with the thermal procedure. The solid line in Figure 6-7 represents the theoretical limit, no noise floor, beyond which λ was not discernable given a measured η_0 . This limiting boundary was determined from a purely theoretical consideration of the influence of λ on the VE-FSI model compared to the Newtonian response without the influence of the noise floor. The dashed line represents the limit of the current experimental hardware as determined by including the noise into the FSI model, analogous to Figure 6-5. The accessible parameter space makes sense because of equation (6.2), which states that the driving power increases with viscosity. That translates to an increased SNR and minimizes the effect of the noise floor. Consequently, the experimental limit in Figure 6-7 approaches the solid line with increasing viscosity, representing the theoretical limit.

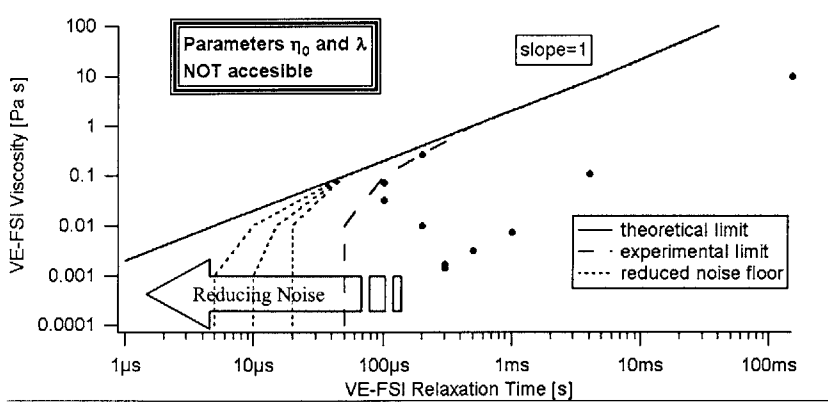


Figure 6-8: Expansion of accessible parameter space by reduction of photodiode noise floor. Each successive dashed line represents 1 order reduction in the noise floor.

Continued reduction of the noise floor leads to the plots in Figure 6-8. Each dashed line to the left represents 1 order reduction in the noise floor, the far left dashed line representing a noise level of $10^{-13} V^2/Hz$. There are photodiodes packages, including sum and difference amplifiers, by Pacific Silicon Sensor that have a theoretical noise floor of $3e-16 V^2/Hz$, which would allow one to take full advantage of the first four modes in the presently described system. At this point, the limiting factor would become the sampling rate. Recall that changes in the FSI are only observed up to the nyquist frequency such that $\lambda > \frac{1}{2\pi f_{nyq}} = 250ns$ for the given experimental setup.

6.1.1 Low Frequency Viscous Limit of FSI Theory

Recall in the results section, the lower modes began to disagree with the observed data as the viscosity of the fluid was increased. This was a consequence of the fact that the calculation of the force acting on the translating cylinder assumed that the penetration depth, $\sqrt{\nu/\omega}$, into the

fluid was not orders of magnitude larger than the width of the probe. From the testing discussed in this thesis, this lead to equation (6.3).

$$f > \frac{\eta}{900\rho D^2} \quad (6.3)$$

This states that the FSI model is only valid, for a given fluid and cantilever, above certain frequencies. Case in point, the limiting frequency for the 3% PEO was approximately 70kHz, which agrees with the data presented in the results section. However, this is not a limiting effect. Recall the reason for using the higher modes in the first place was to eliminate use of the over damped lower modes in high viscosity fluids. However, this effect should be considered when fitting the models to the spectra.

6.2 Scaling limits

6.2.1 Polymer size and concentration effects

In general, small amplitude motion is desired to linearly deform a fluid about an equilibrium position. For thermally driven oscillations of the cantilevers, the amplitude of oscillation is much smaller than the cantilever dimensions. However, when the probe amplitude is on the same order as the polymer, which is the source of visco-elasticity, one needs to ensure that the probe is interacting with sufficient numbers of polymers to provide a measure of the mixture's rheology. For instance, if the probe oscillations were too small in a dilute solution, then the probe may not even interact with the polymers and relating the spectral response of the probe to rheological properties of the mixture becomes questionable.

To quantify how many polymers are interacting with the cantilevered probes discussed in this thesis, first consider the size of the polymer in solution. The characteristic size of a polymer in a solution is characterized by its radius of gyration[46], given by (6.4).

$$\langle \overline{R_g^2} \rangle = \alpha^2 C_\infty \left(\frac{M_w}{3M_0} \right) l^2 \quad (6.4)$$

In this relation, R_g is the effective radius of the polymer, α characterizes how much the polymer swells in the given solvent, l and C_∞ relate to the chemical bond lengths and the ability of the polymer to rotate given its chemical bond angles, respectively. M_w is the polymer molecular weight and M_0 is the molecular weight of the repeating monomer. For the PEO solutions discussed in this thesis these parameters are given by the following equations.

$$M_w = 2e6 \frac{kg}{kmol} \quad (6.5)$$

$$l = 1.54e(-10)m \quad (6.6)$$

$$C_\infty = 4.1 \quad (6.7)$$

$$\alpha = 1.499 \quad (6.8)$$

The repeating chemical structure for PEO is $(O-CH_2-CH_2)_n$, which has a molecular weight of

$$M_0 = 44 \frac{kg}{kmol} \quad (6.9)$$

For these values the radius of gyration evaluates to equation (6.10) and (6.11).

$$\langle \overline{R_g^2} \rangle = 3.3e(-15)m^2 \quad (6.10)$$

$$\overline{R_g} = 57nm \quad (6.11)$$

This is at least an order of magnitude less than any dimension of the cantilevered probe:

$$L=200\mu m, W=20\mu m, t=0.6\mu m.$$

To quantify the number of molecules interacting with the probe, the number density, equation (6.12), was multiplied by the swept volume of the cantilever.

$$n = c\rho_w \left(\frac{N_A}{M_w} \right) \quad (6.12)$$

The variables ρ_w and N_A are the density of water and Avogadro's number, respectively. The weight percent concentration, c , is the independent parameter varied in the PEO results of Chapter 5.

To compute the volume, consider the spatial modes of the beam, which were discussed in the theory section for beam dynamics. Recall the normalized deflection of the fundamental mode, Figure 6-9.

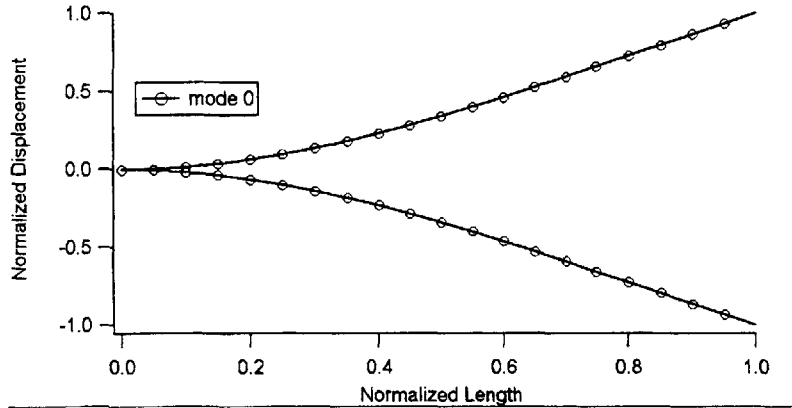


Figure 6-9: Area between lines represents the area swept by the thermally oscillating cantilever for the fundamental mode. The higher modes swept larger volumes so only the fundamental mode is considered since it represents the minimum volume.

The energy associated with each mode of vibration of the beam is given by equation (6.13).

$$\frac{1}{2}k_B T = \left\langle \frac{1}{2}k_C x^2 \right\rangle \quad (6.13)$$

This results in an amplitude of oscillation for the thermally oscillating beam of $x_t=0.46nm$.

Substituting this into equation (6.14)

$$\int_0^L \sqrt{\frac{k_B T}{k_C}} [X_j - (-X_j)] (W dx) \quad (6.14)$$

and the resulting swept volume of the fundamental mode is $V_{swept}=14.4e(-18)m^3$.

The final step is to multiply the number density by the swept volume, $N=nV_{swept}$, and the resulting number of molecules in contact with the cantilever is given by equation (6.15).

$$N = c(4.3e6molecules) \tag{6.15}$$

For the lowest concentration discussed in this thesis, 0.01% PEO, that translates to $N=43000molecules$ interacting with the cantilever. This value is proportionally 300 times larger for the 3% PEO solution, $N=13e6molecules$. Therefore, the spectral response of the probe, for the results discussed in this thesis, represented the response of the polymer solution.

6.2.2 Effect of Viscous Boundary on Parameter Space

The final issue that needs to be addressed is the effect of scaling this technique to be used in the interfacial regime. As the probe approaches the interface, the dissipative effects are expected to increase as a consequence of the boundary.

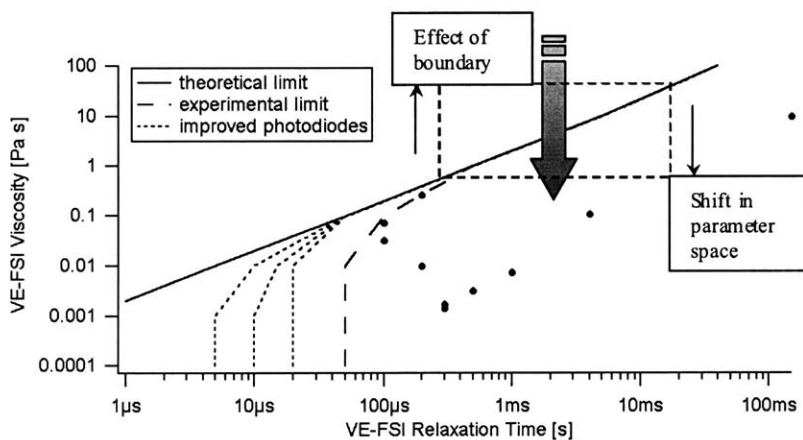


Figure 6-10: As the viscous boundary is approached, the dissipation of the cantilever oscillations reduce the accessible parameter space for this technique.

To understand how this increased dissipation would affect the accessible parameter space, refer to Figure 6-10. As the probe approaches the boundary, there will be an increase in the dissipation, therefore, moving up the left side of the dashed box. As a result, the minimum relaxation time that can be resolved must increase. The equivalent net effect is a downward shift in the parameter space boundary lines.

This will reduce the available combination of viscosity and relaxation time that can be quantified with this technique. Balancing the reduction in the parameter space, the increased dissipation will improve the SNR at high frequencies, as discussed above, and allow the higher modes to probe the shorter times scales of the fluid response. This trade-off would be limited by the viscous limit on the FSI theory moving to higher frequencies, until the nyquist frequency was reached. For the present configuration, this is equivalent to saying that a maximum fluid viscosity of $\eta_{\max} = 900 f_{\text{nyq}} \rho D^2 = 225 \text{ Pa s}$ can be tested with this technique.

7 Conclusion

The objective of this research was to develop a method that would be able to quantify interfacial lubricant rheology. The Atomic Force Microscope (AFM) was chosen because of its spatial resolution and a separate Data Acquisition (DAQ) system was used to monitor the probe dynamics for the temporal resolution. To quantify the fluid properties, a visco-elastic FSI (VE-FSI) model was required. Starting with existing viscous FSI models, this work developed a VE-FSI model for the SPM probes, such that variations on the spectral response of the probe were related to rheological parameters.

Deflection data for thermally oscillating probes in visco-elastic fluids were converted to Power Spectral Densities (PSDs) for comparison with the VE-FSI model. Only the thermal vibrations were considered since these small, $< 1nm$, perturbations probed the fluid locally. Emphasis on both the theoretical and experimental data was on the higher modes of the probe, which deformed the more elastic, shorter time scale, response of the fluid.

A testing and processing procedure was developed to guide a user through the DAQ and post processing to extract fluid properties. The experimental data was first used to determine h , the height above the substrate where the fluid was being measured. Next, the relaxation of the cantilevers was used as a micro viscometer to quantify the viscosity, η_0 . Finally, the VE-FSI theory was fit to the experimental data to determine the relaxation time, λ . Ultimately, the user had the fluid properties, η_0 and λ , at a known height, h , above the substrate.

The results of this method were compared to rheometer (η_0) and CaBER (λ) data for varying concentrations of PolyEthyleneOxide (PEO, $M_w=2e6kg/kmol$) and several lubricant base

stocks. The results showed that this technique performed well as both a micro viscometer and a measure of fluid relaxation, λ . The viscosity values from the micro viscometer were within 30% of the rheometer data over 4 orders of magnitude. The relaxation time correlation was in less agreement, but the values were always within one order of magnitude of the CaBER™ results. More importantly, this thermal technique correctly quantified the λ dependence on PEO concentration in both the dilute and semi-dilute regimes.

The experimental and theoretical limitations of this technique were discussed in chapter 6. Specifically, the accessible parameter space was defined and the influence of the photo-diode noise floor on the accessible parameter space was discussed. It was shown that by minimizing the noise from the photo-diode, this technique would be able to resolve relaxation times below $1\mu s$. Viscous limitations on the VE-FSI theory for low frequency operation was discussed, but did not limit the technique since the whole reason for using the higher modes was to avoid heavily damped lower modes. Additionally, the expected influence of the viscous boundary, as one approaches the interface, on the accessible parameter space was discussed. It was argued that although the parameter space would decrease, the increased dissipative effect would improve the SNR, which would allow the higher modes to be utilized. In combination with VE-FSI theory, a maximum viscosity for the operating was determined to be $\eta_0=225Pa s$.

It has been shown that the VE-FSI theory and experimental procedure, in conjunction with the AFM platform, formed a viable basis for an interfacial rheology probe. The comparison of the bulk measurements for η_0 and λ showed correlation with other techniques and the scaling relations for polymer concentrations were shown to agree. Although limitations were identified, they were not insurmountable. The continued development of this technique will provide researchers with an additional tool for quantifying rheology in the interfacial regime.

Appendix A: Processing code used in IGOR with annotation for various macros and user-defined functions

```
#pragma rtGlobals=1          // Use modern global access method.
#include <Multi-peak fitting 1.3>
#include <Peak Functions>
#include <Global Fit>
#include <DSP Window Functions>

// This procedure is for loading data waves(thermal files from AFM / Chief computer) and processing them.
// There are several Macros accessible from the Macro menu....each contains a brief description at the beginning

// Typical Procedure
// 1) Load Waves
// 2) Break Waves into sections
// 3) Generate Force Curves (determine distance from surface)
// 4) Clean Files (removes deflection files in lieu of force curves)
// 5) RYAN_POST_PROCESSING
//     a) takes pull curve or raw data(just thermal) and fits to SHO then convert to Transfer Function
// 6) If SHO fit isn't good, Run justPSDfit to re-calculate fit
// the others are for user convenience and debugging

// This is a list of available user defined MACROS as of 3/10/04:
//Ryan_LoadEntirePull
//Ryan_BreakEntirePull
//Ryan_GenerateForceCurve
//Ryan_CleanFiles;Ryan_PSD
//Ryan_Post_Processing
//Ryan_JustPSDrootFit
//Ryan_Testing_Parameters
//Ryan_Modify_force_curves
//Ryan_dimensionless_squeeze
//Ryan_added_theory
//Ryan_VE_hydro
//Ryan_SHO_added
//Ryan_add_noise
//Ryan_bulk_viscometer
//Ryan_Save_Regen_Graph

// *****Macros that came with IGOR packages*****
//CreateFitSetupPanel
//UseCursors
//ZapFitAndResiduals
//RenameGroup
//RevisitGroup
//RunMeAfterManualFit
//PrintPeakParams
//RemovePeakPackage
```

```

// *****This is a list of available user defined FUNCTIONS as of 3/10/04:

// ExamplesExperimentLoader
// getstartscan
// getspikebin
// getfilterboxwidth
// get_SHO_FitWidth
// remove_spikes
// SHOampWhite
// SuperSHO
// RyanSHO
// RyanSHO_fluid_fitfunc
// square_wave
// triangle_wave
// ThermalkError
// computecantileverparameters
// computefitparameters
// convert_to_transfer
// comp_counter
// loophydro
// RH
// RH2
// mass_2fluid
// disp_2fluid
// RVH
// mass_Vfluid
// disp_Vfluid
// RVEH
// mass_LVEfluid
// disp_LVEfluid
// disp_LVEfluid_alt
// Ndisp_LVEfluid_alt
// SHO_modes_freq
// SHO_modes_spring

// *****functions that came with general IGOR package*****
// DoSaveGraphToFile
// MakeUniqueFolders
// WMCreateFitGlobals
// WMPF_DataFolderList
// FindGraphWithWave
// ReturnToOldDataSet
// fPrintPeakParams
// CheckPeakPackage

// This macro loads waves as expected from Chief / AFM and renames them appropriately
macro Ryan_LoadEntirePull(pull_name)
    String pull_name
    NewDataFolder/O/S root:entire_pull
    //LoadWave/J/D/N=$pull_name/K=0
    LoadWave/J/D/N=$pull_name/K=0/p=home pull_name
    killwaves $pull_name+"1"
    Redimension/N=10 $pull_name+"0"
    Duplicate/o $pull_name+"0" $pull_name+"_parameters"; killwaves $pull_name+"0"
    Duplicate/o $pull_name+"2" $pull_name+"_pull"; killwaves $pull_name+"2"
    Display $pull_name+"_pull"; showinfo

```

```

Printf "****Record x-coordinate values for Thermal Wave and Pull Wave****\r ****run BreakEntirePull
macro****\r"
End // End of Load Entire Pull Macro

```

```

// This macro allows one to enter points at which to break the pull curves in segments
// The macro then renames the appropriate segments
macro Ryan_BreakEntirePull(w,thermal_start0, thermal_end0, approach_end0, retract_end0)
string w
Prompt w "pull wave:",popup WaveList("",";","")
variable thermal_start0, thermal_end0, approach_end0, retract_end0
variable/G thermal_start, thermal_end, approach_end, retract_end
thermal_start=thermal_start0; thermal_end=thermal_end0; approach_end=approach_end0;
retract_end=retract_end0
duplicate/o/r=[thermal_start, thermal_end] $w, $w+"_Thermal_deflection"
duplicate/o/r=[thermal_end, approach_end] $w, $w+"_Approach_deflection"
duplicate/o/r=[approach_end, retract_end] $w, $w+"_Retract_deflection"
newdatafolder/O/S root:original_files
//changing string value ***BE CAREFUL***
variable namelen=strlen(w)
string w1=w[0,namelen-6]
duplicate/O root:entire_pull:$w1+"_pull_Thermal_deflection" $w1+"_Therm_def"
duplicate/O root:entire_pull:$w1+"_parameters" $w1+"_parameters"
SetScale/P x 0,$w1+"_parameters"[1],"seconds", $w1+"_Therm_def"
SetScale d 0,0,"Volt", $w1+"_Therm_def"
variable thermerror=$w1+"_parameters"[1]*abs($w1+"_parameters"[5]/$w1+"_parameters"[1]-
numpnpts($w1+"_Therm_def"))
variable approacherror=$w1+"_parameters"[1]*abs(1/2/$w1+"_parameters"[4]/$w1+"_parameters"[1]-
numpnpts(root:entire_pull:$w1+"_Approach_deflection"))
variable retracterror=$w1+"_parameters"[1]*abs(1/2/$w1+"_parameters"[4]/$w1+"_parameters"[1]-
numpnpts(root:entire_pull:$w1+"_Retract_deflection"))
Printf "Time error in Thermal Deflection Wave = %g\r", thermerror
Printf "Time error in Approach Wave = %g\r", approacherror
Printf "Time error in Retract Wave = %g\r", retracterror
Printf "****Run Ryan_GenerateForceCurve to verify Optical Lever Sensitivity and Compute
Height****\r"
End //end of break entire pull

// If processing a pull curve, this macro uses the the approach curve and retract curve
// It convert them into force curves so that the distance can be determine graphically
macro Ryan_GenerateForceCurve(w)
string w
//Prompt w "data wave:",popup WaveList("",";","")
NewDataFolder/O/S root:$w+"_processed"
duplicate/O root:entire_pull:$w+"_pull_Approach_deflection"
root:$w+"_processed":$w+"_pull_Approach_deflection"
duplicate/O root:entire_pull:$w+"_pull_Retract_deflection"
root:$w+"_processed":$w+"_pull_Retract_deflection"
SetScale/P x 0,root:entire_pull:$w+"_parameters"[1],"seconds", $w+"_pull_Approach_deflection"
$w+"_pull_Approach_deflection"*=root:entire_pull:$w+"_parameters"[2]*1e-9;SetScale d 0,0,"m",
$w+"_pull_Approach_deflection"
duplicate/O $w+"_pull_Approach_deflection" $w+"_Approach_dist"
$w+"_Approach_dist"*=x*root:entire_pull:$w+"_parameters"[6]*1e-6 //assume speed is in micron/second
SetScale d 0,0,"m", $w+"_Approach_dist"
duplicate/O $w+"_Approach_dist" $w+"_Approach_sep"
Display $w+"_pull_Approach_deflection" vs $w+"_Approach_dist"

```

```

showinfo
$w+"_Approach_sep"=$w+"_pull_Approach_deflection"; wavestats/Q $w+"_Approach_sep"
$w+"_Approach_sep"=V_max; $w+"_Approach_sep"*=-1
//Display $w+"_pull_Approach_deflection" vs $w+"_Approach_sep"
SetScale/P x 0,root:entire_pull:$w+"_parameters"[1],"seconds", $w+"_pull_Retract_deflection"
$w+"_pull_Retract_deflection"*=root:entire_pull:$w+"_parameters"[2]*1e-9;SetScale d 0,0,"m",
$w+"_pull_Retract_deflection"
duplicate/O $w+"_pull_Retract_deflection" $w+"_Retract_dist"
$w+"_Retract_dist"=x*root:entire_pull:$w+"_parameters"[6]*1e-6 //assume speed is in micron/second
SetScale d 0,0,"m", $w+"_Retract_dist"
duplicate/O $w+"_Retract_dist" $w+"_Retract_sep"
//Display $w+"_pull_Retract_deflection" vs $w+"_Retract_dist"
$w+"_Retract_sep"+= $w+"_pull_Retract_deflection"; wavestats/Q $w+"_Retract_sep"
$w+"_Approach_sep"=V_max; $w+"_Approach_sep"*=-1
//Display $w+"_pull_Retract_deflection" vs $w+"_Retract_sep"
Printf "****Check Slope on Contact region of Deflection vs Distance plot: \r"
Printf "          Change Optical Sensitivity Manually(2 param files) (current O.L.S. / approach
slope(~1)) and re-Run Macro****\r"
Printf "****After fixing Sensitivity, run clean files macro****\r"
Printf "****Run Ryan_PSD on Therm_def****\r"
end //end of macro Ryan_GenerateForceCurve

macro Ryan_adjustIOLS(w)
string w
Printf "original_files parameter file [2] = %g\r",root:original_files:$w+"_parameters"[2]
CurveFit line $w+"_pull_Approach_deflection"[pcsr(A),pcsr(B)] /X=$w+"_Approach_dist"
root:entire_pull:$w+"_parameters"[2]/=root:$w+"_processed":W_coef[1];root:original_files:$w+"_parameters"[2]/=root:$w+"_processed":W_coef[1]
//re-calculate deflection curves*****
NewDataFolder/O/S root:$w+"_processed"
duplicate/O root:entire_pull:$w+"_pull_Approach_deflection"
root:$w+"_processed":$w+"_pull_Approach_deflection"
duplicate/O root:entire_pull:$w+"_pull_Retract_deflection"
root:$w+"_processed":$w+"_pull_Retract_deflection"
SetScale/P x 0,root:entire_pull:$w+"_parameters"[1],"seconds", $w+"_pull_Approach_deflection"
$w+"_pull_Approach_deflection"*=root:entire_pull:$w+"_parameters"[2]*1e-9;SetScale d 0,0,"m",
$w+"_pull_Approach_deflection"
duplicate/O $w+"_pull_Approach_deflection" $w+"_Approach_dist"
$w+"_Approach_dist"=x*root:entire_pull:$w+"_parameters"[6]*1e-6 //assume speed is in micron/second
SetScale d 0,0,"m", $w+"_Approach_dist"
duplicate/O $w+"_Approach_dist" $w+"_Approach_sep"
//Display $w+"_pull_Approach_deflection" vs $w+"_Approach_dist"
//showinfo
$w+"_Approach_sep"=$w+"_pull_Approach_deflection"; wavestats/Q $w+"_Approach_sep"
$w+"_Approach_sep"=V_max; $w+"_Approach_sep"*=-1
//Display $w+"_pull_Approach_deflection" vs $w+"_Approach_sep"
SetScale/P x 0,root:entire_pull:$w+"_parameters"[1],"seconds", $w+"_pull_Retract_deflection"
$w+"_pull_Retract_deflection"*=root:entire_pull:$w+"_parameters"[2]*1e-9;SetScale d 0,0,"m",
$w+"_pull_Retract_deflection"
duplicate/O $w+"_pull_Retract_deflection" $w+"_Retract_dist"
$w+"_Retract_dist"=x*root:entire_pull:$w+"_parameters"[6]*1e-6 //assume speed is in micron/second
SetScale d 0,0,"m", $w+"_Retract_dist"
duplicate/O $w+"_Retract_dist" $w+"_Retract_sep"
//Display $w+"_pull_Retract_deflection" vs $w+"_Retract_dist"
$w+"_Retract_sep"+= $w+"_pull_Retract_deflection"; wavestats/Q $w+"_Retract_sep"
$w+"_Retract_sep"=V_max; $w+"_Retract_sep"*=-1

```

```

//Display $w+"_pull_Retract_deflection" vs $w+"_Retract_sep"
Printf "new parameter file [2] = %g\r",root:original_files:$w+"_parameters"[2]
end

// Removes deflection curves in lieu of the force curves
macro Ryan_CleanFiles(wave_to_clean)
string wave_to_clean
//Prompt wave_to_clean "data wave to clean:",popup WaveList("",";","")
//killwaves root:entire_pull:"wave_to_clean+"_parameters"
killwaves/z root:entire_pull:$wave_to_clean+"_pull_Retract_deflection"
killwaves/z root:entire_pull:$wave_to_clean+"_pull_Thermal_deflection"
killwaves/z root:entire_pull:$wave_to_clean+"_pull_Approach_deflection"
newdatafolder/O/S root:original_files
end // end of clean files macro

// Given a long data wave create a short result wave containing the Power
// Spectral Density. For the purposes of this macro, PSD is defined in
// terms of the power per frequency bin width. To get the total power you need
// to integrate. The signal is assumed to be a voltage measurement across a
// 1 ohm resistor.
// The name of the new wave is the name of the source + _psd
// This macro also creates a new deflection wave with a zero mean for computing the psd
Macro Ryan_PSD(w,modwave,seglen>window)
string w
Prompt w "data wave:",popup WaveList("",";","")
variable modwave=1
Prompt modwave, "use modified data with zeroed mean or actual data wave", popup "modified data
wave;actual data wave"
variable seglen=9
Prompt seglen,"segment length:",popup
"256;512;1024;2048;4096;8192;16384;32768;65536;131072;262144"
variable window=2
Prompt window, "Window type:",popup "Square;Hann;Parzen;Welch;Hamming;"
"BlackmanHarris3;KaiserBessel"

PauseUpdate; silent 1
variable npsd= 2^(7+seglen) // number of points in group (resultant psd)
wave len= npsd/2+1
variable psdOffset= npsd/2 // offset each group by this amount
variable psdFirst=0 // start of current group

if(modwave==1)
duplicate/O $w moddatawave
wavestats moddatawave
moddatawave=v_avg
$w=moddatawave
killwaves/z moddatawave
endif

variable nsrc= numpnts($w)
variable nsegs,winNorm // count of number of segments
and window normalization factor
variable namelen=strlen(w)
string w1=w[0,namelen-1]
//string w1=w[0,namelen-5] this line mysteriously appeared between versions of this procedure?****??
string destw=w1+"_psd_V2",srctmp=w1+"_tmp"

```

```

string winw=w1+"_psdWin" // window goes here
make/o/n=(npsd/2+1) $destw
make/o/n=(npsd) $srctmp,$swinw; $swinw= 1
if( window==1 )
    winNorm= 1
else
    if( window==2 )
        Hanning $swinw;winNorm=0.372 // winNorm is avg
squared value of Hanning function
    else
        if( window==3 )
            winNorm= Parzen($swinw)
        else
            if( window==4 )
                winNorm= Welch($swinw)
            else
                if( window==5 )
                    winNorm= Hamming($swinw)
                else
                    if( window==6 )
                        winNorm= BlackmanHarris3($swinw)
                    else
                        if( window==7 )
                            winNorm= KaiserBessel($swinw)
                        else
                            Abort "unknown window index"
                        endif
                    endif
                endif
            endif
        endif
    endif
endif
endif
//Duplicate/O/R=[0,npsd-1] $w $srctmp; $srctmp *= $swinw; fft $srctmp
//CopyScales/P $srctmp, $destw
//$srctmp*=2/npsd
//$destw= magsqr($srctmp)
//psdFirst= npsd
nsegs=0
if (psdFirst+npsd-1<nsrc)
    do
        Duplicate/O/R=[psdFirst,psdFirst+npsd-1] $w $srctmp; $srctmp *= $swinw
        fft $srctmp; CopyScales/P $srctmp, $destw; $srctmp*=2/npsd; $destw +=
magsqr($srctmp); psdFirst += npsd; nsegs+=1
        while( psdFirst+npsd < nsrc )
            else
                Abort "Data wave shorter than requested segment length"
            endif
        printf "%g PSD data segments averaged\r", nsegs
        winNorm= 1/deltax($destw)/(winNorm*nsegs); $destw *= winNorm
        $destw[0] /= 4
        KillWaves $srctmp,$swinw
        SetScale d 0,0,"Volt^2/Hz", $w1+"_psd_V2"
        Printf "****Run Ryan_Post_Processing on *_psd to compute m,b,k parameters****\r"
end // macro for psd

```

```

// Takes pull data or raw thermal data and converts to PSD
// Removes video monitor spikes and smooths with running box average
// Fits to SHOampWhite
// Computes Thermal and Cantilever Parameters
// Converts to Transfer Function
macro Ryan_Post_Processing(name_wave, pull_flag)
  string name_wave
  variable pull_flag=0
  Prompt pull_flag,"Use data from pull wave or data from raw file:",popup "Use Pull Wave;Use Raw File"
  if (pull_flag==2)
    NewDataFolder/O/S root:original_files
    //LoadWave/J/D/N=$name_wave/K=0
    //LoadWave/J/D/N=$pull_name/K=0
    LoadWave/J/D/N=$name_wave/K=0/p=home name_wave
    Redimension/N=10 $name_wave+"0"
    Redimension/N=(1/$name_wave+"0"[0]/$name_wave+"0"[1]/2) $name_wave+"1"
    Duplicate/O $name_wave+"0" $name_wave+"_parameters"
    Duplicate/O $name_wave+"1" $name_wave+"_psd_V2"
    Duplicate/O $name_wave+"2" $name_wave+"_Therm_def"
    KillWaves $name_wave+"0" $name_wave+"1" $name_wave+"2"
    SetScale/P x 0,$name_wave+"_parameters"[0],"Hz", $name_wave+"_psd_V2" // change wave
scalings and add units
    SetScale d 0,0,"Volt^2/Hz", $name_wave+"_psd_V2"
    SetScale/P x 0,$name_wave+"_parameters"[1],"seconds", $name_wave+"_Therm_def"
    SetScale d 0,0,"Volt", $name_wave+"_Therm_def"
  endif
  NewDataFolder/O/S root:$name_wave+"_processed"
  Duplicate/O root:original_files:$name_wave+"_psd_V2" $name_wave+"_psd_m2"
  $name_wave+"_psd_m2"*=root:original_files:$name_wave+"_parameters"[2]^2*1e-18
  SetScale d 0,0,"m^2/Hz", $name_wave+"_psd_m2"
  Duplicate/O $name_wave+"_psd_m2" $name_wave+"_raw_psd_m2"
  killwaves $name_wave+"_psd_m2"
  duplicate/O $name_wave+"_raw_psd_m2" $name_wave+"_psd_m"
  $name_wave+"_psd_m"=sqrt($name_wave+"_raw_psd_m2")
  SetScale d 0,0,"m/sqrt(Hz)", $name_wave+"_psd_m"
  Display $name_wave+"_psd_m"; ModifyGraph log(left)=1; ModifyGraph log(bottom)=1; ModifyGraph
tickunit(left)=1; Label Left "\u"
  showinfo
  // Clean up psd plots by removing spikes and using sliding box filter
  variable/G startscan=getstartscan(), spikebin=getspikebin()
  remove_spikes($name_wave+"_psd_m", startscan, spikebin,
root:original_files:$name_wave+"_parameters")
  variable/G filterboxwidth=getfilterboxwidth()
  Smooth/B filterboxwidth, $name_wave+"_psd_m"
  Duplicate/O $name_wave+"_psd_m" Fitwave
  Fitwave:=SHOampWhite(SHOparm, x)
  AppendToGraph Fitwave
  FitWidth=get_SHO_FitWidth(FitWidth)
  if (FitWidth==0) //if fitwidth=0
then use the whole wave
    FuncFit SHOampWhite SHOparm $name_wave+"_psd_m" //full width fit, no frills
  else
    if ((ResFreq-FitWidth/2)<startscan)
      FuncFit SHOampWhite SHOparm
$name_wave+"_psd_m"(startscan,ResFrcq+(FitWidth/2)) //limits the lower side of the fit if frequency
is low

```

```

// sometimes the macro will
stop with a singular error, which is usually due to the ResFreq = 0
    else
        FuncFit SHOampWhite SHOparm $name_wave+"_psd_m"(ResFreq-
(FitWidth/2),ResFreq+(FitWidth/2)) //does the fit within the fit width
    endif
endif
SHOparm=abs(SHOparm)
ThermalDC=SHOparm[0] //sets the SHO fit
parameters to displayed values
ThermalQ=SHOparm[1]
ResFreq=SHOparm[2]
SHOparm[3]/=1000
WhiteNoise=SHOparm[3]
make/o/n=3 ThermalK
variable/G Boltzman=1.38e-23
ThermalKError(SHOparm, W_sigma, ThermalK, Boltzman, Temperature)
computecantileverparameters(ThermalK[0], ResFreq, ThermalQ)
Duplicate/O $name_wave+"_psd_m" $name_wave+"_mag_Transfer_Function"
convert_to_transfer($name_wave+"_mag_Transfer_Function", ResFreq, ThermalQ, ThermalK[0],
Boltzman, Temperature)
SetScale d 0,0,"m/N", $name_wave+"_mag_Transfer_Function"
Duplicate/O Fitwave $name_wave+"Fit_mag_TF"
convert_to_transfer($name_wave+"Fit_mag_TF", ResFreq, ThermalQ, ThermalK[0], Boltzman,
Temperature)
SetScale d 0,0,"m/N", $name_wave+"Fit_mag_TF"
Display $name_wave+"_mag_Transfer_Function"; ModifyGraph log(left)=1; ModifyGraph
log(bottom)=1; ModifyGraph tickunit(left)=1; Label Left "\u"
Printf "*****Run Ryan_JustPSDrootFit if Fit wave is NOT correct*****\r"
end // end of Post_Processing macro

// Use this macro if the PSD fit isn't good
// before running this macro, set all new guess value and fitwidth
macro Ryan_JustPSDrootFit(name_wave,pull_flag,use_cursor)
    string name_wave
    variable pull_flag=1
    Prompt pull_flag,"Redo fit or use SHOparm from independent fit",popup "Redo;Use SHOparm file"
    variable use_cursor=1
    Prompt use_cursor,"use cursors on graph or FitWidth",popup "cursors;FitWidth"
    if (pull_flag==1)
        If (use_cursor==2)
            if (FitWidth==0)
                //if fitwidth=0 then use the whole wave
                FuncFit SHOampWhite SHOparm $name_wave+"_psd_m" //full
width fit, no frills
                //FuncFit/H="0001" SHOampWhite SHOparm
$name_wave+"_psd_m"[pcsr(A),pcsr(B)] /D=Fitwave
                else
                    if ((ResFreq-FitWidth/2)<startscan)
                        FuncFit SHOampWhite SHOparm
$name_wave+"_psd_m"(startscan,ResFreq+(FitWidth/2)) //limits the lower side of the fit if frequency
is low
                    else
                        FuncFit SHOampWhite SHOparm $name_wave+"_psd_m"(ResFreq-
(FitWidth/2),ResFreq+(FitWidth/2)) //does the fit within the fit width
                    endif
                endif
            endif
        endif
    endif
end

```



```

endif
else
FuncFit/H="0001" SHOampWhite SHOparm $name_wave+"_psd_m"[pcsr(A),pcsr(B)]
/D=Fitwave
endif
endif
SHOparm=abs(SHOparm)
ThermalDC=SHOparm[0] //sets the SHO fit
parameters to displayed values
ThermalQ=SHOparm[1]
ResFreq=SHOparm[2]
SHOparm[3]/=1000
WhiteNoise=SHOparm[3]
make/o/n=3 ThermalK
variable/G Boltzman=1.38e-23
ThermalkError(SHOparm, W_sigma, ThermalK, Boltzman, Temperature)
computeantileverparameters(ThermalK[0], ResFreq, ThermalQ)
Duplicate/O $name_wave+"_psd_m" $name_wave+"_mag_Transfer_Function"
convert_to_transfer($name_wave+"_mag_Transfer_Function", ResFreq, ThermalQ, ThermalK[0],
Boltzman, Temperature)
SetScale d 0,0,"m/N", $name_wave+"_mag_Transfer_Function"
Duplicate/O Fitwave $name_wave+"_Fit_mag_TF"
convert_to_transfer($name_wave+"_Fit_mag_TF", ResFreq, ThermalQ, ThermalK[0], Boltzman,
Temperature)
SetScale d 0,0,"m/N", $name_wave+"_Fit_mag_TF"
//Display $name_wave+"_mag_Transfer_Function"; ModifyGraph log(left)=1; ModifyGraph
log(bottom)=1; ModifyGraph tickunit(left)=1; Label Left "\u"
end // end JustPSDrootFit Macro

// *****End of Main Macros*****Beginning of Function Definitions*****
function getstartscan()
Variable tempstartscan=1000
Prompt tempstartscan,"enter frequency to start scan (Hz), just past 1/f noise"
DoPrompt "refer to plot of psd", tempstartscan
return tempstartscan
end
function getspikebin()
Variable tempspikebin=500
Prompt tempspikebin, "enter bandwidth of spikes to be filtered"
DoPrompt "Enter bandwidth", tempspikebin
return tempspikebin
end
function getfilterboxwidth()
Variable tempfilterboxwidth=10
Prompt tempfilterboxwidth, "enter box width for sliding filter"
DoPrompt "Enter filter", tempfilterboxwidth
return tempfilterboxwidth
end
function get_SHO_FitWidth(tempfitwidth)
Variable tempfitwidth=tempfitwidth //units in Hz, and center on Resonant Frequency
Prompt tempfitwidth, "enter width about resonant frequency to fit SHOampWhite"
DoPrompt "Enter SHOWampWhite FitWidth", tempfitwidth
return tempfitwidth
end
function remove_spikes(psdwave,startscan, spikebin, parmwave)
wave psdwave

```

```

variable startscan, spikebin
wave parmwave
variable count, binsize, F0, F0amp, amplitude_threshold
variable/G dc_value, samplerate, df, OpticalLeverSens, Temperature
count=0
binsize=1000 //size of bin that crawls throught psd with units of Hz
samplerate= 1/parmwave[1]
df = parmwave[0]
OpticalLeverSens=parmwave[2]
Temperature=parmwave[3]
variable/G PullFrequency=parmwave[4]
variable/G ThermalDelayTime=parmwave[5]
variable/G PullSpeed=parmwave[6]
wavestats/q/r=(startscan, startscan+1000) psdwave
dc_value=v_avg
amplitude_threshold=5 // multiple of binsize average that determines spike
make/o/d/n=(samplerate/2/binsize) crawler
do
    if (startscan<=count*binsize)
        wavestats/Q/R=((count*binsize),(count*binsize+binsize)) psdwave
        crawler[count]=v_avg
        F0=v_maxloc
        F0amp=v_max
        wavestats/q/r=((F0-spikebin/2),(F0+spikebin/2)) psdwave
        if (v_avg*1.4<F0amp)
            if (v_max>crawler[count]*amplitude_threshold) //if true then this is a spike
                psdwave[x2pnt(psdwave,F0-
spikebin/2),x2pnt(psdwave,F0+spikebin/2)]=psdwave(F0-spikebin/2)
                crawler[count]=crawler[count-1]
            endif
        endif
    else
        crawler[count]=dc_value
//
//
        psdwave[x2pnt(psdwave,count*binsize),x2pnt(psdwave,count*binsize+binsize)]=dc_value
// texted out the above code...it used to set psdwave values below the startscan=dc_value. Eliminated this so that
// I can still see original wave, and modified FuncFit to limit lower value to startscan value
        endif
        count+=1
        while (count<(samplerate/2/binsize))
            WaveStats/Q crawler
            variable maxfreqbin=v_maxloc
            WaveStats/Q/R=((maxfreqbin*binsize),(maxfreqbin*binsize+binsize)) psdwave
            variable/G Freq0=v_maxloc

            If (Freq0==Inf) //if the
F0 is too high assumes the Q is 1.5
                Freq0=2500
            endif
            If (Freq0<10) //if the
F0 is NaN assumes the Q is 1.5
                Freq0=2500
            endif

            WaveStats/Q/R=((Freq0-70),(Freq0+70)) psdwave
            variable/G Freq0amp=v_avg

```

```

    FindLevel/Q/B=1/R=(Freq0,Freq0+5000) psdwave,(Freq0amp*.707)
    variable F2=V_LevelX //finds the width
of the peak at sqrt2/2 of max peak
    FindLevel/Q/B=1/R=(Freq0,Freq0-5000) psdwave,(Freq0amp*.707)
    variable F1=V_LevelX
    variable/G Qual=Freq0/(F2-F1) //divides the max
amp freq by the width to get the Q
    If (Qual==Inf) //if the
F0 is too high assumes the Q is 1.5
        Qual=1.5
    endif
    If (Qual*0!=0) //if the
F0 is NaN assumes the Q is 1.5
        Qual=1.5
    endif
    wavestats /Q/R=((Freq0-5100),(Freq0-4900)) psdwave //gets the average for 5 kHz below
the resonance
    variable LowAmp=dc_value //figures
out the base level for the white noise estimate
    wavestats /Q/R=((Freq0+4900),(Freq0+5100)) psdwave //gets the average for 5 kHz above
the resonance
    variable HiAmp=v_avg
    if (Freq0<5200)
    //if the peak is too low then LowAmp doesn't exist
        LowAmp=HiAmp
    //set the low amp equal to the high amp
    endif
    variable amp=freq0amp/Qual //figures out the
DC level by dividing the max amp by Q
    Make/N=4/D/O SHOparm //makes the
parameter wave for the SHO fit
    SHOparm[0]=dc_value //amp
    //the ThermalDC
    SHOparm[1]=Qual //the
ThermalQ
    SHOparm[2]=Freq0
    //the ResFreq
    SHOparm[3]=LowAmp //(HiAmp+LowAmp)/2 //the
average of the two is the WhiteNoise
    Variable /G ThermalDC,ThermalQ,ResFreq,WhiteNoise,FitWidth //makes the fit variables
    ThermalDC=SHOparm[0] //sets the SHO fit
parameters to displayed values
    ThermalQ=SHOparm[1]
    ResFreq=SHOparm[2]
    WhiteNoise=SHOparm[3]
    FitWidth=8000
    //sets the fit width
    if (Qual<2)
        FitWidth=16000 //Low Q
needs more width
    endif
    return psdwave
end //remove_spikes

Function SHOampWhite(w,x) : FitFunc
Wave w

```

Variable x

```
//CurveFitDialog/ These comments were created by the Curve Fitting dialog. Altering them will
//CurveFitDialog/ make the function less convenient to work with in the Curve Fitting dialog.
//CurveFitDialog/ Equation:
//CurveFitDialog/ //Amplitude response for a SHO. "Vibration and Waves" p. 89
//CurveFitDialog/ //w[0] = Amplitude at DC
//CurveFitDialog/ //w[1] = Q
//CurveFitDialog/ //w[2] = omega0, in either radians or Hz
//CurveFitDialog/ //w[3] = white noise. Units are m/rHz
//CurveFitDialog/ //x is the variable omega
//CurveFitDialog/ variable RedFreq
//CurveFitDialog/ RedFreq = x/w_2
//CurveFitDialog/ f(x) = (Sqrt((w_0/RedFreq)^2/ ((1/RedFreq - RedFreq)^2 + 1/w_1^2) + w_3^2 ))
//CurveFitDialog/ End of Equation
//CurveFitDialog/ Independent Variables 1
//CurveFitDialog/ x
//CurveFitDialog/ Coefficients 4
//CurveFitDialog/ w[0] = w_0
//CurveFitDialog/ w[1] = w_1
//CurveFitDialog/ w[2] = w_2
//CurveFitDialog/ w[3] = w_3

//Amplitude response for a SHO. "Vibration and Waves" p. 89
//w[0] = Amplitude at DC
//w[1] = Q
//w[2] = omega0, in either radians or Hz
//w[3] = white noise. Units are m/rHz
//x is the variable omega
variable RedFreq
RedFreq = x/w[2]
return (Sqrt((w[0]/RedFreq)^2/ ((1/RedFreq - RedFreq)^2 + 1/w[1]^2) + w[3]^2 ))
```

End

function SuperSHO(w,x) : FitFunc

```
wave w
variable x
//w[0,4,8,12] = Amplitude at DC: 1/k
//w[1,5,9,13] = Quality: Q
//w[2,6,10,14] = omega0, in either radians or Hz
//w[3,7,11,15] = white noise. Units are m/rHz
//x is the variable omega
variable RedFreq1
RedFreq1 = x/w[2]
variable mode1=((w[0]/RedFreq1)^2/ ((1/RedFreq1 - RedFreq1)^2 + 1/w[1]^2) + w[3]^2 ))
variable RedFreq2
RedFreq2 = x/w[6]
variable mode2=((w[4]/RedFreq2)^2/ ((1/RedFreq2 - RedFreq2)^2 + 1/w[5]^2) + w[7]^2 ))
variable RedFreq3
RedFreq3 = x/w[10]
variable mode3=((w[8]/RedFreq3)^2/ ((1/RedFreq3 - RedFreq3)^2 + 1/w[9]^2) + w[11]^2 ))
variable RedFreq4
RedFreq4 = x/w[14]
variable mode4=((w[12]/RedFreq4)^2/ ((1/RedFreq4 - RedFreq4)^2 + 1/w[13]^2) + w[15]^2 ))
return sqrt(mode1+mode2+mode3+mode4) // note: PSDs add
```

end // end of SuperSHO

//SHO transfer function with complex values and mass, damping and stiffness
function RyanSHO(w,f,add_flag,density,width,viscosity,relax,length,cc,bb) : FitFunc

```
    wave w
    variable f
    variable add_flag
    variable density//=root:original_files:fluid_density
    variable width//=root:original_files:cantilever_width
    variable viscosity//=root:original_files:fluid_viscosity
    variable relax//=root:original_files:relaxation_time
    variable length//=root:original_files:cantilever_length
    variable cc
    variable bb
    //parameter wave can be used to fit air response m,b,k....density, viscosity, etc. are independent variables
    //w[0,3,6,9]=m0,m1,m2,m3
    //w[1,4,7,10]=b0,b1,b2,b3
    //w[2,5,8,11]=k0,k1,k2,k3
    //
    //variable cc=.12 //mass correction factor for the fact that theory is for infinite cylinder and we have a
cantilevered beam
    //variable bb=.12 //damping correction factor for the fact that theory is for infinite cylinder and we have a
cantilevered beam
    variable/c CTR0=0,CTR1=0,CTR2=0,CTR3=0
    if(add_flag==1)
        CTR0=1/(
(w[0]+cc*mass_2fluid(f,density,width,viscosity,length))*(2*pi*f*cmplx(0,1))*(2*pi*f*cmplx(0,1))+(w[1]+bb*disp
_2fluid(f,density,width,viscosity,length))*(2*pi*f*cmplx(0,1))+w[2] )
        CTR1=1/(
(w[3]+cc*mass_2fluid(f,density,width,viscosity,length))*(2*pi*f*cmplx(0,1))*(2*pi*f*cmplx(0,1))+(w[4]+bb*disp
_2fluid(f,density,width,viscosity,length))*(2*pi*f*cmplx(0,1))+w[5] )
        CTR2=1/(
(w[6]+cc*mass_2fluid(f,density,width,viscosity,length))*(2*pi*f*cmplx(0,1))*(2*pi*f*cmplx(0,1))+(w[7]+bb*disp
_2fluid(f,density,width,viscosity,length))*(2*pi*f*cmplx(0,1))+w[8] )
        CTR3=1/(
(w[9]+cc*mass_2fluid(f,density,width,viscosity,length))*(2*pi*f*cmplx(0,1))*(2*pi*f*cmplx(0,1))+(w[10]+bb*dis
p_2fluid(f,density,width,viscosity,length))*(2*pi*f*cmplx(0,1))+w[11] )
        elseif(add_flag==2)
            CTR0=1/(
(w[0]+cc*mass_Vfluid(f,density,width,viscosity,relax,length))*(2*pi*f*cmplx(0,1))*(2*pi*f*cmplx(0,1))+(w[1]+b
b*disp_Vfluid(f,density,width,viscosity,relax,length))*(2*pi*f*cmplx(0,1))+w[2] )
            CTR1=1/(
(w[3]+cc*mass_Vfluid(f,density,width,viscosity,relax,length))*(2*pi*f*cmplx(0,1))*(2*pi*f*cmplx(0,1))+(w[4]+b
b*disp_Vfluid(f,density,width,viscosity,relax,length))*(2*pi*f*cmplx(0,1))+w[5] )
            CTR2=1/(
(w[6]+cc*mass_Vfluid(f,density,width,viscosity,relax,length))*(2*pi*f*cmplx(0,1))*(2*pi*f*cmplx(0,1))+(w[7]+b
b*disp_Vfluid(f,density,width,viscosity,relax,length))*(2*pi*f*cmplx(0,1))+w[8] )
            CTR3=1/(
(w[9]+cc*mass_Vfluid(f,density,width,viscosity,relax,length))*(2*pi*f*cmplx(0,1))*(2*pi*f*cmplx(0,1))+(w[10]+
bb*disp_Vfluid(f,density,width,viscosity,relax,length))*(2*pi*f*cmplx(0,1))+w[11] )
            elseif(add_flag==3)
                CTR0=1/(
(w[0]+cc*mass_LVEfluid(f,density,width,viscosity,relax,length))*(2*pi*f*cmplx(0,1))*(2*pi*f*cmplx(0,1))+(w[1]
+bb*disp_LVEfluid(f,density,width,viscosity,relax,length))*(2*pi*f*cmplx(0,1))+w[2] )
```

```

        CTR1=1/(
(w[3]+cc*mass_LVEfluid(f,density,width,viscosity,relax,length))*(2*pi*f*cmplx(0,1))*(2*pi*f*cmplx(0,1))+(w[4]
+bb*disp_LVEfluid(f,density,width,viscosity,relax,length))*(2*pi*f*cmplx(0,1))+w[5] )
        CTR2=1/(
(w[6]+cc*mass_LVEfluid(f,density,width,viscosity,relax,length))*(2*pi*f*cmplx(0,1))*(2*pi*f*cmplx(0,1))+(w[7]
+bb*disp_LVEfluid(f,density,width,viscosity,relax,length))*(2*pi*f*cmplx(0,1))+w[8] )
        CTR3=1/(
(w[9]+cc*mass_LVEfluid(f,density,width,viscosity,relax,length))*(2*pi*f*cmplx(0,1))*(2*pi*f*cmplx(0,1))+(w[10]
+bb*disp_LVEfluid(f,density,width,viscosity,relax,length))*(2*pi*f*cmplx(0,1))+w[11] )
        elseif(add_flag==4)
            CTR0=1/(
(w[0]+cc*mass_LVEfluid(f,density,width,viscosity,relax,length))*(2*pi*f*cmplx(0,1))*(2*pi*f*cmplx(0,1))+(w[1]
+bb*disp_LVEfluid_alt(f,density,width,viscosity,relax,length))*(2*pi*f*cmplx(0,1))+w[2] )
            CTR1=1/(
(w[3]+cc*mass_LVEfluid(f,density,width,viscosity,relax,length))*(2*pi*f*cmplx(0,1))*(2*pi*f*cmplx(0,1))+(w[4]
+bb*disp_LVEfluid_alt(f,density,width,viscosity,relax,length))*(2*pi*f*cmplx(0,1))+w[5] )
            CTR2=1/(
(w[6]+cc*mass_LVEfluid(f,density,width,viscosity,relax,length))*(2*pi*f*cmplx(0,1))*(2*pi*f*cmplx(0,1))+(w[7]
+bb*disp_LVEfluid_alt(f,density,width,viscosity,relax,length))*(2*pi*f*cmplx(0,1))+w[8] )
            CTR3=1/(
(w[9]+cc*mass_LVEfluid(f,density,width,viscosity,relax,length))*(2*pi*f*cmplx(0,1))*(2*pi*f*cmplx(0,1))+(w[10]
+bb*disp_LVEfluid_alt(f,density,width,viscosity,relax,length))*(2*pi*f*cmplx(0,1))+w[11] )
        else
            CTR0=1/( w[0]*(2*pi*f*cmplx(0,1))*(2*pi*f*cmplx(0,1))+w[1]*(2*pi*f*cmplx(0,1))+w[2] )
            CTR1=1/( w[3]*(2*pi*f*cmplx(0,1))*(2*pi*f*cmplx(0,1))+w[4]*(2*pi*f*cmplx(0,1))+w[5] )
            CTR2=1/( w[6]*(2*pi*f*cmplx(0,1))*(2*pi*f*cmplx(0,1))+w[7]*(2*pi*f*cmplx(0,1))+w[8] )
            CTR3=1/( w[9]*(2*pi*f*cmplx(0,1))*(2*pi*f*cmplx(0,1))+w[10]*(2*pi*f*cmplx(0,1))+w[11] )
        endif
        variable tempTF=magsqr(CTR0)+magsqr(CTR1)+magsqr(CTR2)+magsqr(CTR3)
        return tempTF
end // RyanSHO

```

//SHO transfer function with complex values and mass, damping and stiffness

function RyanSHO_fluid_fitfunc(w,f) : FitFunc

wave w //12 SHO_coef_air values, fluid parameters: density, viscosity, relax cantilever parm: length,

width

variable f // frequency

//used to fit added terms and determine density, viscosity and relax
//w[0] through w[11] are the SHO_coef_air values for m0,b0,k0,m1,b1,k1...k3
//w[12]=density
//w[13]=viscosity
//w[14]=relaxation time
//w[15]=length of cantilever
//w[16]=width of cantilever

variable cc=.18 //correction factor for the fact that theory is for infinite cylinder and we have a cantilevered beam

variable/c CTR0=0,CTR1=0,CTR2=0,CTR3=0

CTR0=1/(

(w[0]+cc*mass_LVEfluid(f,w[12],w[16],w[13],w[14],w[15]))*(2*pi*f*cmplx(0,1))*(2*pi*f*cmplx(0,1))+(w[1]+cc*disp_LVEfluid(f,w[12],w[16],w[13],w[14],w[15]))*(2*pi*f*cmplx(0,1))+w[2])

CTR1=1/(

(w[3]+cc*mass_LVEfluid(f,w[12],w[16],w[13],w[14],w[15]))*(2*pi*f*cmplx(0,1))*(2*pi*f*cmplx(0,1))+(w[4]+cc*disp_LVEfluid(f,w[12],w[16],w[13],w[14],w[15]))*(2*pi*f*cmplx(0,1))+w[5])

```

        CTR2=1/(
(w[6]+cc*mass_LVEfluid(f,w[12],w[16],w[13],w[14],w[15]))*(2*pi*f*cmplx(0,1))*(2*pi*f*cmplx(0,1))+(w[7]+cc
*disp_LVEfluid(f,w[12],w[16],w[13],w[14],w[15]))*(2*pi*f*cmplx(0,1))+w[8] )
        CTR3=1/(
(w[9]+cc*mass_LVEfluid(f,w[12],w[16],w[13],w[14],w[15]))*(2*pi*f*cmplx(0,1))*(2*pi*f*cmplx(0,1))+(w[10]+c
c*disp_LVEfluid(f,w[12],w[16],w[13],w[14],w[15]))*(2*pi*f*cmplx(0,1))+w[11] )

        variable tempTF=magsqr(CTR0)+magsqr(CTR1)+magsqr(CTR2)+magsqr(CTR3)
        return sqrt(tempTF)
end // RyanSHO

// function for fitting a square wave. This was originally used in fitting the friction force traces
// However, it is usefull for any square wave trace
Function square_wave(w,x) : FitFunc
    Wave w
    Variable x
    //w[0]=lambda    with units in x-axis terms
    //w[1]=amplitude    units in y-axis
    //w[2]=shift    x-axis
    //w[3]=shift    y-axis
    variable count=0
    variable j=0
    for(j=1;j<=10;j+=1)
        count+=sinc(j*pi/2)*cos(j*2*pi*(x-w[2])/w[0])
        // condition;update loop variables
    endfor
    execute body code until continue test is false
    return w[1]*2*count+w[3]
End
// this function fits a triangle wave. Again, this was used for calibration the torsional displacement in FFM.
// this function is generated by combining sawtooth waves ( a built-in function)
Function triangle_wave(stparm,x): FitFunc
    wave stparm
    variable x
    // stparm[0] = amplitude
    // stparm[1] = frequency
    // stparm[2] = y shift
    // stparm[3] = x shift
    return stparm[2]+stparm[0]*((sawtooth((x-stparm[3])*stparm[1]/2/pi)-sawtooth(((x-stparm[3])-
20/stparm[1])*stparm[1]/2/pi))*2*sawtooth((x-stparm[3])*stparm[1]/2/pi*2)+(sawtooth(((x-stparm[3])-
20/stparm[1])*stparm[1]/2/pi)-sawtooth(((x-stparm[3]))*stparm[1]/2/pi)))
end

function ThermalkError(Coefs, Sigma, OutputWave, Boltzman, Temperature)
    wave Coefs, Sigma, OutputWave
    variable Boltzman, Temperature
    //This returns the same thermal spring constant as Thermalk, but uses the errors on the fit
    //returned by Igor to estimate the error in the spring constant.
    //OutputWave[0] contains the thermal k value
    //OutputWave[1] contains the maximum negative error from the individual errors in Adc, Q, and omega0
    //OutputWave[2] contains the maximum positive error
    variable ErrorSign0, ErrorSign1, ErrorSign2, MaxPosError, MaxNegError, i, Adc, Q, nu0, error
    Adc = Coefs[0]
    Q = abs(Coefs[1])
    nu0 = Coefs[2]
    OutputWave[0] = 2*Boltzman*Temperature/(Pi*nu0*Q*Adc^2)

```

```

ErrorSign0 = -1          //These will be used for adding or subtracting the errors
ErrorSign1 = -1
ErrorSign2 = -1
MaxPosError = 0
MaxNegError = 0
i = 0
do
    ErrorSign0 = 2*mod(i,2) -1
    ErrorSign1 = 2*trunc(mod(i,4)/2)-1
    ErrorSign2 = 2*trunc(mod(i,8)/4) - 1
    //print i, ErrorSign2, ErrorSign1, ErrorSign0
    //Enable this print statement to see how the above runs through all the possible combinations of
the
    //signs of the errors for Adc, Q, and nu0.
    Adc = Coefs[0]
    Q =abs(Coefs[1])
    nu0 = Coefs[2]
    Adc += ErrorSign0*Sigma[0]
    Q += ErrorSign1*Sigma[1]
    nu0 += ErrorSign2*Sigma[2]
    error = 2*Boltzman*Temperature/(Pi*nu0*Q*Adc^2) - OutputWave[0]
    //printf "%+0.0d%+0.0d%+0.0d%+3.3fv", ErrorSign2, ErrorSign1, ErrorSign0, error
    if (error>MaxPosError)
        MaxPosError = error
    endif
    if (error<MaxNegError)
        MaxNegError = error
    endif
    i +=1
while(i<8)
OutPutWave[1] = MaxNegError
OutPutWave[2] = MaxPosError
Printf "ThermalK=%g +/- %g/%g\r", OutPutWave[0], OutPutWave[2], OutPutWave[1]
return(nan)
end //ThermalkError

// enter values for spring constant, resonant frequency, and quality.....returns m,b,k parameters
Function computecantileverparameters(tspringk, tfoc, tQc)
    variable tspringk, tfoc, tQc
    variable tmasc, tdampb
    tmasc=tspringk/(2*pi*tfoc)^2
    tdampb=sqrt(tmasc*tspringk)/tQc
    variable/G ThermalMass=tmasc, ThermalDamp=tdampb, ThermalSpringC=tspringk
    Printf "spring constant = %g\r", tspringk
    Printf "mass of cantilver = %g\r", tmasc
    Printf "damping coefficient = %g\r", tdampb
    Printf "Quality = %g\r", tQc
    Printf "Resonant Frequency = %g\r", tfoc
end
Function computefitparameters(m,b,k)
    variable m,b,k
    variable DC, F0, Q
    DC=1/k
    F0=1/(2*pi)*sqrt(k/m)
    Q=sqrt(k*m)/b
    Printf "mass of cantilver = %g\r", m

```



```

Printf "damping coefficient = %g\r", b
Printf "spring constant = %g\r", k
Printf "DC value = %g\r", DC
Printf "Resonant Frequency = %g\r", F0
Printf "Quality = %g\r", Q
end
Function convert_to_transfer(psdroot, foc, Qc, springk, boltz, temperature)
wave psdroot
variable foc, Qc, springk, boltz, temperature
wave temp
psdroot = psdroot*sqrt((2*pi*foc*Qc/springk)/(4*boltz*temperature))
return psdroot
end

// Macro for entering testing parameters. This Macro is needed for most of the force curve macros because
// the fluid viscosity and tip height are required.
macro Ryan_Fluid_Parameters(f_name, f_viscosity, f_density, relaxation_t)
string f_name="name of fluid used in testing"
variable f_viscosity=.001
Prompt f_viscosity, "VISCOSITY of fluid: Pa*sec:"
variable f_density=1000
Prompt f_density, "DENSITY of fluid: Kg/m^3:"
variable relaxation_t=1e-10
Prompt relaxation_t, "Fluid Relaxation Time: sec:"
newdatafolder/O/S root:original_files
string/G fluid_name=f_name
variable/G fluid_viscosity=f_viscosity
variable/G fluid_density=f_density
variable/G relaxation_time=relaxation_t

end // end of macro for entering fluid values
macro
Ryan_Testing_Parameters(tp_height, can_width, can_length, can_thick, can_modulus, can_density, can_angle, s_const)
variable tp_height=3e-6
Prompt tp_height, "HEIGHT of tip: METERS:"
variable can_width=20e-6
Prompt can_width, "WIDTH of Cantilever: METERS:"
variable can_length=200e-6
Prompt can_length, "LENGTH of Cantilever: METERS:"
variable can_thick=.6e-6
Prompt can_thick, "Thickness of Cantilever: METERS:"
variable can_modulus=1.5e11
Prompt can_modulus, "Elastic Modulus of Cantilever: Pa"
variable can_density=2330
Prompt can_density, "Density of Cantilever: Kg/m^3"
variable can_angle=0
Prompt can_angle, "holder ANGLE of Cantilever: RADIANS:"
variable s_const=0
Prompt s_const, "Bulk SPRING CONSTANT: N/m:"
newdatafolder/O/S root:original_files
variable/G tip_height=tp_height
variable/G cantilever_width=can_width
variable/G cantilever_length=can_length
variable/G cantilever_thickness=can_thick
variable/G cantilever_modulus=can_modulus
variable/G cantilever_density=can_density

```

```

        variable/G cantilever_angle=can_angle
        variable/G bulk_spring_const=s_const

end // end of macro for entering fluid values

// Macro for turning approach curves into actual force curves. It PERMANENTLY MODIFIES the waves
// when it zeroes the vertical deflection and shifts for tip height. This is really not a concerning act, since
// the vertical displacement is somewhat arbitrary since it depends on the voltage at time of acquisition.
// The shift for contact is just adding the tip height.
// Place cursor A on contact region to enter present contact value
// Place cursor B on farthest point to record height in Height variable
Macro Ryan_display_FC(w)
    string w
    setdatafolder root:$w+"_processed"
    display $w+"_pull_Approach_deflection" vs $w+"_Approach_sep"
    showinfo
end
Macro Ryan_Modify_force_curves(w_approach,w_separation,zero_flag,contact_flag,contact_value,tip_flag)
    string w_approach
    Prompt w_approach "MODIFY approach deflection wave:", popup WaveList("*_deflection",";", "")
    string w_separation
    Prompt w_separation "MODIFY approach separation wave:", popup WaveList("*_sep",";", "")
    variable zero_flag=1
    Prompt zero_flag, "MODIFY deflection wave to first point:", popup "ZERO wave;DO NOT zero wave"
    variable contact_flag=1
    Prompt contact_flag, "MODIFY separation wave at contact:", popup "ZERO wave; DO NOT zero wave"
    //variable contact_value=100e-9
    //Prompt contact_value, "Enter present Contact value"
    variable tip_flag=1
    Prompt tip_flag, "MODIFY for Tip Height:", popup "MODIFY wave; DO NOT modify wave"
    variable contact_value=hcsr(a)
    if(zero_flag==1)
        wavestats/q/t=[5,10] $w_approach
            $w_approach-=v_avg
        endif
    if(contact_flag==1)
        $w_separation-=contact_value
    endif
    if(tip_flag==1)
        if(contact_flag==1)
            $w_separation+=(root:original_files:tip_height)
        else
            $w_separation+=(root:original_files:tip_height-contact_value)
        endif
    endif
    Variable/g Height=hcsr(b)

end // End of Ryan_Modify_force_curves

macro Ryan_record_height_data(indexrj, folder)
    variable indexrj=0
    Prompt indexrj "index in waves"
    string folder
    Prompt folder "name of folder to get data"
    root:Height[indexrj]=root:$folder+"_processed":height;
    root:Hfreq[indexrj]=root:$folder+"_processed":resfreq;
endmacro

```

```

    root:Hdamp[indexrj]=root:$folder+"_processed":thermaldamp;
root:Hspring[indexrj]=root:$folder+"_processed":thermalspring;
    root:Hmass[indexrj]=root:$folder+"_processed":thermalmass
end

//Computes the squeeze film theory curves (Vinogradova).
// Computes both actual deflection curve and dimensionless curves, which should
// collapse all curves into one except for drag offset.
// have option to run with processed folders or use you own files
macro Ryan_dimensionless_squeeze(tempvelocity,use_processed_flag)
    Variable tempvelocity=100e-6
    Prompt tempvelocity,"enter velocity (m/s) for particular test(ignore if using processed files)"
    variable use_processed_flag=1
    Prompt use_processed_flag,"are processed folders present in experiment?","popup" "Yes;No"
    pauseupdate
    if(use_processed_flag==1)
        tempvelocity=PullSpeed*1e-6
        Duplicate/O $WaveList("*_pull_Approach_deflection", "", "") norm_force
        Duplicate/O $WaveList("*_Approach_sep", "", "") norm_sep
    endif
    if(use_processed_flag==1)
        print "new waves in current folder"
    else
        newdatafolder/O/S root:original_files
    endif
    variable/g
tempreynolds=root:original_files:fluid_density*root:original_files:cantilever_width*tempvelocity/root:original_files
:fluid_viscosity
    variable/g tempv=tempvelocity
    variable/g width_correction
    variable aspect_ratio=root:original_files:cantilever_width/root:original_files:cantilever_length
    make/o/n=1000 ryansqeezefunc, ryansqeezeUNITS, angle_correction1,angle_correction2
    width_correction=comp_counter(aspect_ratio)

    setscale/I x,0,1,angle_correction1
    setscale/I x,0,1,ryansqeezefunc
    variable/g lalpha=root:original_files:cantilever_length*root:original_files:cantilever_angle
    variable/g wolalpha=root:original_files:cantilever_width/lalpha
    angle_correction1:=4/3*(x*wolalpha)*(1-3/2*(x*wolalpha)+3*(x*wolalpha)^2-
3*(x*wolalpha)^3*ln(1+1/(x*wolalpha)))
    ryansqeezefunc:=(3/8)*(1/x)^3*width_correction*angle_correction1 + 4*pi/(log(7.4/tempreynolds))

    setscale/I x,0,root:original_files:cantilever_width,angle_correction2
    setscale/I x,0,root:original_files:cantilever_width,ryansqeezeUNITS
    // variable/g lalpha=root:original_files:cantilever_length*root:original_files:cantilever_angle
    angle_correction2:=4/3*(x/lalpha)*(1-3/2*(x/lalpha)+3*(x/lalpha)^2-3*(x/lalpha)^3*ln(1+1/(x/lalpha)))
    ryansqeezeUNITS:=((3/8)*(root:original_files:cantilever_width/x)^3*width_correction*angle_correction2
+
4*pi/(log(7.4/tempreynolds)))*(root:original_files:cantilever_length*root:original_files:fluid_viscosity*tempv/root:
original_files:bulk_spring_const)

    norm_force*=root:original_files:bulk_spring_const/(root:original_files:cantilever_length*root:original_file
s:fluid_viscosity*tempv)
    norm_sep/=root:original_files:cantilever_width
    resumeupdate
end

```

```

function comp_counter(aspect_ratio)
    variable aspect_ratio
    variable punkie=0
    variable jc=1
    // only use odd counter number (2*jc-1)
    for(jc=1;jc<=100;jc+=1)
        //print punkie
        punkie+=(-3*aspect_ratio*(2*jc-1)*pi+2*(3*aspect_ratio^3+((2*jc-1)*pi)^2)*tanh(pi*(2*jc-
1)/2/aspect_ratio))/((2*jc-1)^7)
    endfor
    punkie=1-2^7*aspect_ratio/pi^7*punkie
    return punkie
end

// This macro generates added mass and dampening terms as defined by Sader's Thoery
// prompts for file which is generated by matlab via mathcad component.
macro Ryan_added_theory(use_process_flag)
    variable use_process_flag=1
    Prompt use_process_flag, "are processed folders present in experiment?", popup "Yes;No"
    if(use_process_flag==1)
        print "new waves in current folder"
    else
        newdatafolder/O/S root:original_files
    endif
    string pull_name="hydro"
    LoadWave/J/D/N=$pull_name/K=0
    Duplicate/o $pull_name+"0" $pull_name+"_Re"; killwaves $pull_name+"0"
    Duplicate/o $pull_name+"1" $pull_name+"_Im"; killwaves $pull_name+"1"
    Duplicate/o $pull_name+"2" $pull_name+"_x_reynolds"; killwaves $pull_name+"2"
    variable
mass_cant=pi*(root:original_files:cantilever_width/2)^2*root:original_files:cantilever_length*root:original_files:flu
id_density
    Duplicate/o $pull_name+"_Re" M_eff
    Duplicate/o $pull_name+"_Im" B_eff
    Duplicate/o $pull_name+"_x_reynolds" $pull_name+"_x_Hz"
    $pull_name+"_x_Hz"*=4*root:original_files:fluid_viscosity/root:original_files:fluid_density/root:original_
files:cantilever_width^2/2/pi
    M_eff*=mass_cant
    B_eff*=(-1)*mass_cant*$pull_name+"_x_Hz"*2*pi
    SetScale d 0,0,"Kg", M_eff
    SetScale d 0,0,"N*s/m", B_eff
    SetScale d 0,0,"Hz", $pull_name+"_x_Hz"
    //set scale for hydrodynamic function...depends on how it was generated
    // I set it equally spaced logarithmatically.
    //variable/g seghydro=1000
    //make/n=(seghydro)/o hydro_freq=loophydro(seghydro); killwaves tempx
    //B_eff*=hydro_freq*2*pi*(-1)*mass_cant
end
function loophydro(seghydro)
    variable seghydro
    NVAR vis=root:original_files:fluid_viscosity
    NVAR dens=root:original_files:fluid_density
    NVAR width=root:original_files:cantilever_width
    variable reynolds_multi=(4*vis)/(dens*width^2*2*pi)
    variable ll=2e-3
    variable ul=4e4

```

```

variable int=seghydro
variable jj=0
make/N=(int)/O tempx
for(jj=0 ; jj<int ; jj+=1)
    if(jj>=1)
        tempx[jj]=reynolds_multi*ll*(ul/ll)^(jj/(int-1))
    else
        tempx[jj]=reynolds_multi*ll*1           // for j=0
    endif
endfor
return tempx
end
//end of macro Ryan_added_theory

//for display purposes only...have defined functions for computing effect on cantilever response
macro Ryan_VE_hydro(startfreq, endfreq, numpnt)
    variable startfreq=1
    Prompt startfreq,"beginning frequency: Hz:"
    variable endfreq=1e6
    Prompt endfreq,"ending frequency: Hz:"
    variable numpnt=1000
    Prompt numpnt,"number of points in waves to be displayed:"
    variable/g numpnt=numpnt
    newdatafolder/O/S root:original_files
    //variable/g numpoint=numpnt
    make/o/n=(numpnt) rjfreq_x= 10^(log(startfreq)+(log(endfreq)-log(startfreq))/numpnt*x)
    // call and break them into real and imag part Dependencies
    make/o/n=(numpnt) nmass_newtonian:=real(RH2(rjfreq_x,fluid_density,cantilever_width,fluid_viscosity))
    ndisp_newtonian:=imag(RH2(rjfreq_x,fluid_density,cantilever_width,fluid_viscosity))*rjfreq_x*2*pi
    make/o/n=(numpnt)
    nmass_shearthin:=real(RVH(rjfreq_x,fluid_density,cantilever_width,fluid_viscosity,relaxation_time))
    make/o/n=(numpnt)
    ndisp_shearthin:=imag(RVH(rjfreq_x,fluid_density,cantilever_width,fluid_viscosity,relaxation_time))*rjfreq_x*2*pi
    i
    make/o/n=(numpnt)
    nmass_LVE:=real(RVEH(rjfreq_x,fluid_density,cantilever_width,fluid_viscosity,relaxation_time))
    make/o/n=(numpnt)
    ndisp_LVE:=imag(RVEH(rjfreq_x,fluid_density,cantilever_width,fluid_viscosity,relaxation_time))*rjfreq_x*2*pi
    make/o/n=(numpnt)
    ndisp_LVE_alt:=Ndisp_LVEfluid_alt(rjfreq_x,fluid_density,cantilever_width,fluid_viscosity,relaxation_time,cantilever_length)

    make/o/n=(numpnt)
    mass_LVE:=mass_LVEfluid(rjfreq_x,fluid_density,cantilever_width,fluid_viscosity,relaxation_time,cantilever_length)
    make/o/n=(numpnt)
    disp_LVE:=disp_LVEfluid(rjfreq_x,fluid_density,cantilever_width,fluid_viscosity,relaxation_time,cantilever_length)
    make/o/n=(numpnt)
    disp_LVE_alt:=disp_LVEfluid_alt(rjfreq_x,fluid_density,cantilever_width,fluid_viscosity,relaxation_time,cantilever_length)
    make/o/n=(numpnt)
    mass_V:=mass_Vfluid(rjfreq_x,fluid_density,cantilever_width,fluid_viscosity,relaxation_time,cantilever_length)
    make/o/n=(numpnt)
    disp_V:=disp_Vfluid(rjfreq_x,fluid_density,cantilever_width,fluid_viscosity,relaxation_time,cantilever_length)

```

```

        make/o/n=(numpnt)
mass_2:=mass_2fluid(rjfreq_x,fluid_density,cantilever_width,fluid_viscosity,cantilever_length)
        make/o/n=(numpnt)
disp_2:=disp_2fluid(rjfreq_x,fluid_density,cantilever_width,fluid_viscosity,cantilever_length)

        Display
nmass_newtonian,ndisp_newtonian,nmass_shearthin,ndisp_shearthin,nmass_LVE,ndisp_LVE,ndisp_LVE_alt,mass
_LVE,disp_LVE,disp_LVE_alt,mass_V,disp_V,mass_2,disp_2 vs rjfreq_x
        ModifyGraph log=1;DelayUpdate
        Label left "Normalized  $m \backslash Badd \backslash M$  &  $b \backslash Badd \backslash M$ ";DelayUpdate
        Label bottom "Frequency [Hz]"
end // end of Ryan_VE_hydro
//Ryan Hydro Function (kinematic Reynolds)
function/c RH(krey)
        variable krey
        variable/c H=1+cmplx(0,1)*4/(sqrt(cmplx(0,1)*krey))
        return H
end
//Ryan Hydro Function (frequency in Hz)
function/c RH2(f,density,width,viscosity)
        variable f
        variable density//=root:original_files:fluid_density
        variable width//=root:original_files:cantilever_width
        variable viscosity//=root:original_files:fluid_viscosity
        variable/c H=1+cmplx(0,1)*4/(sqrt(cmplx(0,1)/4*(density*(width*width)*(2*pi*f)/(viscosity)))
        return H
end
function mass_2fluid(f,density,width,viscosity,length)
        variable f
        variable density//=root:original_files:fluid_density
        variable width//=root:original_files:cantilever_width
        variable viscosity//=root:original_files:fluid_viscosity
        variable length//=root:original_files:cantilever_length
        variable displaced_mass=1*density*length*pi*(width/2)^2
        variable m_2=displaced_mass*real(RH2(f,density,width,viscosity))
        return m_2
end
function disp_2fluid(f,density,width,viscosity,length)
        variable f
        variable density//=root:original_files:fluid_density
        variable width//=root:original_files:cantilever_width
        variable viscosity//=root:original_files:fluid_viscosity
        variable length//=root:original_files:cantilever_length
        variable displaced_mass=1*density*length*pi*(width/2)^2
        variable b_2=displaced_mass*imag(RH2(f,density,width,viscosity))*f*2*pi
        return b_2
end
// Ryan viscosity dependent Hydro function (Hz)
function/c RVH(f,density,width,viscosity,relax)
        variable f
        variable density//=root:original_files:fluid_density
        variable width//=root:original_files:cantilever_width
        variable viscosity//=root:original_files:fluid_viscosity
        variable relax//=root:original_files:relaxation_time
        variable/c H=1+cmplx(0,1)*4/( sqrt( cmplx(0,1)/4* ( density*(width*width)*(2*pi*f) /
(viscosity/(1+(relax*2*pi*f)*(relax*2*pi*f))) ) ) )

```

```

    return H
end
function mass_Vfluid(f,density,width,viscosity,relax,length)
    variable f
    variable density//=root:original_files:fluid_density
    variable width//=root:original_files:cantilever_width
    variable viscosity//=root:original_files:fluid_viscosity
    variable relax//=root:original_files:relaxation_time
    variable length//=root:original_files:cantilever_length
    variable displaced_mass=1*density*length*pi*(width/2)^2
    variable m_V=displaced_mass*real(RVH(f,density,width,viscosity,relax))
    return m_V
end
function disp_Vfluid(f,density,width,viscosity,relax,length)
    variable f
    variable density//=root:original_files:fluid_density
    variable width//=root:original_files:cantilever_width
    variable viscosity//=root:original_files:fluid_viscosity
    variable relax//=root:original_files:relaxation_time
    variable length//=root:original_files:cantilever_length
    variable/g displaced_mass=1*density*length*pi*(width/2)^2
    variable b_V=displaced_mass*imag(RVH(f,density,width,viscosity,relax))*f*2*pi
    return b_V
end
// Ryan visco-elastic Hydro function(Hz)
function/c RVEH(f,density,width,viscosity,relax)
    variable f
    variable density//=root:original_files:fluid_density
    variable width//=root:original_files:cantilever_width
    variable viscosity//=root:original_files:fluid_viscosity
    variable relax//=root:original_files:relaxation_time
    variable/c H=1+cmplx(0,1)*4/(sqrt(cmplx(0,1)/4*(density*(width*width)*(2*pi*f)/
viscosity/(1+(relax*2*pi*f)*(relax*2*pi*f)) -
cmplx(0,1)*viscosity*(relax*2*pi*f)/(1+(relax*2*pi*f)*(relax*2*pi*f)))) )
    return H
end
function mass_LVEfluid(f,density,width,viscosity,relax,length)
    variable f
    variable density//=root:original_files:fluid_density
    variable width//=root:original_files:cantilever_width
    variable viscosity//=root:original_files:fluid_viscosity
    variable relax//=root:original_files:relaxation_time
    variable length//=root:original_files:cantilever_length
    variable displaced_mass=1*density*length*pi*(width/2)^2
    variable m_LVE=displaced_mass*real(RVEH(f,density,width,viscosity,relax))
    return m_LVE
end
function disp_LVEfluid(f,density,width,viscosity,relax,length)
    variable f
    variable density//=root:original_files:fluid_density
    variable width//=root:original_files:cantilever_width
    variable viscosity//=root:original_files:fluid_viscosity
    variable relax//=root:original_files:relaxation_time
    variable length//=root:original_files:cantilever_length
    variable displaced_mass=1*density*length*pi*(width/2)^2
    variable b_LVE=displaced_mass*imag(RVEH(f,density,width,viscosity,relax))*f*2*pi

```

```

        return b_LVE
end
// reworking above function, to better approximate actual dissipative effect as shown by Mathcad file
function disp_LVEfluid_alt(f,density,width,viscosity,relax,length)
    variable f
    variable density//=root:original_files:fluid_density
    variable width//=root:original_files:cantilever_width
    variable viscosity//=root:original_files:fluid_viscosity
    variable relax//=root:original_files:relaxation_time
    variable length//=root:original_files:cantilever_length
    variable displaced_mass=1*density*length*pi*(width/2)^2
    variable b_LVE=displaced_mass*(f*2*pi)*(4*sqrt(2/(density*(width*width)*(2*pi*f)/ (
viscosity/(1+(relax*2*pi*f)*(relax*2*pi*f)))))) *((relax*2*pi*f)*((1+(1/(relax*2*pi*f)^2)^.5+1))^.5
    return b_LVE
end

function Ndisp_LVEfluid_alt(f,density,width,viscosity,relax,length)
    variable f
    variable density//=root:original_files:fluid_density
    variable width//=root:original_files:cantilever_width
    variable viscosity//=root:original_files:fluid_viscosity
    variable relax//=root:original_files:relaxation_time
    variable length//=root:original_files:cantilever_length
    variable displaced_mass=1*density*length*pi*(width/2)^2
    variable b_LVE=(f*2*pi)*(4*sqrt(2/(density*(width*width)*(2*pi*f)/ (
viscosity/(1+(relax*2*pi*f)*(relax*2*pi*f)))))) *((relax*2*pi*f)*((1+(1/(relax*2*pi*f)^2)^.5+1))^.5
    return b_LVE
end

//macro for generating superposition of damped modes with function RyanSHO
macro Ryan_SHO_added(wname,add_flag)
    string wname="name of SHO added wave"
    variable add_flag=4
    prompt add_flag "select fluid model for added m & b: ", popup "no added terms;Newtonian;Shear-
Thinning;Linear Visco-Elastic"
    newdatafolder/O/S root:original_files

    make/o/n=12 SHO_coef_air=0
    // constant multiplying density is arbitrary in lieu of integral calculation which give approx. same value
    variable/g aa=.29
    variable/g cc=.12 //mass correction factor for the fact that theory is for infinite cylinder and we have a
cantilevered beam
    variable/g bb=.12 //damping correction factor for the fact that theory is for infinite cylinder and we have a
cantilevered beam
    SHO_coef_air[0]=(aa*cantilever_density*cantilever_width*cantilever_thickness*cantilever_length);SHO_
coef_air[1]=1e-
8;SHO_coef_air[2]=SHO_modes_spring(0,cantilever_length,cantilever_width,cantilever_thickness,cantilever_Mod
ulus,cantilever_density) // m1,b1,k1
    SHO_coef_air[3]=(aa*cantilever_density*cantilever_width*cantilever_thickness*cantilever_length);SHO_
coef_air[4]=1e-
8;SHO_coef_air[5]=SHO_modes_spring(1,cantilever_length,cantilever_width,cantilever_thickness,cantilever_Mod
ulus,cantilever_density) // m2,b2,k2
    SHO_coef_air[6]=(aa*cantilever_density*cantilever_width*cantilever_thickness*cantilever_length);SHO_
coef_air[7]=1e-
8;SHO_coef_air[8]=SHO_modes_spring(2,cantilever_length,cantilever_width,cantilever_thickness,cantilever_Mod
ulus,cantilever_density) // m3,b3,k3

```



```

    SHO_coef_air[9]=(aa*cantilever_density*cantilever_width*cantilever_thickness*cantilever_length);SHO_
coef_air[10]=1e-
8;SHO_coef_air[11]=SHO_modes_spring(3,cantilever_length,cantilever_width,cantilever_thickness,cantilever_Mo
dulus,cantilever_density) // m4,b4,k4

    make/o/n=17 SHO_coef_fluid_fitfunc=0
    SHO_coef_fluid_fitfunc=SHO_coef_air
    SHO_coef_fluid_fitfunc[12]=fluid_density ; SHO_coef_fluid_fitfunc[13]=fluid_viscosity ;
SHO_coef_fluid_fitfunc[14]=relaxation_time;
    SHO_coef_fluid_fitfunc[15]=cantilever_length ; SHO_coef_fluid_fitfunc[16]=cantilever_width

    make/o/n=(numpnt)
$wname+"_ALT":=sqrt(1*(RyanSHO(SHO_coef_air,rjfreq_x,4,fluid_density,cantilever_width,fluid_viscosity,relax
ation_time,cantilever_length,cc,bb)))
    make/o/n=(numpnt)
$wname+"_LVE":=sqrt(1*(RyanSHO(SHO_coef_air,rjfreq_x,3,fluid_density,cantilever_width,fluid_viscosity,relax
ation_time,cantilever_length,cc,bb)))
    make/o/n=(numpnt)
$wname+"_ShearThinning":=sqrt(1*(RyanSHO(SHO_coef_air,rjfreq_x,2,fluid_density,cantilever_width,fluid_visc
osity,relaxation_time,cantilever_length,cc,bb)))
    make/o/n=(numpnt)
$wname+"_Newtonian":=sqrt(1*(RyanSHO(SHO_coef_air,rjfreq_x,1,fluid_density,cantilever_width,fluid_viscosity
,relaxation_time,cantilever_length,cc,bb)))
    make/o/n=(numpnt)
$wname+"_NoADD":=sqrt(1*(RyanSHO(SHO_coef_air,rjfreq_x,0,fluid_density,cantilever_width,fluid_viscosity,r
elaxation_time,cantilever_length,cc,bb)))

    Display
$wname+"_LVE",$wname+"_ShearThinning",$wname+"_Newtonian",$wname+"_NoADD",$wname+"_ALT" vs
rjfreq_x
    ModifyGraph log=1;DelayUpdate
    Label left "Magnitude of Transfer Function [m/N]";DelayUpdate
    Label bottom "Frequency [Hz]"

end // end of Macro
function SHO_modes_freq(index,can_length,can_width,can_thick,can_modulus,can_density)
    variable index
    variable can_length
    variable can_width
    variable can_thick
    variable can_modulus
    variable can_density

    make/o/n=4 KL
    KL[0]=1.875;KL[1]=4.694;KL[2]=7.853;KL[3]=10.996

    variable AA=can_width*can_thick
    variable inert=can_width/12*(can_thick)^3
    make/o/n=4 EIRA=can_modulus*inert/can_density/AA
    make/o/n=4 freq_temp=(1/2/pi)*sqrt(EIRA)*(KL/can_length)^2
    return freq_temp[(index)]
end
function SHO_modes_spring(index,can_length,can_width,can_thick,can_modulus,can_density)
    variable index
    variable can_length
    variable can_width

```

```

variable can_thick
variable can_modulus
variable can_density

make/o/n=4 KL
KL[0]=1.875;KL[1]=4.694;KL[2]=7.853;KL[3]=10.996

variable AA=can_width*can_thick
variable inert=can_width/12*(can_thick)^3
make/o/n=4 EI=can_modulus*inert
make/o/n=4 spring_temp=0.2427*can_length*EI*(KL/can_length)^4
return spring_temp[(index)]
end

// generate function that returns Voltage psd so that I can conver my model
// back to a V^2/Hz scale then add noise and then convert back to transfer function
// this will allow better comparison to observed data

macro Ryan_add_noise(foldername, psdnoise, wavetomodify)
string foldername="A1"
variable psdnoise=6e-11
Prompt psdnoise, "value of PSD noise: V^2/Hz"
string wavetomodify="fluid_ALT"

string/g root:original_files:NoiseAddedWave=wavetomodify

NewDataFolder/O/S root:$foldername+"_processed"
variable/g add_termL
add_termL= psdnoise*OpticalLeverSens^2*1e-
18*(ThermalQ*2*pi*Resfreq/ThermalSpringC)/(4*Boltzman*Temperature)
variable/g root:original_files:add_term=root:$foldername+"_processed":add_termL
NewDataFolder/O/S root:original_files
duplicate/o $NoiseAddedWave test_noise test2_noise test3_noise test4_noise Rconstant
test_noise:=sqrt(add_term+$NoiseAddedWave^2 )

make/o/n=(numpnt) correctingwave
correctingwave=(1+rjfreq_x/2e4)^-1.2/(1+rjfreq_x/1e5)^4
test2_noise:=$NoiseAddedWave/correctingwave
test3_noise:=sqrt(add_term+test2_noise^2 )
Rconstant=5
test4_noise:=Rconstant+$NoiseAddedWave
end

// Macro to compute viscosity based on bulk drag on cantilever
// enter deflection value and
macro Ryan_bulk_viscometer(foldername, bulk_deflection)
string foldername="P1"
variable bulk_deflection=5e-9
Prompt bulk_deflection, "enter static defelction value:"

NewDataFolder/O/S root:original_files
variable/g
mu=(bulk_deflection*root:original_files:bulk_spring_const*8/3*2)/(root:$foldername+"_processed":pullspeed*1e-
6*cantilever_length*11.75)
print "viscosity as determined by microviscometer: = ", mu, " Pa s"

```

```

end

// SaveGraph 1.2
//
// Creates an Igor Text file that will be able to recreate the target graph (including the data)
// in another experiment.
//
// To use, simply bring the graph you wish to save to the front and select "Save Graph"
// from the Macros menu. You will be presented with a save dialog.
// Later, in another experiment, you can use the "Load Igor Text..." item from the Data menu
// to load the file. The data will be loaded and the graph will be regenerated.
//
// "Save Graph" makes an Igor Text file that, when later loaded, will load the data into a data folder
// of the same name as your graph. If there are conflicts in the wave names, subfolders called
// data1 etc will be created for any subsequent waves.
//
// No data folders or waves are created by the Save Graph macros in the experiment where
// the graph was first created. All new folders and waves are generated by loading the Igor
// Text file that recreates the graph. The new folders and waves are in the destination experiment.
//
// NOTE: The data folder hierarchy from the original experiment is not preserved by Save Graph.
//
// Version 1.2 supports commands in the graph recreation macro that exceed 256 characters.
// Version 1.1 differs from the first version as follows:
//     Supports Igor 3.0's Data Folders, liberal wave names
//     Supports contour and image graphs.

##pragma rtglobals=1
##pragma version=1.2 // 2/2/99

Macro Ryan_Save_Regen_Graph()
    DoSaveGraphToFile()
end

Function DoSaveGraphToFile()

    Variable numWaves
    Variable refnum
    Variable i
    Variable pos0, pos1
    Variable FolderLevel=1

    String TopFolder, FolderName
    String WinRecStr
    String fileName
    String wname= WinName(0,1)

    if( strlen(wname) == 0 )
        DoAlert 0,"No graph!"
        return 0
    else
        DoWindow/F $wname
    endif
    TopFolder= wname
    GetWindow kwTopWin, wavelist
    Wave/T wlist=W_WaveList

```

```

numWaves = DimSize(wlist, 0)
Redimension/N=(-1,5) wlist
MakeUniqueFolders(wlist, "data")
Open/D refnum as wname
filename=S_filename
if (strlen(filename) == 0)
    DoAlert 0, "You cancelled the Save Graph operation"
    KillWaves/Z wlist
    return 0
endif
Open refnum as filename
fprintf refnum, "%s", "IGOR\r"
fprintf refnum, "%s", "X NewDataFolder/S/O "+TopFolder+"\r"
close refnum
i = 0
do
    if (strlen(wlist[i][3]) != 0)
        Open/A refnum as filename
        if (FolderLevel > 1)
            fprintf refnum, "%s", "X SetDataFolder ::\r"
        endif
        fprintf refnum, "%s", "X NewDataFolder/S "+wlist[i][3]+"\r"
        FolderLevel=2
        close refnum
    endif
    Execute "Save/A/T "+wlist[i][1]+" as \"+FileName+"\"
    i += 1
while (i < numWaves)
if (FolderLevel > 1)
    Open/A refnum as filename
    fprintf refnum, "%s", "X SetDataFolder ::\r"
    close refnum
endif
WinRecStr = WinRecreation(wname, 2)
i = 0
FolderName = ""
do
    pos0=0
    if (strlen(wlist[i][3]) != 0)
        FolderName = ":"+wlist[i][3]+":"
    endif
    do
        pos0=strsearch(WinRecStr, wlist[i][2], pos0+1)
        if (pos0 < 0)
            break
        endif
        WinRecStr[pos0,pos0+strlen(wlist[i][2])-1] =
FolderName+PossiblyQuoteName(wlist[i][0])
        while (1)
            i += 1
        while (i<numWaves)
            Open/A refnum as filename
            pos0= strsearch(WinRecStr, "\r", 0)
            pos0= strsearch(WinRecStr, "\r", pos0+1)+1
            fprintf refnum,"X Preferences 0\r"
            String str

```

```

do
    pos1= strstr(WinRecStr, "r", pos0)
    if( (pos1 == -1) %| (cmpstr(WinRecStr[pos0,pos0+2],"End") == 0) )
        break
    endif
//    fprintf refnum,"X%s%s",WinRecStr[pos0,pos1-1];DelayUpdate\r" // has 256 character limit
    str= "X"+WinRecStr[pos0,pos1-1];DelayUpdate\r" //
Version 1.2, 2/2/99
    FBinWrite refnum, str
    pos0= pos1+1
    while(1)
        fprintf refnum, "%s", "X SetDataFolder ::\r"
        fprintf refnum,"X Preferences l\r"
        fprintf refnum,"X KillStrings S_waveNames\r"
        close refnum
        KillWaves/Z wlist
        return 0
    end
Function MakeUniqueFolders(wlist, FBaseName)
    Wave/T wlist
    String FBaseName
    Variable i,j, endi = DimSize(wlist, 0), startj = 0
    Variable FolderNum = 0
    wlist[0][3] = ""
    i = 1
    do
        j = startj
        do
            if (cmpstr(wlist[i][0], wlist[j][0]) == 0)
                FolderNum +=1
                wlist[i][3] = FBaseName+num2istr(FolderNum)
                startj = i
                break
            endif
            j += 1
        while (j < i)
        i += 1
    while (i < endi)
end
// this is the end of the Macro and associated functions that are required to save a graph to be regenerated.

```

Works cited

1. Bowden, F.P. and D. Tabor, *Friction and Lubrication of Solids*. International series of monographs on physics. 1950, Oxford,: Clarendon Press. 337.
2. Spikes, H.A. *Boundary Lubrication and Boundary Films*. in *Leeds-Lyon Symposium on Tribology*. 1993: Elsevier Science.
3. Elcoate, C.D., et al. *Thin Film, Time-Dependent, Micro-EHL Solutions with Real Surface Roughness*. in *Leeds-Lyon Symposium on Tribology*. 1999: Elsevier Science.
4. Hu, Y.-Z. and D. Zhu, *A Full Numerical Solution to the Mixed Lubrication in Point Contact*. *Journal of Tribology*, 2000. 122: p. 1-9.
5. Gao, J., L.W. D, and L. Uzi, *Nano-elastohydrodynamics: structure, dynamics, and flow in nonuniform lubricated junctions*. *Science*, 1995. 270: p. 605-8.
6. Gao, J., L.W. D, and L. Uzi, *Structure and solvation forces in confined films: Linear and branched alkanes*. *Journal of Chemical Physics*, 1996. 106(10): p. 4309-4318.
7. Hidrovo, C.H. and D.P. Hart, *Emission reabsorption laser induced fluorescence (ERLIF) film thickness measurement*. *Measurement Science & Technology*, 2001. 12(4): p. 467-477.
8. Cann, P.M., H.A. Spikes, and J. Hutchinson, *Development of a spacer layer imaging method (SLIM) for mapping elastohydrodynamic contacts*. *Tribology Transactions*, 1996. 39(4): p. 915-921.
9. Guangteng, G., et al., *Lubricant Film Thickness in Rough Surface, Mixed Elastohydrodynamic Contact*. *Journal of Tribology*, 2000. 122: p. 65-76.
10. Molimard, J., M. Querry, and P. Vergne, *New Tools for the Experimental Study of EHD and Limit Lubrications*. in *Leeds-Lyon Symposium on Tribology*. 1999: Elsevier Science.
11. Hupp, S., *Experimental method for frictional characterization of micro-textured surfaces*. 2004.
12. Jacobson, B.O., *Rheology and elastohydrodynamic lubrication*. *Tribology series* ; 19. 1991, Amsterdam ; New York: Elsevier. xv, 382.
13. Macosko, C.W., *Rheology : Principles, Measurements, and Applications*. *Advances in interfacial engineering series*. 1994, New York: Wiley-VCH. 550.
14. Bird, R.B., R.C. Armstrong, and O. Hassager, *Dynamics of Polymeric Liquids*. Vol. 1. 1987, New York: Wiley-Interscience.
15. Braithwaite, G. and G. McKinley, *Microrheometry for Studying the Rheology and Dynamics of Polymers near Interfaces*. *Journal of Applied Rheology*, 1999. 9: p. 27-33.
16. Dhinojwala, A. and S. Granick, *Micron-gap rheo-optics with parallel plates*. *Journal of Chemical Physics*, 1997. 107(20): p. 8664-7.
17. Zhu, Y.X. and S. Granick, *Healing of confined polymer films following deformation at high shear rate*. *Journal of Rheology*, 2000. 44(5): p. 1169-1182.
18. Luengo, G., J. Israelachvili, and S. Granick, *Generalized effects in confined fluids: New friction map for boundary lubrication*. *Wear*, 1996. 200(1-2): p. 328-335.
19. Luengo, G., et al., *Thin film rheology and tribology of confined polymer melts: Contrasts with bulk properties*. *Macromolecules*, 1997. 30(8): p. 2482-2494.
20. Demirel, A.L. and S. Granick, *Glasslike transition of a confined simple fluid*. *Physical Review Letters*, 1996. 77(11): p. 2261-2264.
21. *Handbook of Micro/Nano Tribology*. *Mechanics and Materials Science*, ed. B. Bhushan. 1995, New York: CRC Press. 628.
22. Ortiz, C. and G. Hadziioannou, *Entropic elasticity of single polymer chains of poly(methacrylic acid) measured by atomic force microscopy*. *Macromolecules*, 1999. 32(3): p. 780-787.
23. Wong, J., A. Chilkoti, and V.T. Moy, *Direct force measurements of the streptavidin-biotin interaction*. *Biomolecular Engineering*, 1999. 16(1-4): p. 45-55.
24. O'Shea, S.J., M.E. Welland, and T. Rayment, *Solvation Forces near a Graphite Surface Measured with an Atomic Force Microscope*. *Applied Physics Letters*, 1992. 60(19): p. 2356-2358.
25. Han, W.H., S.M. Lindsay, and T.W. Jing, *A magnetically driven oscillating probe microscope for operation in liquids*. *Applied Physics Letters*, 1996. 69(26): p. 4111-4113.
26. Lantz, M., et al., *Dynamic force microscopy in fluid*. *Surface and Interface Analysis*, 1999. 27(5-6): p. 354-360.

27. O'Shea, S.J., *Oscillatory forces in liquid atomic force microscopy*. Japanese Journal of Applied Physics Part 1-Regular Papers Short Notes & Review Papers, 2001. 40(6B): p. 4309-4313.
28. Burnham, N.A., et al., *Scanning local-acceleration microscopy*. Journal of Vacuum Science & Technology B, 1996. 14(2): p. 794-799.
29. Wahl, K.J., S.V. Stepnowski, and W.N. Unertl, *Viscoelastic effects in nanometer-scale contacts under shear*. Tribology Letters, 1998. 5(1): p. 103-107.
30. Wahl, K.J. and W.N. Unertl, *Formation of Nanometer-Scale Contacts to Viscoelastic Materials*.
31. Roters, A., et al., *Collapse of a polymer brush in a poor solvent probed by noise analysis of a scanning force microscope cantilever*. Langmuir, 1998. 14(15): p. 3999-4004.
32. Chen, S.-S., *Flow-Induced Vibration of Circular Cylindrical Structures*. 1987, New York: Hemisphere Publishing Corporation.
33. Kirstein, S., M. Mertesdorf, and M. Schonhoff, *The influence of a viscous fluid on the vibration dynamics of scanning near-field optical microscopy fiber probes and atomic force microscopy cantilevers*. Journal of Applied Physics, 1998. 84(4): p. 1782-1790.
34. Boskovic, S., et al., *Rheological measurements using microcantilevers*. Journal of Rheology, 2002. 46(4): p. 891-899.
35. Chon, J.W.M., P. Mulvaney, and J.E. Sader, *Experimental validation of theoretical models for the frequency response of atomic force microscope cantilever beams immersed in fluids*. Journal of Applied Physics, 2000. 87(8): p. 3978-3988.
36. Goodman, J.W., *Statistical Optics*. Wiley classics library. 2000, New York: Wiley. 550.
37. Timoshenko, S., D.H. Young, and W. Weaver, *Vibration problems in engineering*. 4 ed. 1974, New York: John Wiley&Sons.
38. Hosaka, H., K. Itao, and S. Kuroda, *Damping Characteristics of Beam-Shaped Micro-Oscillators*. Sensors and Actuators a-Physical, 1995. 49(1-2): p. 87-95.
39. Sader, J.E., et al., *Method for the Calibration of Atomic-Force Microscope Cantilevers*. Review of Scientific Instruments, 1995. 66(7): p. 3789-3798.
40. Allen, B. and P. Brady, *Quantization Noise in Ligo Interferometers*. 1997, University of Wisconsin California Institute of Technology: Milwaukee, WI Pasadena, CA.
41. Batchelor, G.K., *An Introduction to Fluid Mechanics*. 1967, Cambridge: Cambridge University Press.
42. Hutter, J.L. and J. Bechhoefer, *Calibration of Atomic-Force Microscope Tips*. Review of Scientific Instruments, 1993. 64(7): p. 1868-1873.
43. Saulson, P.R., *Thermal Noise in Mechanical Experiments*. Physical Review D, 1990. 42(8): p. 2437-2445.
44. Vinogradova, O.I. and G.E. Yakubov, *Dynamic effects on force measurements. 2. Lubrication and the atomic force microscope*. Langmuir, 2003. 19(4): p. 1227-1234.
45. Bazilevskii, A.V., V.M. Entov, and A.N. Rozhkov, *Breakup of an Oldroyd liquid bridge as a method for testing the rheological properties of polymer solutions*. Polymer Science Series A, 2001. 43(7): p. 716-726.
46. Bird, R.B., et al., *Dynamics of Polymeric Liquids*. Vol. 2. 1987, New York: John Wiley & Sons. 437.